AFRL-RV-PS-
TR-2022-0070

FUNDAMENTAL STUDY OF III-V BISMIDES FOR SPACE APPLICATIONS

Shane Johnson, et al.

Arizona State University
600 S Mill Ave Ste 312
Tempe, AZ 85281-3670

31 Jul 2022

Final Report

AIR FORCE RESEARCH LABORATORY
Space Vehicles Directorate
3550 Aberdeen Ave SE
AIR FORCE MATERIEL COMMAND
KIRTLAND AIR FORCE BASE, NM 87117-5776

NOTICE AND SIGNATURE PAGE

Using Government drawings, specifications, or other data included in this document for any purpose other than Government procurement does not in any way obligate the U.S. Government. The fact that the Government formulated or supplied the drawings, specifications, or other data does not license the holder or any other person or corporation; or convey any rights or permission to manufacture, use, or sell any patented invention that may relate to them.

This report is the result of contracted fundamental research which is exempt from public affairs security and policy review in accordance with AFI 61-201, paragraph 2.3.5.1. This report is available to the general public, including foreign nationals. Copies may be obtained from the Defense Technical Information Center (DTIC) (http://www.dtic.mil).

AFRL-RV-PS-TR-2022-0070 HAS BEEN REVIEWED AND IS APPROVED FOR PUBLICATION IN ACCORDANCE WITH ASSIGNED DISTRIBUTION STATEMENT.

//SIGNED//

PRESTON WEBSTER
Program Manager

//SIGNED//

CHRISTIAN MORATH
Tech Advisor, Space Component Technology Branch

//SIGNED//

JOHN BEAUCHEMIN
Chief Engineer, Spacecraft Technology Division
Space Vehicles Directorate

This report is published in the interest of scientific and technical information exchange, and its publication does not constitute the Government's approval or disapproval of its ideas or findings.

Approved for public release; distribution unlimited.

REPORT DOCUMENTATION PAGE

Form Approved
OMB No. 0704-0188

1. REPORT DATE *(DD-MM-YYYY)*	2. REPORT TYPE	3. DATES COVERED *(From - To)*
31-07-2022	Final Report	01 Aug 2019 - 31 Jul 2022

4. TITLE AND SUBTITLE

Fundamental Study of III-V Bismides for Space Applications

5a. CONTRACT NUMBER
FA9453-19-2-0004

5b. GRANT NUMBER

5c. PROGRAM ELEMENT NUMBER
C6601F

6. AUTHOR(S)

Johnson, Shane R
Schaefer, Stephen T
Kosireddy, Rajeev R
Milosavljevic, Marko S

5d. PROJECT NUMBER
4846

5e. TASK NUMBER
EF132582

5f. WORK UNIT NUMBER
V1EX

7. PERFORMING ORGANIZATION NAME(S) AND ADDRESS(ES)
Arizona State University
600 S Mill Ave Ste 312
Tempe, AZ 85281-3670

8. PERFORMING ORGANIZATION REPORT NUMBER

9. SPONSORING / MONITORING AGENCY NAME(S) AND ADDRESS(ES)
Air Force Research Laboratory
Space Vehicles Directorate
3550 Aberdeen Avenue SE
Kirtland AFB, NM 87117-5776

10. SPONSOR/MONITOR'S ACRONYM(S)
AFRL/RVSV

11. SPONSOR/MONITOR'S REPORT NUMBER(S)
AFRL-RV-PS-TR-2022-0070

12. DISTRIBUTION / AVAILABILITY STATEMENT
Approved for public release; distribution is unlimited.

13. SUPPLEMENTARY NOTES
Fundamental Study of III-V Bismides for Space Applications

14. ABSTRACT

The structural and optical properties of InAsSbBi samples grown on GaSb substrates by molecular beam epitaxy at Arizona State University and the Air Force Research Laboratory are measured by x-ray diffraction, Rutherford backscattering, transmission electron microscopy, and photoluminescence spectroscopy. The Bi mole fractions incorporated range from 0.04 to 1.81 percent. The sample luminescence at wavelengths of 3.72 – 6. 12 micrometers at low temperature. X-ray diffraction scans of the symmetric (400) and asymmetric (511) crystal planes provide the reciprocal space coordinates of the InAsSbBi layer peaks and GaSb substrate peaks. The relaxation and tilt of the InAsSbBi layers is determined from these measurements. Nomarski optical microscopy and atomic force microscopy are used to investigate the surface morphology of the InAsSbBi samples. Several 210 nm thick bulk InAsSbBi samples are irradiated using 63 MeV protons. The photoluminescence before and after radiation treatment is compared to analyze the radiation hardness of InAsSbBi. An in-depth x-ray diffraction study is performed for 210 nm thick bulk InAsSbBi grown on (100) on-axis and offcut GaSb substrates, with offcuts of 1° to (011) and 4° to (111A). The structural and optical properties of InAsSb, GaInAsSb, InAsSbBi, and GaInAs SbBiare determined from X-ray diffraction and photoluminescence and are compared. The diffusion length of mid-wave type-II InAs/InAsSb and InGaAs/InAsSb superlattices is calculated from a diffusion model utilizing steady-state photoluminescence. A kinetic model for molecular beam epitaxy growth of InAsSbBi is developed and fitted to bulk and quantum well samples grown at 400 – 420 °C. A semi-empirical model for the fundamental absorption edge in direct-gap semiconductors is developed and fitted to GaAs, GaSb, InAs, and InSb substrates.

15. SUBJECT TERMS
Bismuth, InAsSbBi, molecular beam epitaxy, X-ray diffraction, simulations, tetragonal distortion, biaxial strain, layer relaxation, layer tilt, photoluminescence, Nomarski, atomic force microscopy, type-II superlattices, transmission electron microscopy, photoluminescence spectroscopy, mid infrared

16. SECURITY CLASSIFICATION OF:			17. LIMITATION OF ABSTRACT	18. NUMBER OF PAGES	19a. NAME OF RESPONSIBLE PERSON
a. REPORT	b. ABSTRACT	c. THIS PAGE			Preston Webster
Unclassified	Unclassified	Unclassified	Unlimited	128	19b. TELEPHONE NUMBER *(include area code)*

(This Page Intentionally Left Blank)

TABLE OF CONTENTS

LIST OF FIGURES

Page

LIST OF FIGURES (Continued)

Page

LIST OF FIGURES (Continued)

Page

LIST OF FIGURES (Continued)

Page

LIST OF TABLES

Page

LIST OF TABLES (Continued)

Page

LIST OF TABLES (Continued)

Page

LIST OF EQUATIONS

Page

LIST OF EQUATIONS (Continued)

Page

1.0 SUMMARY

The InAsSbBi semiconductor alloy system is investigated. Bulk InAsSbBi samples with layer thicknesses ranging from 375 nm to 4 μm are grown by molecular beam epitaxy over a range of growth temperatures and V/III flux ratios. Samples are grown as random alloys with constant group V fluxes and as digital alloys with advanced shutter sequences modulating the group V fluxes. Additionally, several nBn photodetector heterostructures incorporating barrier and superlattice contact layers are examined. X-ray diffraction measurements of layer strain and photoluminescence spectroscopy measurements of low temperature bandgap energy fully determine the average chemical composition of the InAsSbBi layers, with Bi mole fractions ranging from 0.04 to 1.81%. The samples are characterized by x-ray diffraction, photoluminescence spectroscopy, Nomarski optical microscopy, and atomic force microscopy measurements. X-ray measurements of the symmetric (400) and asymmetric (511) crystal planes provide the reciprocal space coordinates of the InAsSbBi layer peaks relative to the GaSb substrates. The relaxation and tilt of the InAsSbBi layers is determined from these measurements. Relaxation ranges from 0 to 80%, and tilt ranges from 0 arcsec to 26 arcsec. Microscopy images reveal a wide degree of variation ranging from specular, smooth surfaces to rough, densely droplet covered surfaces and pitted surfaces. No clear trends in surface morphology with growth conditions are observed.

Several samples are irradiated by 63 MeV protons, and the optical performance before and after radiation treatment is assessed. Radiation treatment reduces the integrated photoluminescence by an average of 20-40%, with marginally better performance for the Bi-containing samples by about 5-10% relative to the InAsSb reference sample. A crystallographic tilt model for coherently strained epilayers grown on offcut substrates is developed and applied to InAsSbBi growths on both (100)-oriented and offcut GaSb substrates, with offcuts of 1° and 4° to (011).

The structural and optical properties of InAsSb, GaInAsSb, InAsSbBi, and GaInAsSbBi as determined by X-ray diffraction and temperature dependent photoluminescence measurements are compared. Incorporation of Bi drastically decreases both the zero-temperature bandgap by -52 meV/%Bi and increases the zero-temperature photoluminescence width intercept by 13.2 meV/%Bi. Incorporation of Ga in InAsSb and InAsSbBi provides some tensile strain allowing for a larger design area of material systems lattice matched to GaSb.

The diffusion length of mid-wave type-II InAs/InAsSb and InGaAs/InAsSb superlattices is calculated using a diffusion model and temperature dependent photoluminescence measurements. The sample structure consists of a thick mid-wave superlattice region grown on a 130 nm thick long-wave InAs/InAsSb superlattice region. The carriers in the thick mid-wave region are directly excited from a 785 nm laser and diffuse into the long-wave region allowing for radiative recombination giving rise to luminescence. The ratio of the integrated photoluminescence intensity of the long-wave over the mid-wave superlattices is used to numerically calculate the diffusion length of the mid-wave superlattice.

A kinetic model for molecular beam epitaxy growth of InAsSbBi encompassing the mechanisms of Bi desorption, incorporation, As- and Sb-assisted desorption, As- and Sb-assisted exchange, and Bi-rich droplet accumulation is developed and fitted to 210 nm thick bulk and 10 nm thick quantum well samples grown at 400-420 °C. The results indicate that As plays an important role in desorbing excess unincorporated Bi from the growth surface, and that an ultimate Bi mole fraction exists for growth of InAsSbBi lattice-matched to GaSb substrates. This ultimate Bi mole fraction decreases with increasing growth temperature.

A five-term semi-empirical absorption model is developed to describe the fundamental absorption edge in direct bandgap semiconductors. The absorption model is fitted to GaAs, GaSb, InAs, and InSb substrates measured by spectroscopic ellipsometry and the results are discussed.

2.0 INTRODUCTION

The infrared spectrum of light finds important applications in both commerce and government. Examples include medical imaging and diagnostics, autonomous vehicle sensors, telecommunications, and gas sensing among many others. Devices for these applications require high-performance materials that efficiently detect and emit infrared light. The III-AsSb material system alloyed with bismuth is attractive for these applications as it offers highly-tunable bandgaps using either thick lattice-matched bulk layers or strain-balanced superlattices grown on readily available large-area GaSb substrates[1,2] that can be processed using mature III-V processing techniques. Moreover, bismuth is the largest nonradioactive element and is relatively nontoxic and abundant compared to other nearby heavy elements such as lead, thallium, or mercury.

This work presents physical, optical, and chemical characterization results for the lesser-studied InAsSbBi quaternary alloy. This material is attractive because quaternary III-V alloys like InAsSbBi have two degrees of freedom allowing the designer the ability to independently adjust strain and bandgap energy, providing an efficient means of tuning bandgap energy without introducing high levels of detrimental strain.

This results and discussion in this report is composed of nine sections. The first five sections present x-ray diffraction, photoluminescence spectroscopy, and Nomarski optical microscopy measurements for InAsSbBi samples grown by molecular beam epitaxy at the Air Force Research Laboratory. The sections consist of (1) 1 μm thick InAsSbBi layers confined by InAsSb barriers and grown as random alloys, (2) 1 μm thick InAsSbBi layers confined by InAsSb barriers and grown as digital alloys, (3) 3 μm thick InAsSbBi layers grown directly on GaSb as random alloys, (4) “metal modulation” digital InAsSbBi alloys with thicknesses ranging from 375 – 750 nm and confined by InAsSb barriers, and (5) nBn photodetector heterostructures with 4 μm thick InAsSbBi absorber layers. The average chemical composition of each InAsSbBi sample is determined and the physical characteristics of the samples are discussed.

Section (6) is a photoluminescence spectroscopy study of radiation damaged InAsSbBi samples grown at Arizona State University by molecular beam epitaxy.

Section (7) presents a crystallographic tilt model for coherently strained epilayers grown on offcut substrates in the [011] direction. The model is applied to InAsSbBi layers grown on both (100)-oriented and offcut GaSb substrates at Arizona State University.

Section (8) compares the structural and optical properties of InAsSb, GaInAsSb, InAsSbBi, and GaInAsSbBi as determined from X-ray diffraction and temperature dependent photoluminescence measurements. The impact of Ga and Bi incorporation in InAsSb is studied.

Section (9) utilizes a diffusion model to calculate the diffusion length of mid-wave type-II InAs/InAsSb and InGaAs/InAsSb superlattices from steady state photoluminescence measurements.

Section (10) develops a kinetic model for molecular beam epitaxy growth of InAsSbBi encompassing the mechanisms of Bi desorption, incorporation, As- and Sb-assisted desorption, As- and Sb-assisted exchange, and Bi-rich droplet accumulation. The model is fitted to 210 nm thick bulk and 10 nm thick quantum well samples grown at 400-420 °C at Arizona State University, and the fitting results are discussed.

Section (11) develops a five-term semi-empirical absorption model to describe the fundamental absorption edge in direct bandgap semiconductors. The absorption model is fitted to GaAs, GaSb, InAs, and InSb substrates measured by spectroscopic ellipsometry and the results are discussed.

3.0 METHODS, ASSUMPTIONS, AND PROCEDURES

The InAsSbBi samples examined in this work are grown by molecular beam epitaxy at either the Air Force Research Laboratory (AFRL) or Arizona State University (ASU). The sample structure and cross-sections are presented in the Results and Discussion section, along with relevant growth details. The samples are grown at substrate temperatures ranging from 345 – 440 °C, higher than past work[2] which has focused on growth at comparatively low temperatures of 280 – 320 °C.

High-resolution X-ray diffraction measurements are performed to determine the layer thicknesses and in-plane strain for the InAsSbBi samples. Coupled ω-2θ scans and single ω and 2θ linescans of the (400) and (511) planes are collected using a Panalytical X'Pert Pro MRD triple-axis diffractometer. The measured intensity as a function of diffraction angle is then simulated using Panalytical X'Pert Epitaxy, a dynamical diffraction modeling program. In the simulations, the elemental X-ray scattering and dispersion parameters for Ga, In, As, and Sb, and the binary compound Poisson ratios and Debye-Waller factors for AlSb, GaSb, InAs, and InSb are provided by the X'Pert Epitaxy database.[3] The other parameters are obtained from the literature, including the scattering and dispersion parameters for Bi,[4] the lattice constants for AlSb, GaSb, InAs, and InSb,[5] and the Poisson ratio and the lattice constant for InBi.[6] The Debye-Waller factor for InBi is estimated as 1.6 by using a linear extrapolation of the values for InAs (0.837) and InSb (1.258) as function of lattice constant. It is typically assumed that the InAsSbBi layers are relatively closely lattice-matched to the GaSb substrates such that they are completely strained; i.e. not relaxed. This simplifying assumption allows the unstrained lattice constant of the InAsSbBi layer to be related to the tetragonal distortion measured by x-ray diffraction. This assumption may fail for highly-strained thick bulk layers, discussed in the text below. The InAsSbBi layers are tilted with respect to the substrate in many samples. As a result, the coupled $\omega - 2\theta$ scans do not capture the true layer peak position. To calculate an accurate out-of-plane lattice constant in the presence of layer tilt, it is necessary to measure the single ω and 2θ linescans of the (400) planes. Since layer tilt varies with rotation of the sample, the tilt that is measured is in either the $< 110 >$ or$< \bar{1}10 >$ crystallographic directions for each sample may not be the maximum tilt between the substrate and layer. Layer relaxation is computed using linescans of the (511) planes. The (511) reflection may occur at a different rotation than the direction layer tilt is measured. Thus, for the results listed below the sample relaxation listed is only an estimate of the true sample relaxation.

InAsSbBi samples are examined using temperature and excitation dependent photoluminescence spectroscopy. The samples are mounted in a closed-loop He-refrigerated cryostat and optically pumped using a modulated 785 nm laser diode. The measurements are performed at various temperatures from 13 to 295 K using average pump powers from 1 to 100 mW that provide incident intensities of 1.2 to 120 W/cm^2. The photoluminescence is collected using a Nicolet Magna-IR 760 Fourier Transform infrared spectrometer with either an InSb detector with a cutoff wavelength of 5.5 μm or mercury cadmium telluride (MCTA) detector with a cutoff wavelength of 15.5 μm. The pump laser is modulated at 50 kHz and the detector signal is fed through a phase-locked loop amplifier for improved signal-to-noise. The system optical throughput is measured and corrected using the spectrum from a Mikron M305 black body source at 800 °C.

The surface morphology is measured by Nomarski optical microscopy using an Olympus MX50 optical microscope with Nomarski prism, analyzer, and polarizer components. The surface morphology is investigated further using atomic force microscopy (AFM). The AFM measurements are performed using a Brucker multimode 8 with a lateral scan range of 153 μm and vertical scan range of 5.5 μm. The AFM images were captured with a 100 μm by 100 μm scan size using ScanAsyst-AIR tips in the Bruker ScanAsyst-in-air imaging mode.

Several InAsSbBi samples are irradiated using a 63 MeV proton beam at the UC Davis Crocker Nuclear Laboratory. 63 MeV particle energy is used because it is sufficiently high that a uniform damage profile is expected over the thicknesses of typical devices. The samples are dosed at 100 krad, equivalent to a fluence of 7.5×10^{11} protons per cm^2. The optical performance before and after irradiation is assessed using photoluminescence spectroscopy as described above.

The fundamental absorption-edge of semi-insulating GaAs and unintentionally doped GaSb, InAs, and InSb is investigated using spectroscopic ellipsometry. The spectroscopic ellipsometry measurements of GaAs and GaSb are performed using a J.A. Woollam VASE spectroscopic ellipsometer that covers 0.39 to 6.42 eV (193 to 3200 nm wavelength). Measurements of InAs and InSb are performed using a J.A. Woollam IR-VASE ellipsometer that covers 0.04 to 0.73 eV (1.7 to 30 μm). All measurements are performed at room temperature (297 K) using four incident angles (68°, 72°, 76°, and 80°) with a spectral resolution of 3.9 nm (6.3 meV for GaAs and 1.7 meV for GaSb) for the VASE measurements and 16 cm^{-1} (2.0 meV for InAs and InSb) for the IR-VASE measurements. Because the wafers are transparent below the bandgap energy, reflection from the backside of the wafer results in the collection of spurious depolarized light at the detector. Therefore, the wafer backsides are roughened sequentially with 320 and 400 grit sandpaper to diffusely scatter the backside reflections. The WVASE software[7] is used to obtain the optical constants of III-V wafers from the measured ellipsometry parameters Ψ and Δ.

4.0 RESULTS AND DISCUSSION

4.1 Characterization of 1 μm thick random alloy InAsSbBi

A total of eleven 1 μm thick random alloy InAsSbBi samples grown by molecular beam epitaxy at Air Force Research Laboratory (AFRL) are examined by x-ray diffraction and photoluminescence spectroscopy. The typical growth cross-section is shown in Figure 1. InAsSb buffer and capping layers lattice-matched to the GaSb substrate provide carrier confinement for the 1 μm thick InAsSbBi layer. The buffer layer is 450 nm thick for all samples except for L19-062 and L19-099 which are grown with 500 nm thick buffer layers. The capping layer is 100 nm thick for all samples except for L19-099 which is grown with a 30 nm thick capping layer.

The molecular beam epitaxy growth conditions are summarized in Table 1. Relatively low growth temperatures of 360 – 390 °C are used to encourage greater incorporation of Bi, which has very low solid solubility in InAs at thermal equilibrium. The group V fluxes are constant with respect to time for the InAsSbBi layer resulting in random alloy growth. Bi/In flux ratios range from 0.030 to 0.078, Sb/In flux ratios from 0.062 to 0.090, and As/In from 0.85 to 1.040.

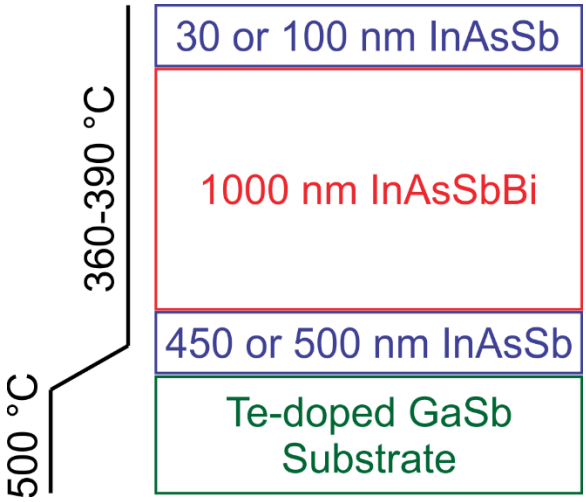

Figure 1. Sample cross-section for 1 μm thick random alloy InAsSbBi samples grown at AFRL

Table 1. Molecular beam growth conditions for 1 μm thick random alloy InAsSbBi samples grown at AFRL

Run number	Layer thickness (nm)			Growth temperature (°C)	Flux ratios		
	InAsSbBi	Buffer	Cap		Bi/In	Sb/In	As/In
L19-040	1000	450	100	390	0.030	0.062	0.975
L19-041	1000	450	100	390	0.030	0.083	0.975
L19-042	1000	450	100	390	0.030	0.077	0.975
L19-043	1000	450	100	380	0.078	0.077	0.975
L19-044	1000	450	100	380	0.078	0.077	0.955
L19-045	1000	450	100	380	0.078	0.069	1.000
L19-046	1000	450	100	380	0.078	0.076	0.990
L19-047	1000	450	100	360	0.078	0.081	0.960
L19-048	1000	450	100	360	0.078	0.090	0.970
L19-062	1000	450	100	360	0.030	0.085	1.040
L19-099	1000	450	30	380		0.090	

High-resolution coupled $\omega - 2\theta$ X-ray diffraction scans of the (400) crystal plane are acquired for all samples using a Panalytical X'Pert Pro MRD triple-axis diffractometer and simulated using the Panalytical X'Pert Epitaxy dynamical diffraction modeling program.[3] The simulations aid in the examination of the layer thicknesses and the InAsSbBi layer strain and mole fractions. A typical x-ray diffraction scan for sample L19-044 is shown in Figure 2. Two distinct intensity peaks are observed for the 1 μm thick InAsSbBi sample: the highest peak at the scan center corresponds to the GaSb substrate and lattice-matched InAsSb buffer and capping layers, while the second-highest peak indicates the 1 μm thick InAsSbBi layer. Good agreement between simulations and the measured x-ray diffraction scans enables accurate measurement of the InAsSbBi tetragonal distortion, or equivalently its unstrained lattice constant.

In the following analysis, the InAsSbBi layers are assumed to be completely strained to the GaSb substrate; i.e., the layers are not relaxed. The Matthews-Blakeslee critical thicknesses[8]

range from 140 to 4.8 μm, and therefore this assumption may fail for the most highly strained 1 μm thick samples. However, it is well-established that MBE growth at comparatively low growth temperatures (such as the 360-390 °C temperatures considered here) may exceed this critical thickness by a factor of two or more without significant relaxation. Therefore, proceeding under the assumption of completely strained layers, the in-plane biaxial strain ε_{xx} may be calculated directly from the unstrained lattice constant. The in-plane and out-of-plane biaxial strains ε_{xx} and ε_{zz} and unstrained lattice constants $a_{InAsSbBi}$ of the InAsSbBi layers are listed in Table 2.

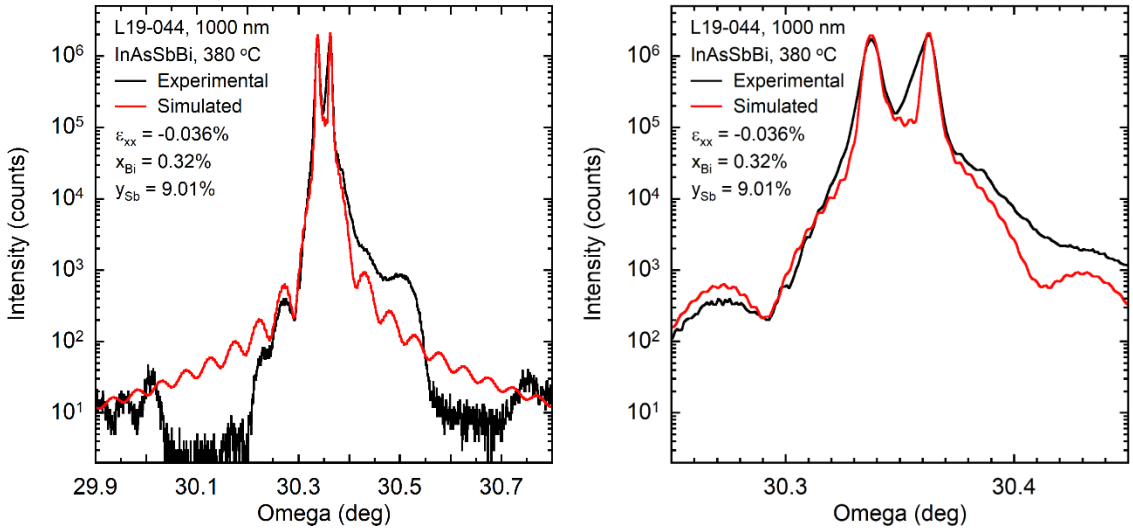

Figure 2. Coupled $\omega - 2\theta$ X-ray diffraction scans of 1 μm thick InAsSbBi sample L19-044. Average Bi and Sb mole fractions in the InAsSbBi layer are shown

The InAsSbBi samples are examined using temperature- and excitation-dependent photoluminescence spectroscopy. The samples are mounted in a closed-loop He-refrigerated cryostat and optically pumped using a modulated 785 nm laser diode. The measurements are performed at various temperatures ranging from 12 to 295 K using average pump powers ranging from 1mW to 100mW (1.2 W/cm^2 to 120 W/cm^2 incident intensity). The photoluminescence is collected using a Nicolet Magna-IR 760 Fourier Transform infrared spectrometer with an InSb detector with a cutoff wavelength of 5.5 μm, or with a mercury cadmium telluride (MCTA) detector with a cutoff wavelength of 15.5 μm. The pump laser is modulated at 50 kHz, and the detector signal is fed through a phase-locked loop amplifier for improved signal-to-noise. The system optical throughput is measured and corrected using the spectrum from a Mikron M305 black body source at 800 °C. Selected photoluminescence spectra are shown for the 1 μm thick InAsSbBi sample L19-044 below in Figure 3.

Most samples, with the exception of the relatively highly strained 390 °C – grown sample L19-040, exhibit a single well-defined photoluminescence intensity peak. This peak shows evidence of inhomogeneous broadening at the low energy side of the curve. This inhomogeneous broadening is attributable to numerous factors, including lateral composition modulation, clustering of alloy elements such as Bi or Sb, localized states associated with the Bi impurity energy level, and partial strain relaxation.

Sample L19-040 exhibits several photoluminescence peaks which are highly dependent on excitation level at low temperature. This may be a result of strain relaxation of the comparatively highly strained 1 μm InAsSbBi layer, or the photoluminescence may originate from the InAsSb buffer/capping layers. Strain relaxation by dislocations results in sample regions with differing lattice constant and therefore differing bandgap energy. Additionally, the dislocations associated

with strain relaxation may give rise to energy states within the bandgap which commonly increase rates of nonradiative recombination but may contribute to radiative recombination and photoluminescence in this InAsSbBi sample.

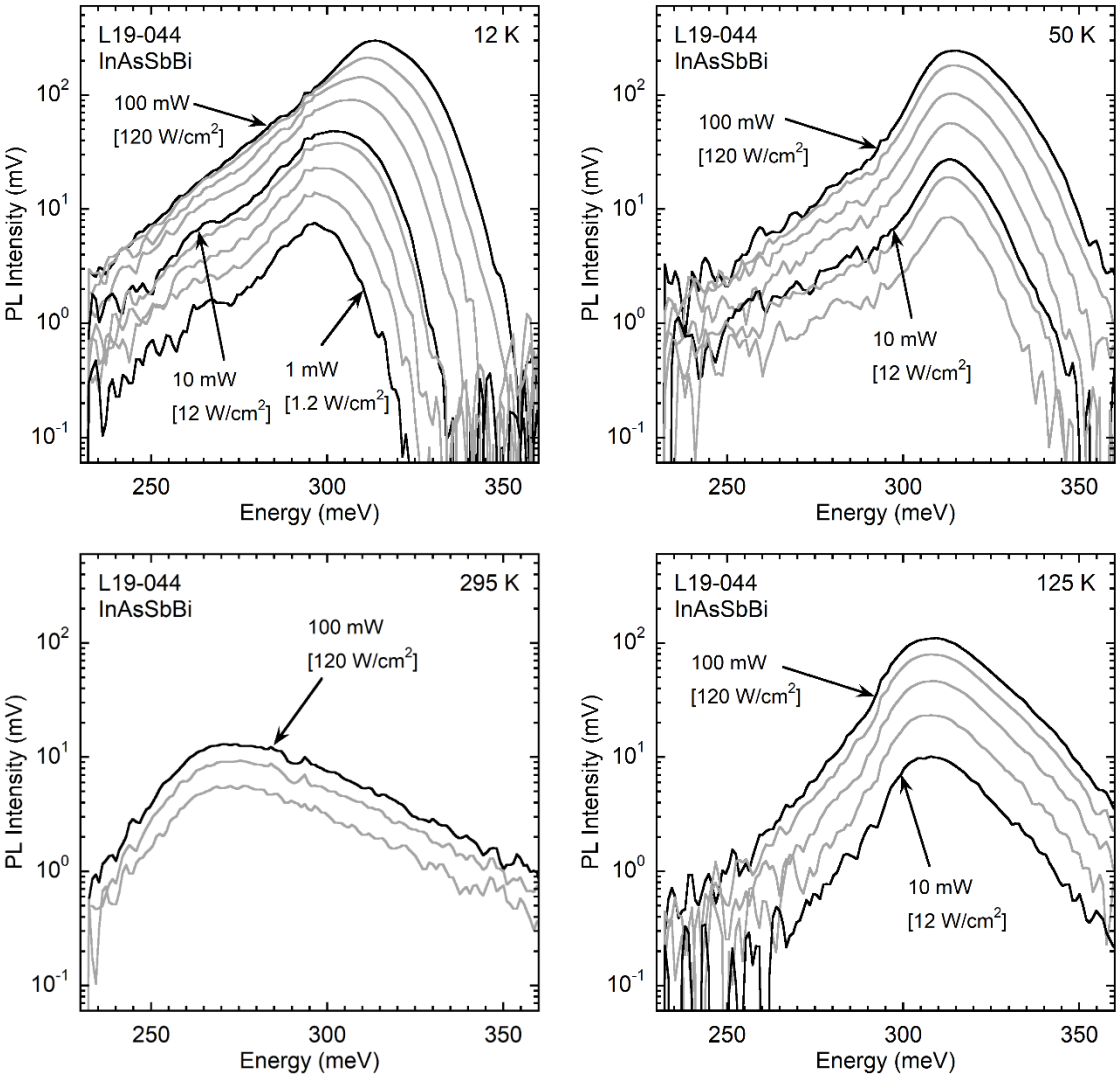

Figure 3. Clockwise from upper left: Photoluminescence spectra for 1 μm thick random alloy InAsSbBi sample L19-044 at 12 K, 50 K, 125 K, and 295 K (room temperature)

The InAsSbBi bandgap energy, E_g, is determined from the first derivative maximum of the photoluminescence energy spectrum, which is a measure of the onset of direct optical transitions involving the valence and conduction continuum bands. Practically, measurement noise poses a challenge to determining the bandgap energy from the first derivative of the data. Therefore the intensity peak and low-energy edge of the photoluminescence spectra are fitted by a Gaussian function which provides an accurate measure of the photoluminescence peak energy and width in the vicinity of the bandgap energy. The first derivative maximum of the Gaussian function is readily calculated from the fit parameters. This method of fitting and extracting the first derivative maximum energy has the advantages of filtering random noise from the spectra and precisely identifying the first derivative maximum energy; i.e. the bandgap energy.

Bandgap energy of 380 °C grown sample L19-044 determined from the first derivative maximum of the photoluminescence spectra is plotted as a function of temperature at a pump laser excitation of 100 mW in Figure 4. The photoluminescence peak energy and the peak energy minus $kT/2$ (which yields the bandgap energy in the simplified case of parabolic band structure) are also shown.

An Einstein single-oscillator equation is used to fit the temperature dependence of the bandgap energy for the 1 μm thick random alloy InAsSbBi layers[1].

$$E_g(x,y,T) = E_g(x,y,0) - \frac{S_0 k T_E}{e^{T_E/T} - 1}, \quad (1)$$

Where $E_g(x,y,0)$ is the InAsSbBi bandgap energy at 0 K, S_0 is a dimensionless coupling parameter, k is Boltzmann's constant, T_E is the Einstein temperature, and kT_E is the Einstein energy. The physical Einstein single-oscillator equation is chosen over the empirical Varshni equation as it realistically describes the influence of the zero-point motion and the temperature dependence of the phonon occupation on the bandgap energy. The coupling parameter is a measure of the strength of the electron-phonon interaction where the linear high-temperature bandgap slope is $S_0 k$. The Einstein temperature and energy are a measure of the average phonon vibration frequency of the lattice that determines the bandgap roll over due to the lattice zero-point motion, and in particular provides the temperature $T_E/2$ at which the low and high temperature bandgap asymptotes intersect. The model is fit to the data over the temperatures indicated by the solid symbols in Figure 4. The low-temperature photoluminescence that appears to originate from localized tail states within the bandgap is indicated by open symbols and is not included in the fit to the model.

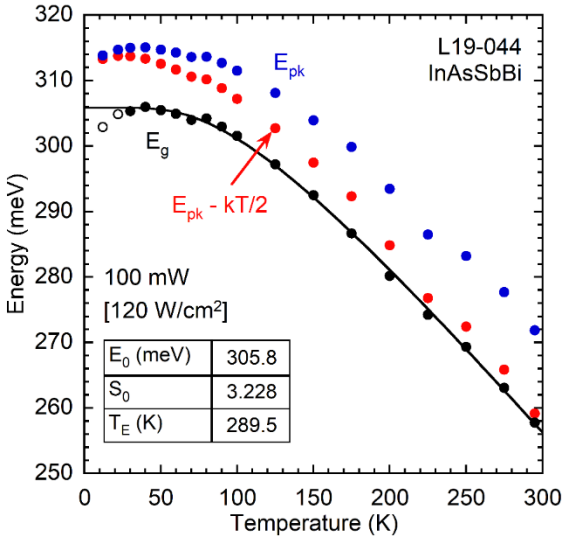

Figure 4. Bandgap energy (black circles), photoluminescence peak energy (blue circles), and peak energy minus $kT/2$ (red circles) as a function of temperature at 100 mW pump laser excitation for 380 °C grown sample L19-044. Solid black curve is fit of Einstein single oscillator model to bandgap energy data; fit parameters are summarized at lower-left of each figure

For a quaternary alloy such as InAsSbBi, at least two measurements sensitive to the chemical composition are required to fully determine the constituent As, Sb, and Bi mole fractions. X-ray diffraction measures the InAsSbBi unstrained lattice constant, while photoluminescence spectroscopy measures the InAsSbBi bandgap energy. Vegard's Law relates the InAsSbBi lattice constant $a_{InAsSbBi}$ to the Bi mole fraction x and Sb mole fraction y, shown in Eq. (2), while the

quaternary bandgap bowing model relates the bandgap energy $E_{g,InAsSbBi}$ to the mole fraction, shown in Eq. (3)[1]

$$y(x, a_{InAsSbBi}) = \frac{a_{InAsSbBi} - a_{InAs}}{a_{InSb} - a_{InAs}} - x\frac{a_{InBi} - a_{InAs}}{a_{InSb} - a_{InAs}} \quad (2)$$

$$E_{g,InAsSbBi}(x,y) = (1-x-y)E_{g,InAs} + yE_{g,InSb} + xE_{g,InBi} - [y(1-x-y)b_{g,InAsSb} + x(1-x-y)b_{g,InAsBi} + xyb_{g,InSbBi}]\,. \quad (3)$$

The resulting system of 2 equations and 2 unknowns may be solved to completely determine the average Bi mole fraction x and Sb mole fraction y. The results of the x-ray diffraction and photoluminescence spectroscopy measurements of InAsSbBi composition are summarized below in Table 2.

Table 2. Characterization summary for 1 µm thick random alloy InAsSbBi samples measured by x-ray diffraction and photoluminescence spectroscopy. From left: sample number, growth temperature, in-plane biaxial strain ε_{xx}, out-of-plane biaxial strain ε_{xx}, unstrained InAsSbBi lattice constant $a_{InAsSbBi}$, low-temperature bandgap energy $E_{g,InAsSbBi}$, and average group V mole fractions

Sample	Growth temperature (°C)	Biaxial strain (%)		InAsSbBi lattice constant (Å)	Low-temperature bandgap energy (eV)	Mole fractions		
		ε_{xx}	ε_{zz}			Bi	Sb	As
L19-040	390	0.102	-0.111	6.0897	0.3003	0.007	0.066	0.928
L19-041	390	-0.093	0.102	6.1016	0.3098	0.001	0.102	0.897
L19-042	390	-0.029	0.031	6.0976	0.3146	0.001	0.092	0.907
L19-043	380	0.043	-0.046	6.0933	0.3115	0.003	0.079	0.918
L19-044	380	-0.036	0.040	6.0981	0.3058	0.003	0.090	0.906
L19-045	380	-0.013	0.015	6.0967	0.3082	0.003	0.087	0.910
L19-046	380	0.096	-0.104	6.0901	0.3200	0.002	0.073	0.925
L19-047	360	-0.037	0.040	6.0981	0.2946	0.006	0.087	0.907
L19-048	360	-0.038	0.042	6.0982	0.2956	0.006	0.088	0.907
L19-062	360	-0.021	0.023	6.0972	0.2863	0.008	0.081	0.911
L19-099	380	-0.010	0.011	6.0965	0.3088	0.002	0.090	0.908

One-dimensional X-ray diffraction line scans passing through the GaSb substrate and InAsSbBi layer peaks along the ω and 2θ scan directions are acquired from the symmetric (400) and asymmetric (511) reflections using the Panalytical X'Pert Pro MRD triple-axis diffractometer. The resulting line scans are fitted using a Gaussian function in MATLAB R2020a[9] to identify the reciprocal space coordinates of the peaks with an accuracy of ± 0.36 arcseconds. These scans are used to compute the out-of-plane lattice constant while accounting for a tilted layer. Similarly, the in-plane strain and lattice constant are calculated using the ω and 2θ linescans of the (511) planes.

In the case of sample L19-044, the tilt is measured in the $< \bar{1}10 >$ direction. After calibrating the layer peak position according to the substrate offsets from the Bragg angles for the (400) planes of GaSb, the tilt is measured as $\theta - \omega = -5.4$ arcseconds. Similarly for the (511) planes, the layer peak position is calibrated according to the substrate offsets from the Bragg angles for the (511) planes of GaSb. The layer peak position's ω and 2θ angles are used to calculate the in-plane and out-of-plane lattice constants and subsequently the relaxation of the InAsSbBi layer. The relaxation is computed to be 0.97%, a relatively small value in comparison to other 1 µm thick random alloy InAsSbBi samples. As mentioned above, the relaxation calculation does not account for the maximum tilt in the layer.

The relaxation, tilt, and measured tilt direction are listed for each sample in Table 3. Many of the 1 µm thick random alloy InAsSbBi samples exhibit relatively low levels of tilt and relaxation. This indicates the InAsSbBi layers are nearly lattice matched to the GaSb substrate with a low

density of misfit dislocations. Sharp, narrow x-ray diffraction peaks are measured for most 1 μm random alloy samples indicating homogeneous composition in the InAsSbBi layer, with small strain gradients in the lateral and vertical directions.

Nomarski optical microscopy images are acquired to investigate the surface morphology of the 1 μm thick random alloy InAsSbBi samples. Images are acquired at magnifications of 100x, 400x, and 1000x. The samples are classified as either "specular" or "rough" in Table 3 on the basis of visual inspection of the Nomarski images. All 1 μm thick random alloy InAsSbBi samples are observed to be free of visible surface features or roughness. Figure 5 shows the Nomarski image at 100x magnification for specular, droplet-free sample L19-044. The As/In flux ratios range from 0.955 to 1.040 for these specular droplet-free samples, pointing to the important role that excess As flux plays in desorbing excess unincorporated Bi from the surface during growth.[1]

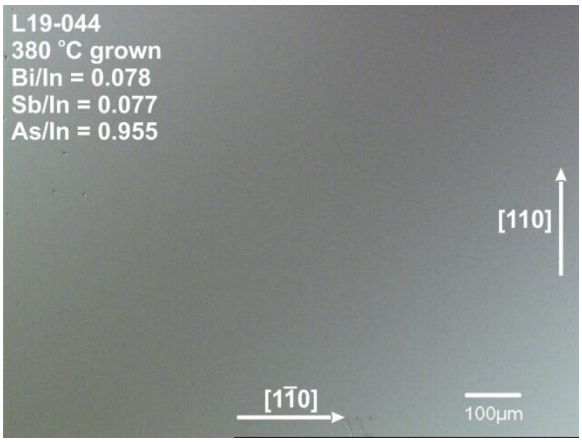

Figure 5. Nomarski optical microscopy image acquired at 100x magnification for sample L19-044, typical of the surface morphology observed on all 1 μm thick random alloy InAsSbBi samples

Table 3. Molecular beam epitaxy growth conditions, strain relaxation, layer tilt, and surface morphology of 1 μm thick random alloy InAsSbBi samples

Sample	Growth temperature (°C)	V/In flux ratios			Relaxation (%)	Tilt (arcsec)	Tilt measurement direction	Nomarski morphology
		Bi/In	Sb/In	As/In				
L19-040	390	0.030	0.062	0.975	1.4	-3.6	$< 110 >$	Smooth
L19-041	390	0.030	0.083	0.975	16.4	-4.5	$< \bar{1}10 >$	Smooth
L19-042	390	0.030	0.077	0.975	1.4	-0.7	$< 110 >$	Smooth
L19-043	380	0.078	0.077	0.975	3.55	-2.2	$< 110 >$	Smooth
L19-044	380	0.078	0.077	0.955	0.97	-0.5	$< \bar{1}10 >$	Smooth
L19-045	380	0.078	0.069	1.000	36.6	0.4	$< \bar{1}10 >$	Smooth
L19-046	380	0.078	0.076	0.990	32.24	1.3	$< 110 >$	Smooth
L19-047	360	0.078	0.081	0.960	6.34	-25.4	$< \bar{1}10 >$	Smooth
L19-048	360	0.078	0.090	0.970	1.8	-3.4	$< 110 >$	Smooth
L19-062	360	0.030	0.085	1.040	6.8	-1.1	$< 110 >$	Smooth
L19-099	380		0.090		0.5	-1.5	$< 110 >$	Smooth

4.2 Characterization of 3 µm thick random alloy InAsSbBi

Two 3 µm thick random alloy InAsSbBi samples grown by molecular beam epitaxy at Air Force Research Laboratory (AFRL) are examined by x-ray diffraction and photoluminescence spectroscopy. The growth cross-section is shown in Figure 6. A 10 nm lattice-matched InAsSb buffer layer is grown on the GaSb substrate, followed by the 3 µm thick InAsSbBi layer. Both samples are grown at 440 °C. Bi/In flux ratios of 0.060 and 0.030, Sb/In flux ratios of 0.096 and 0.084, and As/In flux ratios of 1.030 and 1.040 are used for samples L19-105 and L20-002 respectively. The molecular beam epitaxy growth conditions are summarized in Table 4.

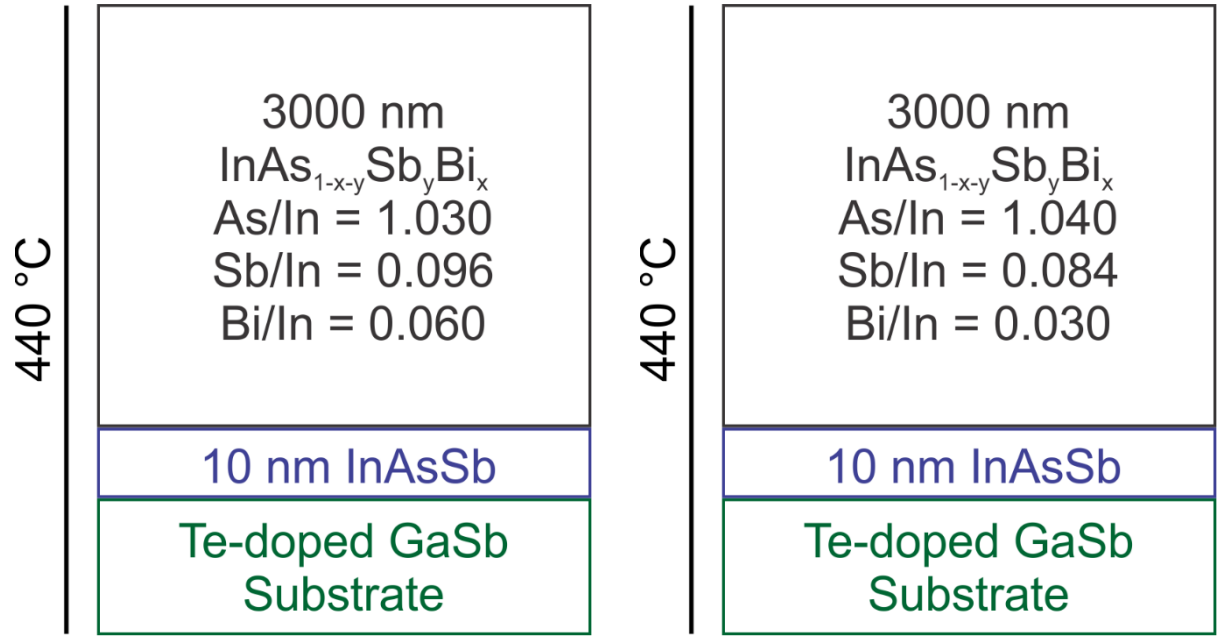

Figure 6. Sample cross-sections for 3 µm thick random alloy InAsSbBi samples grown at AFRL. Left: sample L19-105. Right: sample L20-002

Table 4. Molecular beam growth conditions for 3 µm thick random alloy InAsSbBi samples grown at AFRL

Run number	Layer thickness (nm)		Growth temperature (°C)	Flux ratios		
	InAsSbBi	Buffer		Bi/In	Sb/In	As/In
L19-105	3000	10	440	0.060	0.096	1.030
L20-002	3000	10	440	0.030	0.084	1.040

As in Section (1), high-resolution coupled $\omega - 2\theta$ X-ray diffraction scans of the (400) crystal plane are acquired for the 3 µm thick random alloy samples using a Panalytical X'Pert Pro MRD triple-axis diffractometer and simulated using the Panalytical X'Pert Epitaxy dynamical diffraction modeling program.[3] X-ray diffraction scans are shown for both 3 µm thick samples in Figure 7. Poor agreement between measurement and simulation is realized in both samples. The measured InAsSbBi layer diffraction peaks exhibit low intensity and significant broadening, possible indicators of a high density of dislocations, partial or full strain relaxation, and poor interfacial quality between the layer and substrate. This results in a high degree of uncertainty on the average InAsSbBi lattice constant determined from the x-ray diffraction pattern.

In the following analysis, the InAsSbBi layers are assumed to be completely strained to the GaSb substrate; i.e., the layers are not relaxed. The in-plane and out-of-plane biaxial strains ε_{xx} and ε_{zz} and unstrained lattice constants $a_{InAsSbBi}$ of the InAsSbBi layers are listed in Table 5.

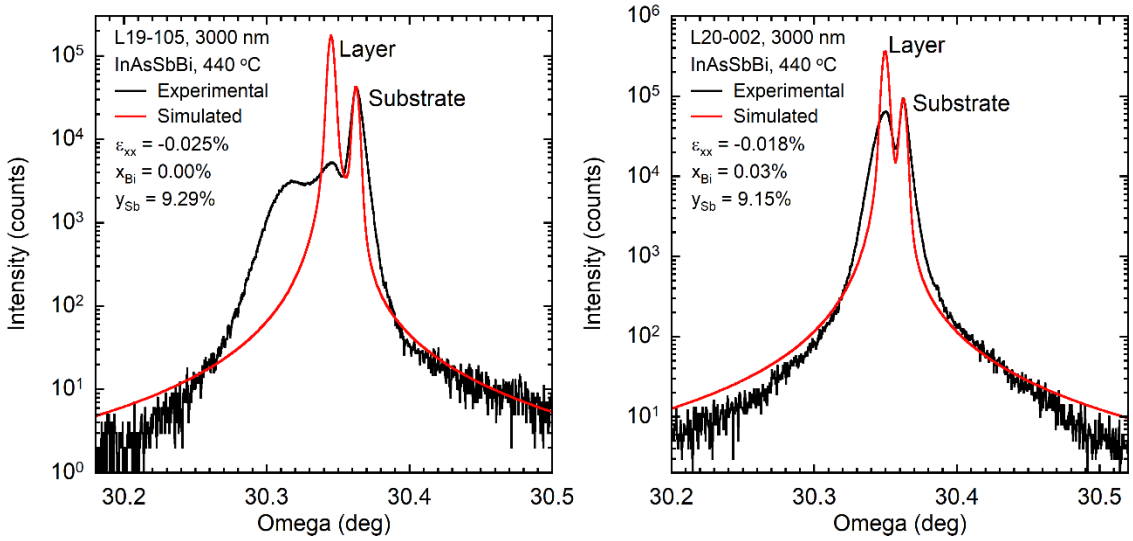

Figure 7. Coupled $\omega - 2\theta$ X-ray diffraction scans of 3 µm thick random alloy InAsSbBi samples L19-105 (left) and L20-002 (right). Average Bi and Sb mole fractions in the InAsSbBi layer are shown

As in Section (1), the 3 µm thick InAsSbBi samples are examined using temperature- and excitation-dependent photoluminescence spectroscopy. The experimental setup is identical to that described in Section (1). Selected photoluminescence spectra are shown for the 3 µm thick InAsSbBi samples L19-105 and L20-002 in Figure 8. Both samples exhibit a single well-defined photoluminescence intensity peak. In comparison to the 1 µm thick InAsSbBi samples grown at temperatures from 360 – 390 °C, the 3 µm thick InAsSbBi samples grown at 440 °C exhibit sharp photoluminescence peaks with comparatively narrow linewidth. This absence of inhomogeneous broadening suggests improved material quality on a microscopic scale and reduction of broadening mechanisms including point defects, clustering of alloy elements such as Bi or Sb, and localized states associated with the Bi impurity energy level.

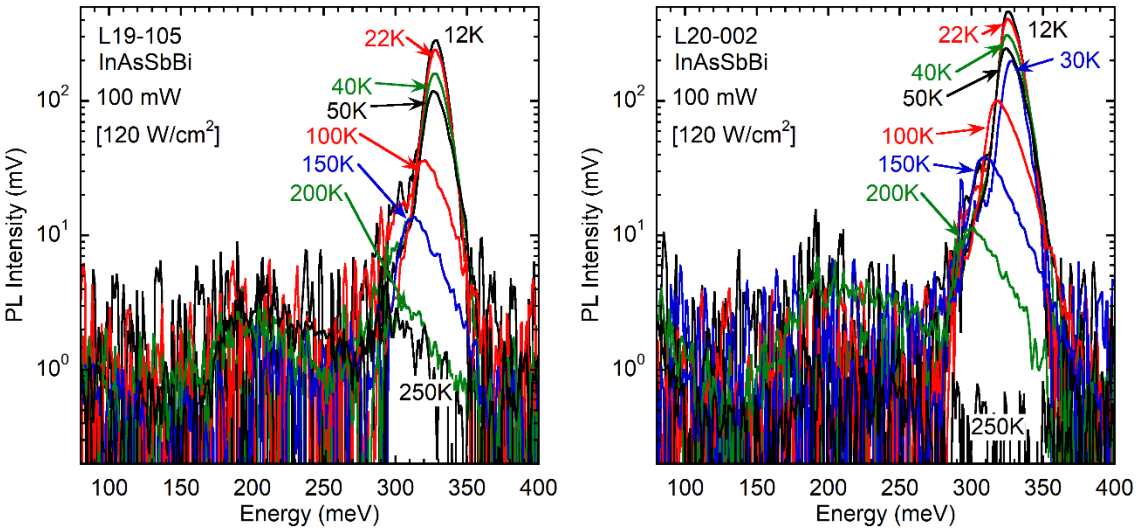

Figure 8. Photoluminescence spectra for 3 µm thick random alloy InAsSbBi samples L19-105 (left) and L20-002 (right) at 100 mW pump laser excitation power (120 W/cm²)

As in Section (1), the InAsSbBi bandgap energy is determined from the first derivative maximum of the photoluminescence energy spectrum. Bandgap energy of both 3 µm thick InAsSbBi samples determined from the first derivative maximum of the photoluminescence spectra is plotted as a function of temperature at a pump laser excitation of 100 mW in Figure 9. The photoluminescence peak energy and the peak energy minus $kT/2$ (which yields the bandgap energy in the simplified case of parabolic band structure) are also shown. The Einstein single-oscillator model Eq. (1) is fit to the data over the temperatures indicated by the solid symbols in Figure 9, yielding the low-temperature bandgap energy E_0.

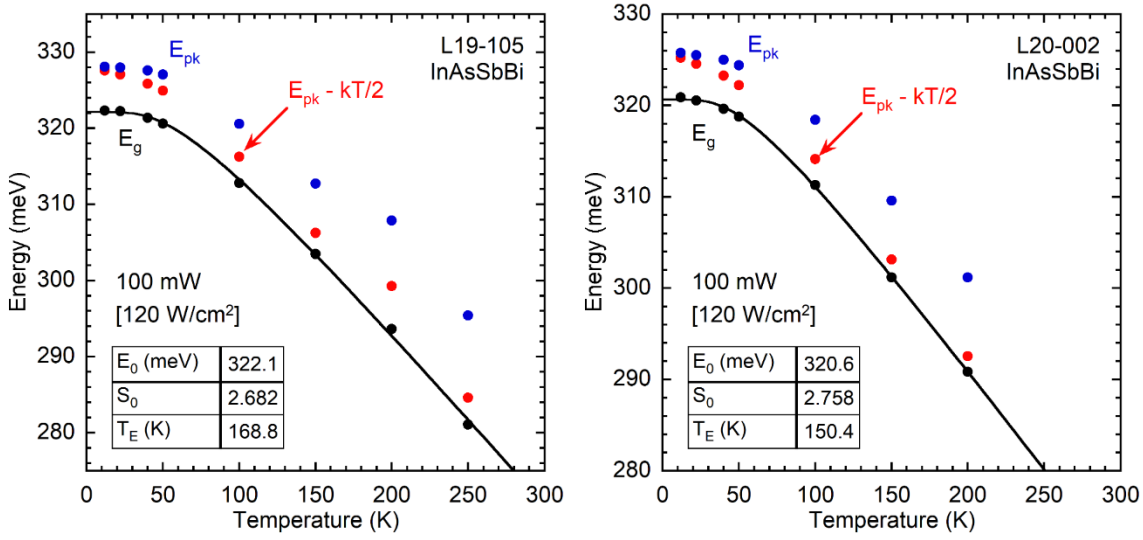

Figure 9. Bandgap energy (black circles), photoluminescence peak energy (blue circles), and peak energy minus $kT/2$ (red circles) as a function of temperature at 100 mW pump laser excitation for 440 °C grown samples L19-105 (left) and L20-002 (right). Solid black curve is fit of Einstein single oscillator model to bandgap energy data; fit parameters are summarized at lower-left of each figure

As in Section (1), Vegard's Law for the InAsSbBi lattice constant, Eq. (2), and the InAsSbBi bandgap bowing Eq. (3) are used to determine the average composition of the 3 μm thick random alloy InAsSbBi layers. The results of the x-ray diffraction and photoluminescence spectroscopy measurements of InAsSbBi composition are summarized below in Table 5. It is evident that Bi incorporation is vanishingly small at the 440 °C growth temperature with average mole fraction of ≤ 0.3%.

Table 5. Characterization summary for 3 μm thick random alloy InAsSbBi samples measured by x-ray diffraction and photoluminescence spectroscopy. From left: sample number, growth temperature, in-plane biaxial strain ε_{xx}, out-of-plane biaxial strain ε_{xx}, unstrained InAsSbBi lattice constant $a_{InAsSbBi}$, low-temperature bandgap energy $E_{g,InAsSbBi}$, and average group V mole fractions

Sample	Growth temperature (°C)	Biaxial strain (%)		InAsSbBi lattice constant (Å)	Low-temperature bandgap energy (eV)	Mole fractions		
		ε_{xx}	ε_{zz}			Bi	Sb	As
L19-105	440	-0.025	0.027	6.0974	0.3221	0.000	0.093	0.907
L20-002	440	-0.018	0.020	6.0970	0.3206	0.003	0.088	0.909

One-dimensional X-ray diffraction line scans passing through the GaSb substrate and InAsSbBi layer peaks along the ω and 2θ scan directions are acquired from the symmetric (400) and asymmetric (511) reflections using the Panalytical X'Pert Pro MRD triple-axis diffractometer. The resulting line scans are fitted using a Gaussian function in MATLAB R2020a[9] to identify the reciprocal space coordinates of the peaks with an accuracy of ± 0.36 arcseconds. These scans are used to compute the out-of-plane lattice constant while accounting for a tilted layer. Similarly, the in-plane strain and lattice constant are calculated using the ω and 2θ linescans of the (511) planes.

The relaxation, tilt, and tilt direction are listed for each sample in Table 6. The tilt angle between the substrate and layer for samples L19-105 and L20-002 is 0.4 and 3.4 arcseconds, respectively. Both samples are measured in the $< 110 >$ direction. The degree of layer relaxation for both samples is calculated to be 0.1% and 13.7%, respectively. The relaxation measurements indicate that sample L19-105 is lattice matched to the GaSb substrate while sample L20-002 is slightly relaxed. As mentioned above, the relaxation calculations do not account for the maximum tilt between the substrate and layer.

Nomarski optical microscopy images are acquired to investigate the surface morphology of the 1 μm thick random alloy InAsSbBi samples. Images are acquired at magnifications of 100x, 400x, and 1000x. Both samples are free of observable surface features or defects at all magnifications and therefore are classified as "smooth" in Table 6. Images at 100x magnification for both 3 μm thick random alloy InAsSbBi samples are shown in Figure 10.

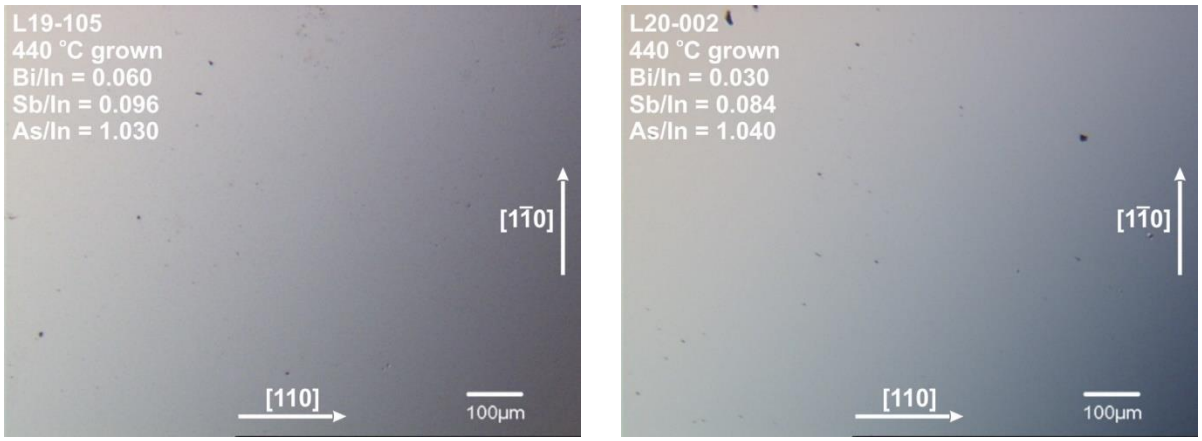

Figure 10. Nomarski optical microscopy images acquired at 100x magnification for samples L19-105 (left) and L20-002 (right). Both samples are free of observable surface features at all magnifications

Table 6. Molecular beam epitaxy growth conditions, strain relaxation, layer tilt, and surface morphology of 3 μm thick random alloy InAsSbBi samples

Sample	Growth temperature (°C)	V/In flux ratios			Relaxation (%)	Tilt (arcsec)	Tilt measurement direction	Nomarski morphology
		Bi/In	Sb/In	As/In				
L19-105	440	0.060	0.096	1.030	0.1	0.4	< 110 >	Smooth
L20-002	440	0.030	0.084	1.040	13.7	3.4	< 110 >	Smooth

4.3 Characterization of 1 μm thick digital alloy InAsSbBi

A total of seven 1 μm thick digital alloy InAsSbBi samples grown by molecular beam epitaxy at Air Force Research Laboratory (AFRL) are examined by x-ray diffraction and photoluminescence spectroscopy. The typical growth cross-section is shown in Figure 11. InAsSb buffer and capping layers lattice-matched to the GaSb substrate provide carrier confinement for the 1 μm thick InAsSbBi layer. The Sb shutter is sequenced to grow the InAsSbBi layer as a digital alloy composed of alternating layers of InAsBi/InAsSbBi with period of 1 nm and effective InAsBi layer thicknesses ranging from 0.10 – 0.56 nm. The buffer and capping layers are 450 nm thick and 100 nm thick respectively for all samples.

The molecular beam epitaxy growth conditions and InAsBi/InAsSbBi constituent layer thicknesses are summarized in Table 7. Relatively low growth temperatures of 345 – 360 °C are used to encourage greater incorporation of Bi, which has very low solid solubility in InAs at thermal equilibrium. The effective group V fluxes for the digital alloy growth range from 0.030 to 0.156 for Bi/In, from 0.070 to 0.095 for Sb/In, and from 0.85 to 0.99 for As/In.

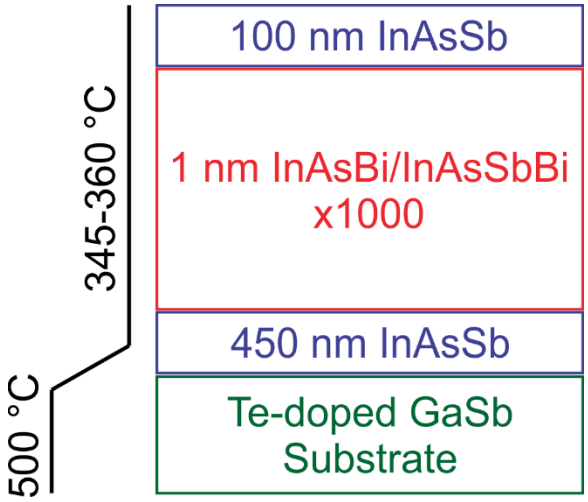

Figure 11. Sample cross-section for 1 µm thick digital alloy InAsSbBi samples grown at AFRL

Table 7. Molecular beam growth conditions for 1 µm digital alloy InAsSbBi samples grown at AFRL

Run number	Total layer thickness (nm)			Constituent layer thickness (nm)		Growth temperature (°C)	Effective flux ratios		
	InAsSbBi	Buffer	Cap	InAsBi	InAsSbBi		Bi/In	Sb/In	As/In
L19-049	1000	450	100	0.50	0.50	360	0.078	0.094	0.970
L19-050	1000	450	100	0.56	0.44	360	0.078	0.095	0.990
L19-051	1000	450	100	0.56	0.44	345	0.156	0.095	0.970
L19-054	1000	450	100	0.56	0.44	360	0.078	0.095	0.900
L19-056	1000	450	100	0.10	0.90	360	0.078	0.084	0.850
L19-057	1000	450	100	0.20	0.80	360	0.078	0.070	0.860
L19-059	1000	450	100	0.10	0.90	360	0.030	0.086	0.990

As in Section (1) high-resolution coupled $\omega - 2\theta$ X-ray diffraction scans of the (400) crystal plane are acquired for all samples using a Panalytical X'Pert Pro MRD triple-axis diffractometer and simulated using the Panalytical X'Pert Epitaxy dynamical diffraction modeling program [3]. A typical x-ray diffraction scan for sample L19-054 is shown in Figure 12. Two intensity peaks are observed for the 1 µm thick InAsSbBi sample: the highest peak at the scan center corresponds to the GaSb substrate and lattice-matched InAsSb buffer and capping layers, while the second-highest peak indicates the 1 µm thick InAsSbBi layer. Poor agreement between measurement and simulation is realized in most samples. The measured InAsSbBi layer diffraction peaks exhibit low intensity and significant broadening, possible indicators of a high density of dislocations, partial or full strain relaxation, and poor interfacial quality between the layer and substrate. This results in a high degree of uncertainty on the average InAsSbBi lattice constant determined from the x-ray diffraction pattern. Assuming completely strained material (i.e. not relaxed), the in-plane and out-of-plane biaxial strains ε_{xx} and ε_{zz} and unstrained lattice constants $a_{InAsSbBi}$ of the InAsSbBi layers are listed in Table 8.

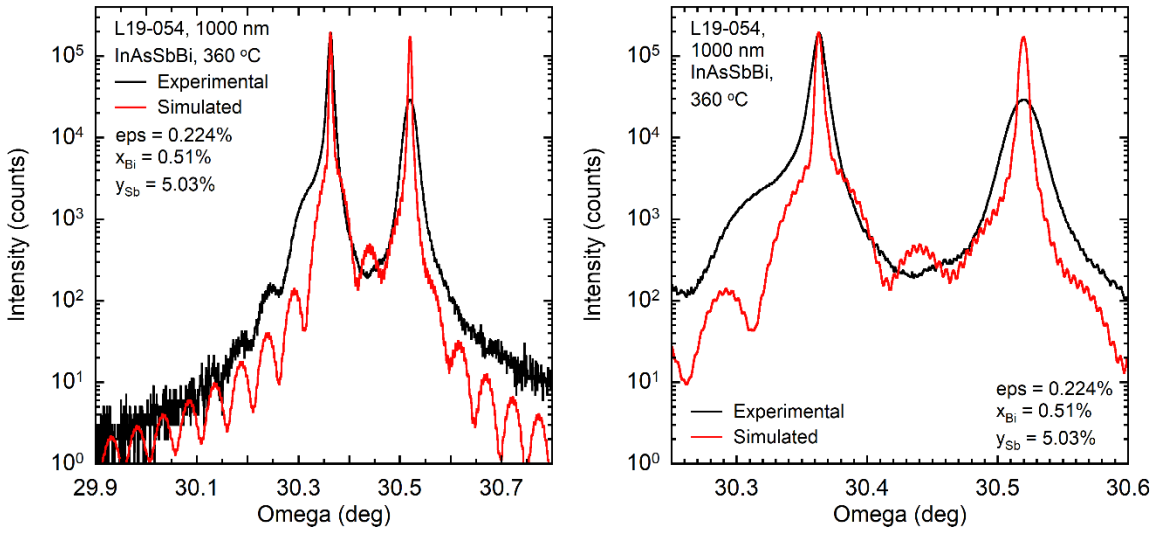

Figure 12. Coupled $\omega - 2\theta$ X-ray diffraction scans of 1 µm thick digital alloy InAsSbBi sample L19-054. Average Bi and Sb mole fractions in the InAsSbBi layer are shown

As in Section (1) the InAsSbBi samples are examined using temperature- and excitation-dependent photoluminescence spectroscopy. Selected photoluminescence spectra are shown for the 1 µm thick digital alloy InAsSbBi sample L19-054 below in Figure 13. The samples exhibit a single well-defined photoluminescence intensity peak. This peak shows evidence of inhomogeneous broadening at the low energy side of the curve. This inhomogeneous broadening is attributable to numerous factors, including lateral composition modulation, clustering of alloy elements such as Bi or Sb, localized states associated with the Bi impurity energy level, and partial strain relaxation.

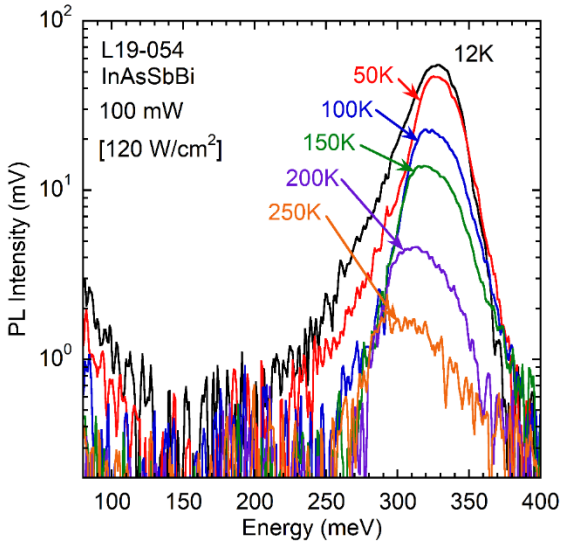

Figure 13. Photoluminescence spectra for 1 µm thick digital alloy InAsSbBi sample L19-054 at 100 mW pump laser excitation power (120 W/cm^2)

As in Section (1) the InAsSbBi bandgap energy, E_g, is determined from the first derivative maximum of the photoluminescence energy spectrum. Bandgap energy of 360 °C grown sample

L19-054 determined from the first derivative maximum of the photoluminescence spectra is plotted as a function of temperature at a pump laser excitation of 100 mW in Figure 14. The photoluminescence peak energy and the peak energy minus $kT/2$ (which yields the bandgap energy in the simplified case of parabolic band structure) are also shown. The Einstein single oscillator model fit of Eq. (1) is shown as a solid black line. The low-temperature photoluminescence that appears to originate from localized tail states within the bandgap is indicated by open symbols and is not included in the fit to the model.

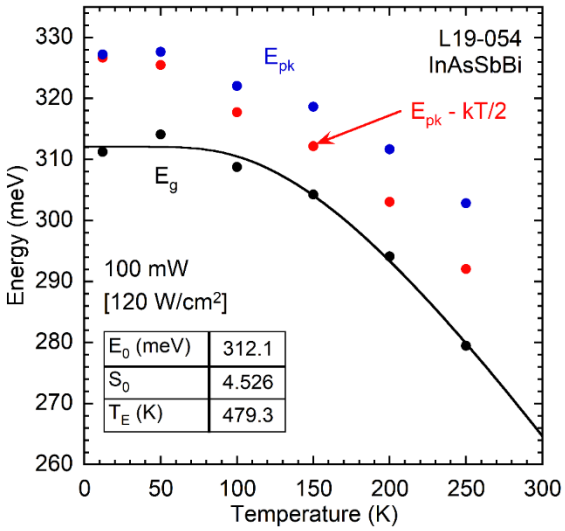

Figure 14. Bandgap energy (black circles), photoluminescence peak energy (blue circles), and peak energy minus $kT/2$ (red circles) as a function of temperature at 100 mW pump laser excitation for 360 °C grown sample L19-054. Solid black curve is fit of Einstein single oscillator model to bandgap energy data; fit parameters are summarized at lower-left of each figure

As in Section (1), Vegard's Law for the InAsSbBi lattice constant, Eq. (2), and the InAsSbBi bandgap bowing Eq. (3) are used to determine the average composition of the digital alloy InAsSbBi layers. The results of the x-ray diffraction and photoluminescence spectroscopy measurements of InAsSbBi composition are summarized below in Table 8.

Table 8. Characterization summary for 1 µm thick digital alloy InAsSbBi samples measured by x-ray diffraction and photoluminescence spectroscopy. From left: sample number, growth temperature, in-plane biaxial strain ε_{xx}, out-of-plane biaxial strain ε_{xx}, unstrained InAsSbBi lattice constant $a_{InAsSbBi}$, low-temperature bandgap energy $E_{g,InAsSbBi}$, and average group V mole fractions

Sample	Growth temperature (°C)	Biaxial strain (%)		InAsSbBi lattice constant (Å)	Low-temperature bandgap energy (eV)	Mole fractions		
		ε_{xx}	ε_{zz}			Bi	Sb	As
L19-049	360	0.142	-0.154	6.0873	0.3136	0.004	0.064	0.932
L19-050	360	0.185	-0.201	6.0846	0.3070	0.006	0.055	0.939
L19-051	345	0.182	-0.198	6.0848	0.3088	0.005	0.056	0.939
L19-054	360	0.224	-0.243	6.0823	0.3121	0.005	0.050	0.945
L19-056	360	-0.072	0.078	6.1003	0.2714	0.011	0.086	0.904
L19-057	360	0.001	-0.001	6.0958	0.2960	0.007	0.081	0.913
L19-059	360	-0.104	0.113	6.1022	0.2690	0.010	0.091	0.899

As in Section (1), one-dimensional X-ray diffraction line scans passing through the GaSb substrate and InAsSbBi layer peaks along the ω and 2θ scan directions are acquired from the symmetric (400) and asymmetric (511) reflections using the Panalytical X'Pert Pro MRD triple-

axis diffractometer. The resulting line scans are fitted using a Gaussian function in MATLAB R2020a[9] to identify the reciprocal space coordinates of the peaks with an accuracy of ± 0.36 arcseconds. These scans are used to compute the out-of-plane lattice constant while accounting for a tilted layer. Similarly, the in-plane strain and lattice constant are calculated using the ω and 2θ linescans of the (511) planes.

The relaxation and tilt are listed for each sample in Table 9. The tilt angle between the substrate and layer for sample L19-054 is 66.2 arcseconds in the $< \bar{1}10 \geq$ direction. The degree of layer relaxation is computed to be 18.8% indicating that it is slightly relaxed. As mentioned above, the relaxation calculation does not account for the maximum tilt in the layer. Many of the 1 µm thick digital alloy InAsSbBi samples exhibit relatively high levels of tilt and relaxation. A large tilt angle between the substrate and layer could be caused by misfit dislocations at the interfaces. The dislocations might be introduced at the many interfaces that exist within the digital alloy since layers of InAsBi and InAsSbBi are grown alternately with thicknesses of 0.56 nm and 0.44 nm respectively.

As in Section (1), Nomarski optical microscopy images are acquired to investigate the surface morphology of the 1 µm thick digital alloy InAsSbBi samples. All samples except for L19-050 and L19-051 exhibit surface roughness and droplet-like features. A typical Nomarski image at 100x magnification for rough, droplet-covered sample L19-054 is shown in Figure 15. The droplet-like surface features observed in rough samples including L19-054 are thought to be composed primarily of excess unincorporated Bi[10,11]. The formation of these droplets is thought to be due primarily to the comparatively low As/In flux ratios of 0.850 to 0.990 used. The low excess As flux reduces the rate of As-assisted Bi desorption from the growth surface resulting in accumulation of unincorporated Bi on the growth surface.

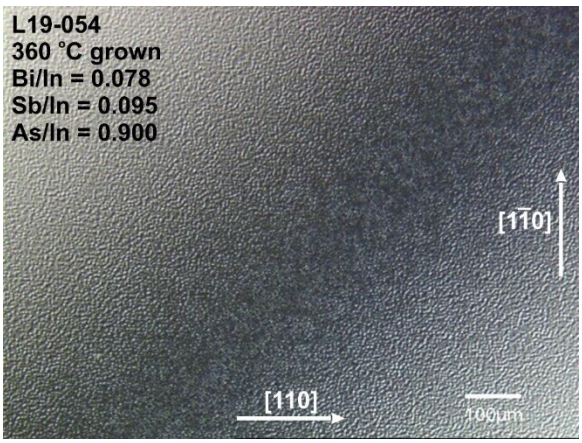

Figure 15. Nomarski optical microscopy image acquired at 100x magnification for sample L19-054

Table 9. Molecular beam epitaxy growth conditions, strain relaxation, layer tilt, and surface morphology of 1 μm thick digital alloy InAsSbBi samples

Sample	Growth temperature (°C)	V/In flux ratios			Relaxation (%)	Tilt (arcsec)	Tilt measurement direction	Nomarski morphology
		Bi/In	Sb/In	As/In				
L19-049	360	0.078	0.094	0.970	81.6	-65.5	$< 110 >$	Rough
L19-050	360	0.078	0.095	0.990	64.1	-9.7	$< \bar{1}10 >$	Smooth
L19-051	345	0.156	0.095	0.970	71.5	-26.5	$< 110 >$	Smooth
L19-054	360	0.078	0.095	0.900	18.8	-66.2	$< 110 >$	Rough
L19-056	360	0.078	0.084	0.850	5.3	0.7	$< \bar{1}10 >$	Rough
L19-057	360	0.078	0.070	0.860	55.2	5.2	$< \bar{1}10 >$	Rough
L19-059	360	0.030	0.086	0.990	15.5	-2.9	$< 110 >$	Rough

4.4 Characterization of metal-modulation digital alloy InAsSbBi

A total of twelve “metal-modulation” digital alloy InAsSbBi samples grown by molecular beam epitaxy at Air Force Research Laboratory (AFRL) are examined by x-ray diffraction and photoluminescence spectroscopy. The metal-modulation technique consists of shutter sequencing to grow alternating layers of InBi and AsSb. In and Bi are co-deposited and then As and Sb are co-deposited in the absence of In flux. Total InAsSbBi layer thicknesses range from 250 – 750 nm with most samples grown at 500 nm thickness. The period of the InBi/AsSb digital alloy ranges from 0.45 – 0.60 nm with most samples grown at 0.6 nm period. The InBi layer thicknesses range from 0.15 – 0.46 nm and the AsSb equivalent layer thicknesses are fixed at 0.30 nm. The total number of InBi/AsSb repeats is 1641 for all samples. Additionally, 90 second growth interrupts are implemented at intervals of either 410 or 328 repeats for several samples.

The typical growth cross-section is shown in Figure 16. InAsSb buffer and capping layers lattice-matched to the GaSb substrate provide carrier confinement for the InAsSbBi layer. The buffer layer thickness is 360 nm for all samples and capping layer thickness ranges from 30 – 100 nm. The molecular beam epitaxy growth conditions are summarized in Table 10. The InAsSbBi growth temperature ranges from 380 – 420 °C. The effective group V fluxes for the digital alloy growth range from 0.030 to 0.129 for Bi/In, from 0.078 to 0.100 for Sb/In, and from 0.970 to 1.350 for As/In.

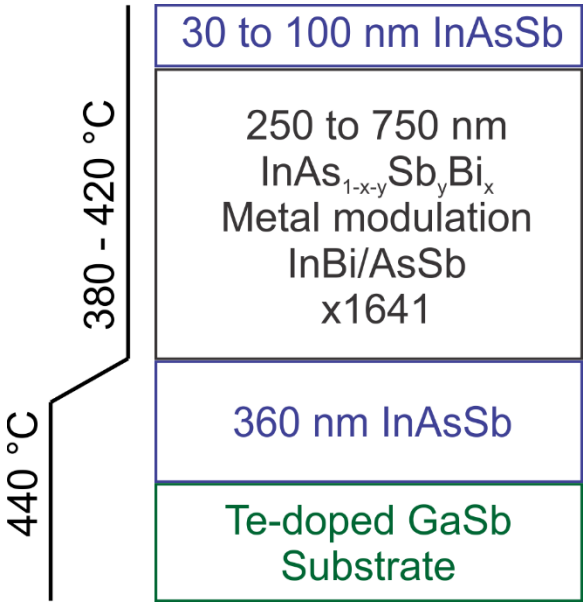

Figure 16. Sample cross-section for metal-modulation digital alloy InAsSbBi samples grown at AFRL

Table 10. Molecular beam growth conditions for metal-modulation digital alloy InAsSbBi samples grown at AFRL

Run number	Layer thickness (nm)					Growth temperature (°C)	Effective flux ratios			Growth interrupts
	InAsSbBi	Cap	InBi/AsSb period	InBi	AsSb		Bi/In	Sb/In	As/In	
L19-075	500	100	0.60	0.30	0.30	380	0.030	0.100	0.970	None
L19-076	500	50	0.60	0.30	0.30	380	0.060	0.094	1.350	None
L19-077	500	50	0.60	0.30	0.30	380	0.129	0.094	1.320	None
L19-078	500	50	0.60	0.30	0.30	420	0.076	0.095	1.210	None
L19-079	500	50	0.60	0.30	0.30	420	0.076	0.093	1.220	90s every 410 reps
L19-080	500	50	0.60	0.30	0.30	420	0.076	0.094	1.200	90s every 328 reps
L19-084	500	30	0.60	0.30	0.30	400	0.076	0.091	1.150	90s every 328 reps
L19-085	500	30	0.60	0.30	0.30	400	0.060	0.078	1.190	90s every 328 reps
L19-086	500	30	0.60	0.30	0.30	400	0.030	0.092	1.170	90s every 328 reps
L19-087	250	30	0.45	0.15	0.30	400	0.076	0.099	1.170	90s every 328 reps
L19-097	750	30	0.76	0.46	0.30	400	0.076	0.098	1.180	90s every 328 reps
L19-098	375	30	0.53	0.23	0.30	400	0.076	0.092	1.150	90s every 328 reps

As in Section (1) high-resolution coupled $\omega - 2\theta$ X-ray diffraction scans of the (400) crystal plane are acquired for all samples using a Panalytical X'Pert Pro MRD triple-axis diffractometer and simulated using the Panalytical X'Pert Epitaxy dynamical diffraction modeling program [3]. Typical x-ray diffraction scans for samples L19-075 and L19-087 are shown in Figure 17. Two intensity peaks are observed for sample L19-075: the highest peak at the scan center

corresponds to the GaSb substrate and lattice-matched InAsSb buffer and capping layers, while the second-highest peak indicates the 500 nm thick InAsSbBi layer. Poor agreement between measurement and simulation is realized in most samples. The measured InAsSbBi layer diffraction peaks exhibit low intensity and significant broadening, possible indicators of a high density of dislocations, partial or full strain relaxation, and lateral and vertical composition inhomogeneity due to the metal-modulation digital alloy growth technique. This results in a high degree of uncertainty on the average InAsSbBi lattice constant determined from the x-ray diffraction pattern.

Improved agreement between x-ray measurement and simulation is observed for sample L19-087 grown at 400 °C with InAsSbBi layer thickness of 250 nm. Three intensity peaks are observed, corresponding to the GaSb substrate, InAsSb buffer and cap layers, and the InAsSbBi layer. The intensity and width of the measured InAsSbBi layer x-ray diffraction peak progressively degrades for 400 °C grown samples L19-087 (250 nm thick), L19-098 (375 nm thick), and L19-097 (750 nm thick), suggesting that the x-ray broadening increases with total InAsSbBi layer thickness. This may be due to an increase in compositional & structural inhomogeneity with the metal-modulation digital alloy growth duration.

Assuming completely strained material (i.e. not relaxed), the in-plane and out-of-plane biaxial strains ε_{xx} and ε_{zz} and unstrained lattice constants $a_{InAsSbBi}$ of the InAsSbBi layers are listed in Table 11.

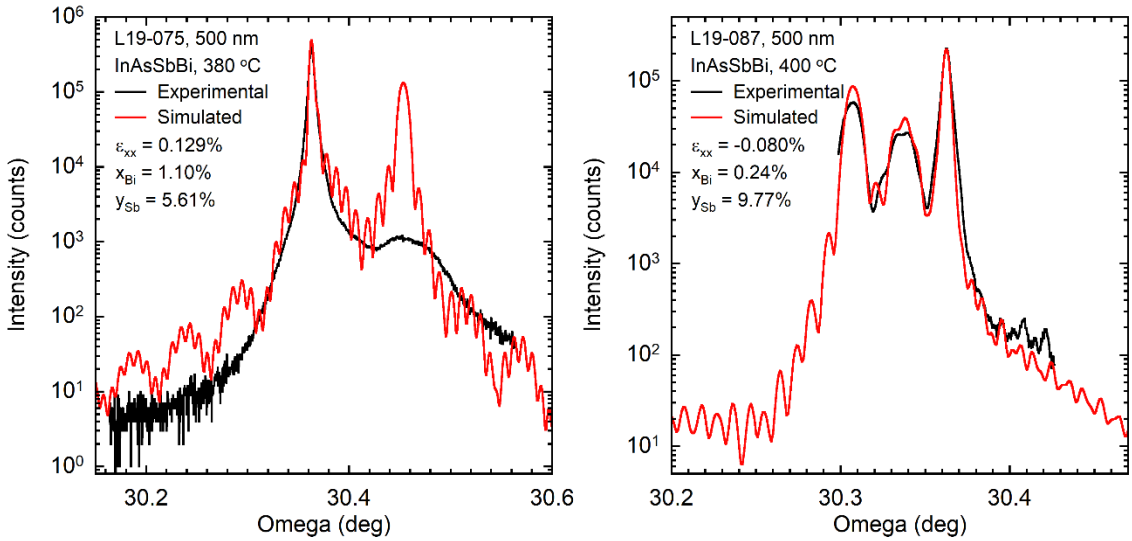

Figure 17. Coupled $\omega - 2\theta$ X-ray diffraction scans of metal-modulation digital alloy InAsSbBi samples L19-075 (left) and L19-087 (right). Average Bi and Sb mole fractions in the InAsSbBi layer are shown

As in Section (1) the InAsSbBi samples are examined using temperature- and excitation-dependent photoluminescence spectroscopy. Selected photoluminescence spectra are shown for the metal-modulation digital alloy InAsSbBi samples L19-075 and L19-087 below in Figure 18. 380 °C grown sample L19-075 exhibits two photoluminescence peaks while 400 °C grown sample L19-087 exhibits a single well-defined photoluminescence peak. Many of the metal-modulation digital alloy samples exhibit two photoluminescence peaks; the peak at lower energy is taken to be due to luminescence from the InAsSbBi layer, as the higher energy peak is nearly constant at about 0.33 eV (3.76 μm) for all samples and is therefore indicative of luminescence from the InAsSb buffer and capping layers. The InAsSbBi layer peak shows evidence of inhomogeneous broadening at the low energy side of the curve. The inhomogeneous broadening is attributable to numerous factors, including lateral and vertical composition modulation, clustering of alloy

elements such as Bi or Sb, localized states associated with the Bi impurity energy level, and partial strain relaxation.

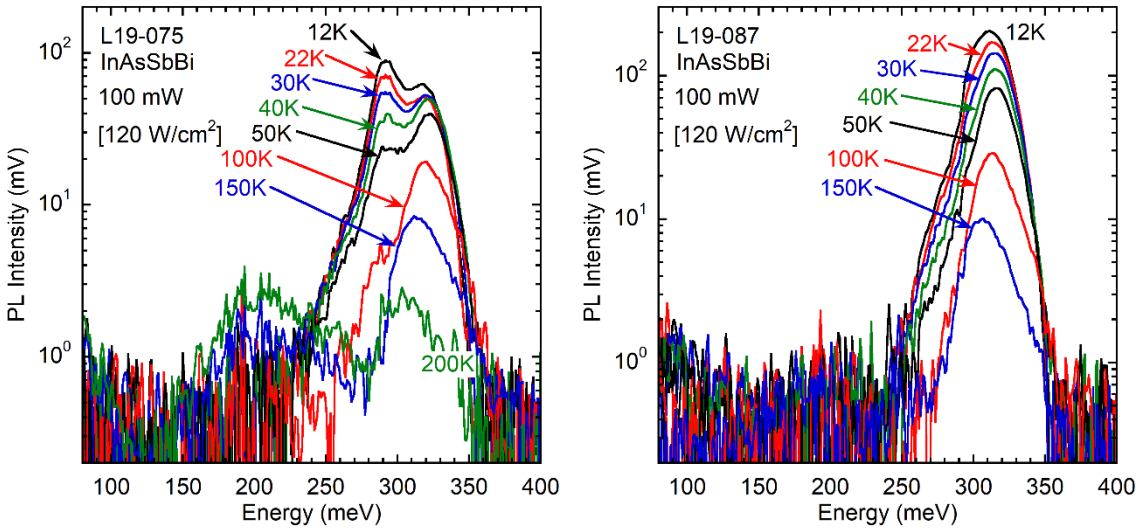

Figure 18. Photoluminescence spectra for metal-modulation digital alloy InAsSbBi samples L19-075 (left) and L19-087 (right) at 100 mW pump laser excitation power (120 W/cm^2)

As in Section (1) the InAsSbBi bandgap energy, E_g, is determined from the first derivative maximum of the photoluminescence energy spectrum. Bandgap energy of 380 °C grown sample L19-075 and 400 °C grown sample L19-087 determined from the first derivative maximum of the photoluminescence spectra is plotted as a function of temperature at a pump laser excitation of 100 mW in Figure 19. The photoluminescence peak energy and the peak energy minus $kT/2$ (which yields the bandgap energy in the simplified case of parabolic band structure) are also shown. The Einstein single oscillator model fit of Eq. (1) is shown as a solid black line. The photoluminescence that appears to originate from localized tail states within the bandgap or from higher energy intensity peaks corresponding to the InAsSb buffer and capping layers is indicated by open symbols and is not included in the fit to the model.

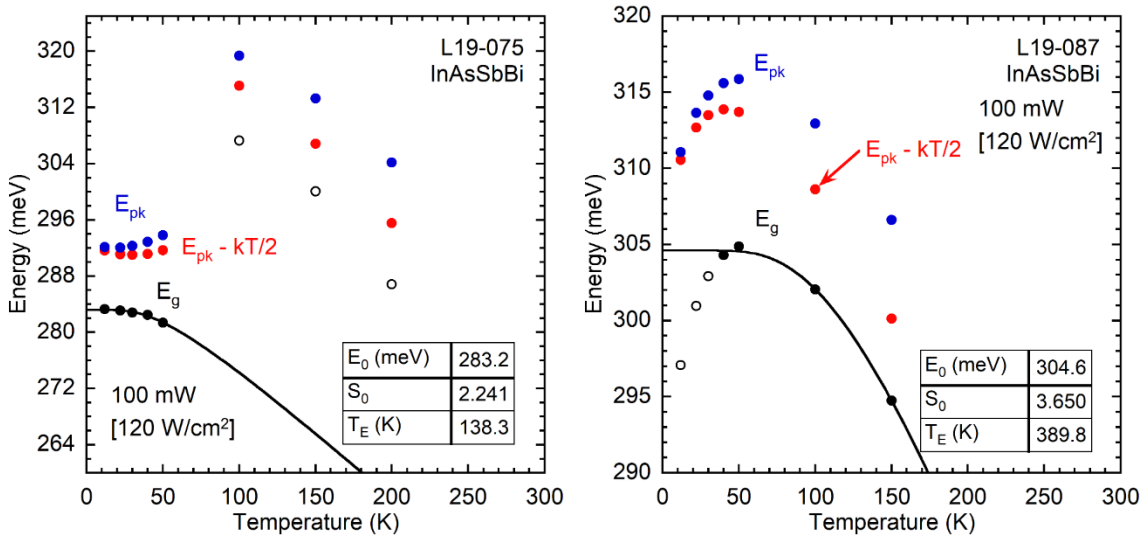

Figure 19. Bandgap energy (black circles), photoluminescence peak energy (blue circles), and peak energy minus $kT/2$ (red circles) as a function of temperature at 100 mW pump laser excitation for metal-modulation digital alloy samples L19-075 (left) and L19-087 (right). Solid black curve is fit of Einstein single oscillator model to bandgap energy data; fit parameters are summarized at lower-left of each figure

The photoluminescence peak energy is seen to be approximately constant at low temperatures for sample L19-075 at about 0.292 eV, however this low-energy intensity peak is extinguished as temperature increases above 50 K. The single photoluminescence peak at temperatures of 100 K and above is thought to be due to the InAsSb buffer and capping layers. In contrast, a single photoluminescence peak is observed for all temperatures for sample L19-087, however the strong blue-shift observed at low temperatures (< 40 K) indicates a comparatively high density of sub-bandgap tail states. These tail states may be attributed to a number of factors including microscopic composition inhomogeneity, localization effects associated with Bi clusters or pairs, or a high density of optically active point defects.

As in Section (1), Vegard's Law for the InAsSbBi lattice constant, Eq. (2), and the InAsSbBi bandgap bowing Eq. (3) are used to determine the average composition of the metal-modulation digital alloy InAsSbBi layers. The results of the x-ray diffraction and photoluminescence spectroscopy measurements of InAsSbBi composition are summarized below in Table 11.

Table 11. Characterization summary for metal-modulation digital alloy InAsSbBi samples measured by x-ray diffraction and photoluminescence spectroscopy. From left: sample number, growth temperature, in-plane biaxial strain ε_{xx}, out-of-plane biaxial strain ε_{xx}, unstrained InAsSbBi lattice constant $a_{InAsSbBi}$, low-temperature bandgap energy $E_{g,InAsSbBi}$, and average group V mole fractions

Sample	Growth temperature (°C)	Biaxial strain (%)		InAsSbBi lattice constant (Å)	Low-temperature bandgap energy (eV)	Mole fractions		
		ε_{xx}	ε_{zz}			Bi	Sb	As
L19-075	380	0.133	-0.144	6.0878	0.3037	0.006	0.060	0.934
L19-076	380	0.129	-0.140	6.0880	0.2832	0.011	0.058	0.931
L19-077	380	0.102	-0.111	6.0897	0.2709	0.014	0.054	0.932
L19-078	380	0.049	-0.053	6.0929	0.3190	0.002	0.080	0.918
L19-079	420	0.048	-0.052	6.0930	0.3206	0.001	0.081	0.918
L19-080	420	0.026	-0.028	6.0943	0.3202	0.001	0.084	0.915
L19-084	420	-0.025	0.028	6.0975	0.3157	0.001	0.090	0.908
L19-085	400	-0.119	0.129	6.1031	0.2441	0.016	0.085	0.899
L19-086	400	-0.075	0.082	6.1005	0.2581	0.014	0.082	0.904
L19-087	400	-0.049	0.053	6.0989	0.3079	0.002	0.093	0.905
L19-097	400	-0.080	0.087	6.1008	0.3046	0.002	0.098	0.900
L19-098	400	0.005	-0.005	6.0956	0.2906	0.008	0.078	0.914

As in Section (1), one-dimensional X-ray diffraction line scans passing through the GaSb substrate and InAsSbBi layer peaks along the ω and 2θ scan directions are acquired from the symmetric (400) and asymmetric (511) reflections using the Panalytical X'Pert Pro MRD triple-axis diffractometer. The resulting line scans are fitted using a Gaussian function in MATLAB R2020a[9] to identify the reciprocal space coordinates of the peaks with an accuracy of ± 0.36 arcseconds. These scans are used to compute the out-of-plane lattice constant while accounting for a tilted layer. Similarly, the in-plane strain and lattice constant are calculated using the ω and 2θ linescans of the (511) planes. [12,13]

The tilt angle between the substrate and layer for samples L19-075 and L19-087 is -12.3 and -4.5 arcseconds, respectively. Both samples are measured in the $< 110 >$ direction. The degree of layer relaxation for both samples is calculated to be 46.6% and 3.8%, respectively. The relaxation measurements indicate that sample L19-075 is relaxed and sample L19-087 is lattice matched to the GaSb substrate. As mentioned before, the relaxation calculations do not account for the maximum tilt between the substrate and layer.

The relaxation and tilt are listed for each sample in Table 12. It is not possible to measure the (511) reflection layer peak for sample L19-087 due to very low diffracted intensity. As a result the layer relaxation cannot be measured.

Many of the metal modulation digital alloy InAsSbBi samples exhibit a broadened low intensity peak. This may be due to several mechanisms including mosaic structure, a range of tilts and strains, or strain relaxation. A mosaic structure is where individual crystalline islands form and have varying orientations independent of each other. Each mosaic structure might have its own tilt with respect to the substrate, causing peak broadening. A mosaic structure may be formed in these samples due to the alternating growth between layers of InBi and AsSb. Bi is known to segregate during growth and during the InBi layer growth, Bi-rich islands may form causing a mosaic-like structure. While many of the XRD peaks were broadened within this sample set, there remain two outliers with sharp, intense peaks: L19-087 and L19-098. Each of these samples also had good agreement with the simulations of the sample structures.

As in Section (1), Nomarski optical microscopy images are acquired to investigate the surface morphology of the metal-modulation digital alloy InAsSbBi samples. All samples except for L19-076, L19-079, L19-087, and L19-098 exhibit surface roughness and droplet-like features. Images at 100x magnification for rough, droplet-covered sample L19-075 and smooth, specular sample L19-087 are shown in Figure 20. In contrast to the random alloy samples examined in Sections (1) and (3), the effective As/In flux ratios are comparatively large at 0.970 – 1.350. In the metal

modulation growth technique comparatively large amounts of Bi are deposited on the surface in the absence of As and Sb flux. Therefore, the surface roughness and presence of surface droplets may be a result of incomplete As-assisted removal of Bi from the surface, despite the apparently large effective As flux.

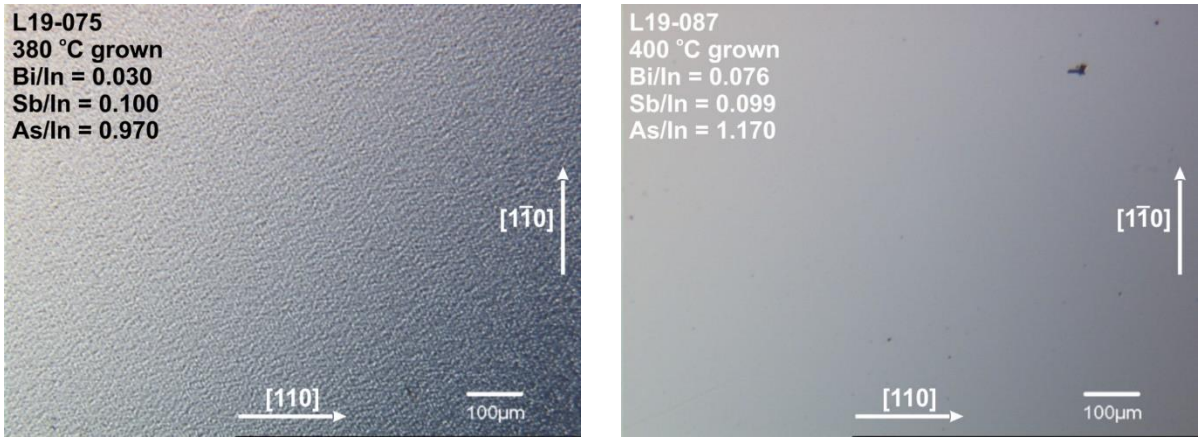

Figure 20. Nomarski optical microscopy images acquired at 100x magnification for metal-modulation digital alloy InAsSbBi samples L19-075 (left) and L19-087 (right)

Table 12. Molecular beam epitaxy growth conditions, strain relaxation, layer tilt, and surface morphology of metal-modulation digital alloy InAsSbBi samples

Sample	Growth temperature (°C)	V/In flux ratios			Relaxation (%)	Tilt (arcsec)	Tilt measurement direction	Nomarski morphology
		Bi/In	Sb/In	As/In				
L19-075	380	0.030	0.100	0.970	46.6	-12.3	< 110 >	Rough
L19-076	380	0.060	0.094	1.350	24.7	-6.4	< 110 >	Rough
L19-077	380	0.129	0.094	1.320	0.28	2.8	< 110 >	Smooth
L19-078	380	0.076	0.095	1.210	16.7	-2.1	< 110 >	Rough
L19-079	420	0.076	0.093	1.220	6.0	-1.5	< 110 >	Rough
L19-080	420	0.076	0.094	1.200	3.1	-2.2	< 110 >	Smooth
L19-084	420	0.076	0.091	1.150	3.5	2.0	< 110 >	Rough
L19-085	400	0.060	0.078	1.190	2.8	4.2	< 110 >	Rough
L19-086	400	0.030	0.092	1.170	17.2	4.5	< 110 >	Rough
L19-087	400	0.076	0.099	1.170	3.8	-4.5	< 110 >	Rough
L19-097	400	0.076	0.098	1.180	N/A	0.4	< 110 >	Smooth
L19-098	400	0.076	0.092	1.150	24.3	-26.5	< 110 >	Rough

4.5 Characterization of 4 μm thick InAsSbBi nBn photodetector heterostructures

A total of three nBn photodetector heterostructures with 4 μm thick InAsSbBi absorber layers grown by molecular beam epitaxy at Air Force Research Laboratory (AFRL) are examined by x-ray diffraction and photoluminescence spectroscopy. The typical growth cross-section is shown in Figure 21. The structure consists of a 350 nm thick InAsSb buffer layer lattice-matched to the GaSb substrate, a 4 μm thick InAsSbBi absorber layer, a 150 nm thick barrier layer composed of either AlAsSb or AlGaAsSb, and a 175 nm thick n-type InAs/InAsSb type-II superlattice contact doped with Si. The InAsSb buffer is grown at 440 °C; the substrate temperature is ramped to the InAsSbBi absorber growth temperature of either 360 °C or 385 °C in the last 50 nm of InAsSb buffer layer growth. The group V fluxes are constant with respect to time for the InAsSbBi layer

resulting in random alloy growth. The Bi/In flux ratio is 0.060, while the Sb/In flux ratios range from 0.085 to 0.095 and As/In flux ratios range from 1.030 to 1.110. The growth is interrupted to ramp the substrate temperature up to 485 °C for growth of the AlAsSb or AlGaAsSb barrier layer. A second growth interrupt is used to ramp the substrate temperature down to 420 °C for growth of the InAs/InAsSb superlattice contact layer. The superlattice contact layer is doped with Si for n-type conductivity. The molecular beam epitaxy growth conditions are summarized in Table 13.

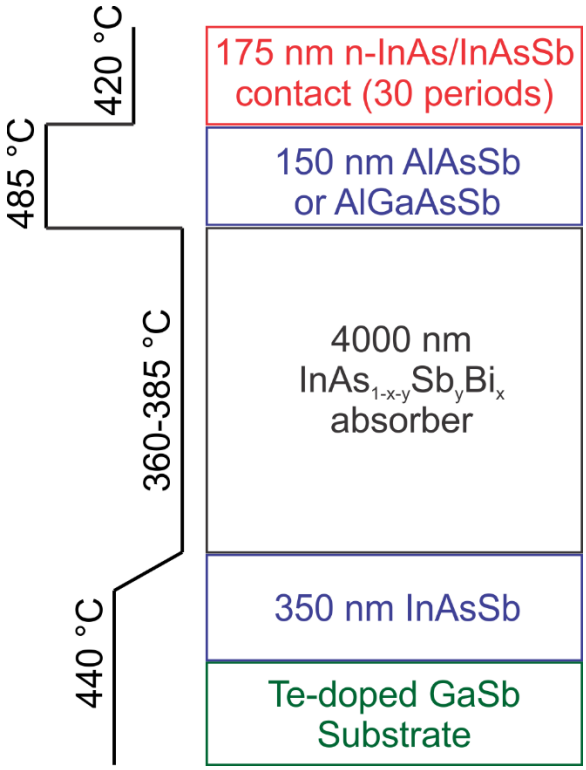

Figure 21. Sample cross-section for nBn photodetector heterostructure samples grown at AFRL

Table 13. Molecular beam growth conditions for nBn photodetector heterostructure samples grown at AFRL

Run number	Barrier layer composition	InAsSbBi Growth temperature (°C)	InAsSbBi layer flux ratios		
			Bi/In	Sb/In	As/In
L19-064	AlAsSb	360	0.060	0.085	1.110
L19-066	AlGaAsSb	360	0.060	0.092	1.030
L19-067	AlGaAsSb	385	0.060	0.095	1.050

As in Section (1), high-resolution coupled $\omega - 2\theta$ X-ray diffraction scans of the (400) crystal plane are acquired for the nBn photodetector heterostructures using a Panalytical X'Pert Pro MRD triple-axis diffractometer and simulated using the Panalytical X'Pert Epitaxy dynamical diffraction modeling program.[3] X-ray diffraction scans are shown for all three nBn photodetector heterostructures in Figure 22. Good agreement between measurement and simulation is observed for 360 °C grown sample L19-064 with an AlAsSb barrier layer. This indicates good interface quality between buffer, absorber, barrier, and contact layers, and nearly lattice-matched material with minimal strain relaxation.

Poor agreement between measurement and simulation is realized in samples L19-066 and L19-067, both grown with AlGaAsSb barriers. This indicates diminished interface quality. The measured InAsSbBi layer diffraction peaks exhibit low intensity and significant broadening, possible indicators of a high density of dislocations, partial or full strain relaxation, and poor interfacial quality between the layer and substrate. This results in a high degree of uncertainty on the average InAsSbBi lattice constant determined from the x-ray diffraction pattern.

In the following analysis, the InAsSbBi layers are assumed to be completely strained to the GaSb substrate; i.e., the layers are not relaxed. The in-plane and out-of-plane biaxial strains ε_{xx} and ε_{zz} and unstrained lattice constants $a_{InAsSbBi}$ of the InAsSbBi layers are listed in Table 14.

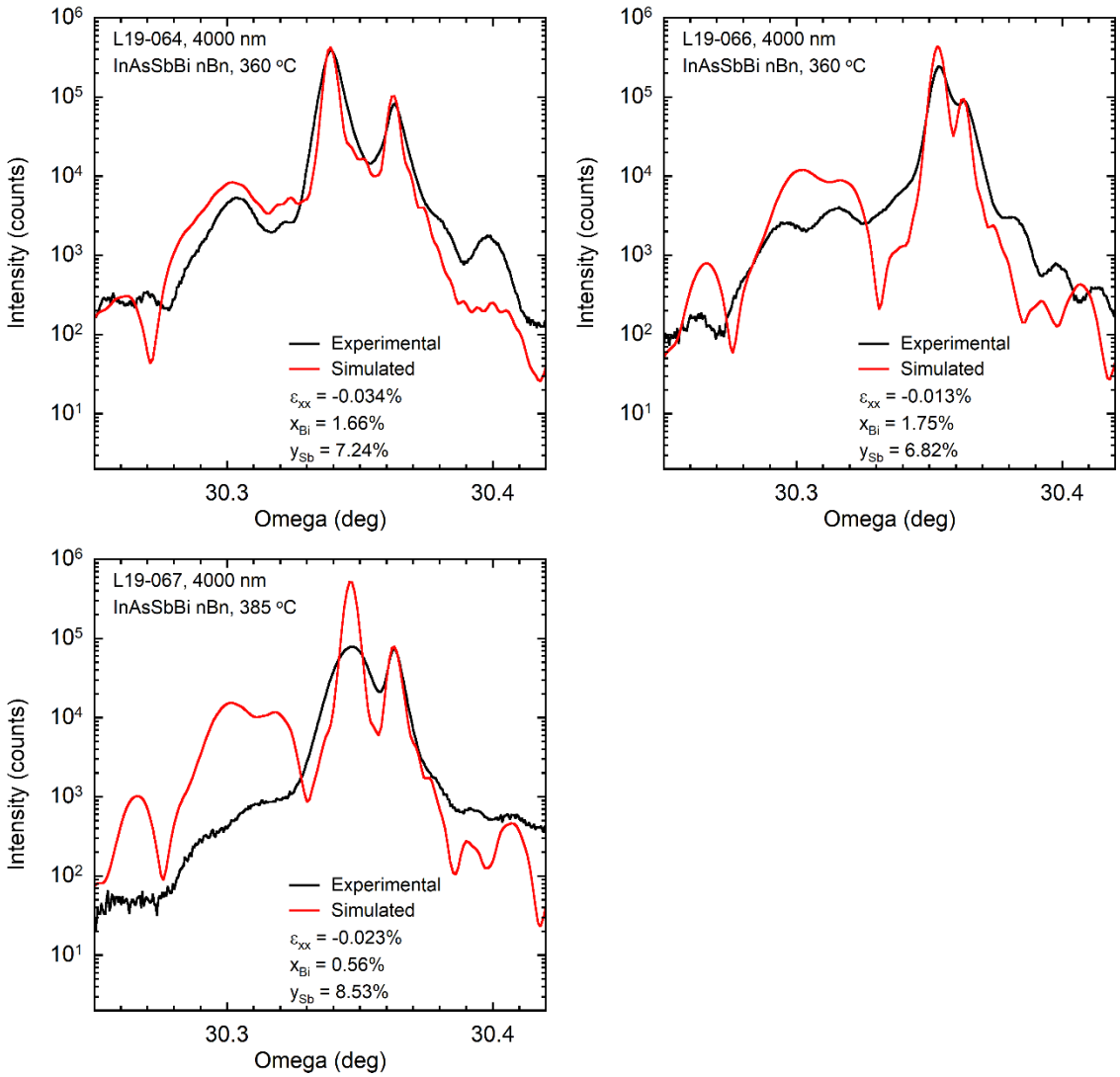

Figure 22. Coupled $\omega - 2\theta$ X-ray diffraction scans of nBn photodetector heterostructure samples L19-064 (upper-left), L19-066 (upper-right), and L19-067 (lower-left). Average Bi and Sb mole fractions in the InAsSbBi layer are shown

As in Section (1) the InAsSbBi samples are examined using temperature- and excitation-dependent photoluminescence spectroscopy. Selected photoluminescence spectra are shown for all three nBn photodetector heterostructures below in Figure 23. The photoluminescence spectra exhibit two peaks; the higher-energy peak near 0.250 – 0.290 eV is attributed to the 4 μm

thick InAsSbBi absorber layer, while the lower energy peak near 0.230 – 0.240 eV is attributed to the InAs/InAsSb superlattice contact layer, which is expected to luminesce near 5 μm (0.248 eV). Photoluminescence intensity is poor for all samples at all temperatures. This is due to several factors, including significant absorption of incident 785 nm pump laser radiation and non-radiative recombination in the relatively highly doped 175 nm thick InAs/InAsSb superlattice contact layer. Additionally, the diminished intensity and strong blue-shift of the InAsSbBi layer peak with temperature may indicate a comparatively high density of point defects due to growth at 360 – 385 °C, clustering of alloy elements such as Bi or Sb, localized states associated with the Bi impurity energy level, and partial strain relaxation.

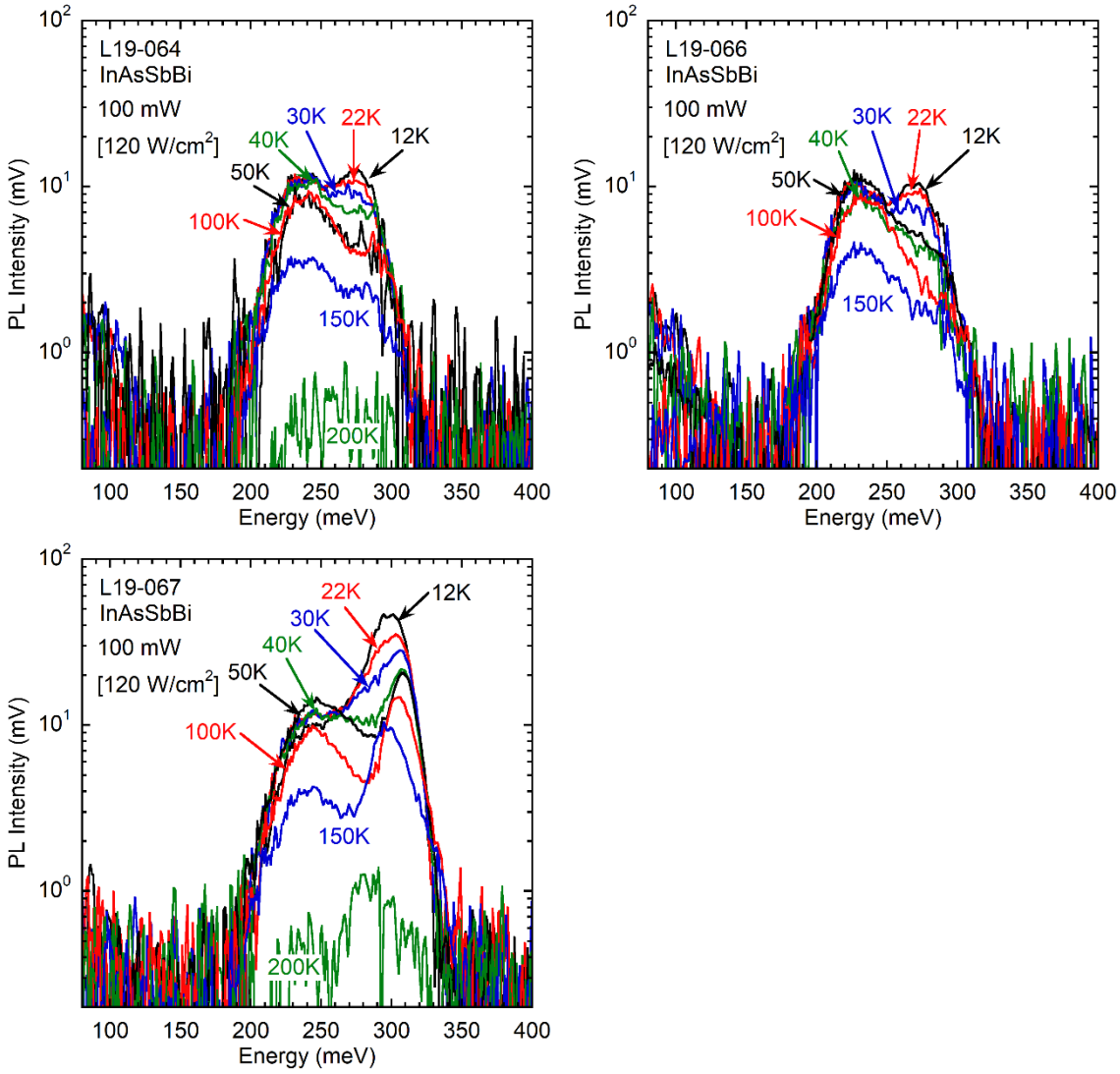

Figure 23. Photoluminescence spectra for nBn photodetector heterostructure samples L19-064 (upper-left), L19-066 (upper-right), and L19-067 (lower-left) at 100 mW pump laser excitation power (120 W/cm²)

As in Section (1) the InAsSbBi bandgap energy, E_g, is determined from the first derivative maximum of the photoluminescence energy spectrum. Bandgap energy of all three nBn photodetector heterostructures determined from the first derivative maximum of the photoluminescence spectra is plotted as a function of temperature at a pump laser excitation of

100 mW in Figure 24. The photoluminescence peak energy and the peak energy minus $kT/2$ (which yields the bandgap energy in the simplified case of parabolic band structure) are also shown. The Einstein single oscillator model fit of Eq. (1) is shown as a solid black line for sample L19-067 only. The photoluminescence that appears to originate from localized tail states within the bandgap or from higher energy intensity peaks corresponding to the InAsSb buffer and capping layers is indicated by open symbols and is not included in the fit to the model. It is not possible to fit Eq. (1) to the bandgap energy data for samples L19-064 and L19-066 due to the disappearance of the InAsSbBi layer peak at temperatures above 30 K. Instead, the average bandgap energy over 12 – 30 K is shown on the figures.

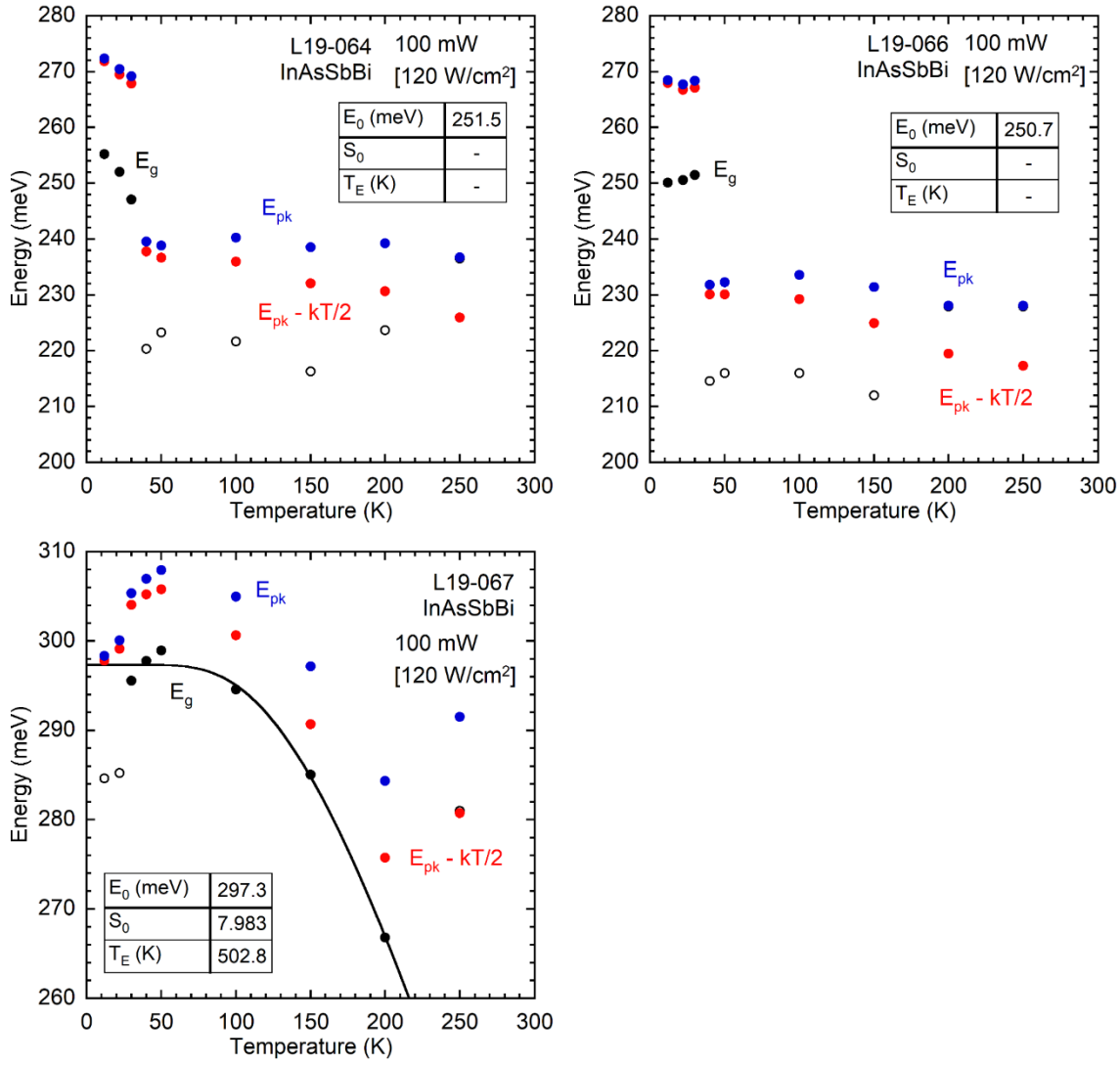

Figure 24. Bandgap energy (black circles), photoluminescence peak energy (blue circles), and peak energy minus $kT/2$ (red circles) as a function of temperature at 100 mW pump laser excitation for nBn photodetector heterostructure samples L19-064 (upper-left), L19-066 (upper-right), and L19-067 (lower-left). Solid black curve is fit of Einstein single oscillator model to bandgap energy data; fit parameters are summarized at lower-left of figure for L19-067. The low-temperature bandgap energies shown for samples L19-064 and L19-066 are the average values over 12 -30 K

The InAsSbBi layer luminescence peak in samples L19-064 and L19-066 disappears at measurement temperatures above 30 K with only luminescence from the InAs/InAsSb superlattice contact layer observed. Sample L19-067 grown at 385 °C exhibits improved photoluminescence with a well-defined InAsSbBi layer peak at temperatures of up to 150 K, however a strong blue-shift in bandgap energy from 12 K to 50 K is also observed. This indicates a comparatively high density of sub-bandgap tail states. These tail states may be attributed to a number of factors including microscopic composition inhomogeneity, localization effects associated with Bi clusters or pairs, or a high density of optically active point defects.

As in Section (1), Vegard's Law for the InAsSbBi lattice constant, Eq. (2), and the InAsSbBi bandgap bowing Eq. (3) are used to determine the average composition of the nBn photodetector heterostructure InAsSbBi layers. The results of the x-ray diffraction and photoluminescence spectroscopy measurements of InAsSbBi composition are summarized below in Table 14.

Table 14. Characterization summary for nBn photodetector heterostructure samples measured by x-ray diffraction and photoluminescence spectroscopy. From left: sample number, growth temperature, in-plane biaxial strain ε_{xx}, out-of-plane biaxial strain ε_{xx}, unstrained InAsSbBi lattice constant $a_{InAsSbBi}$, low-temperature bandgap energy $E_{g,InAsSbBi}$, and average group V mole fractions

Sample	Growth temperature (°C)	Biaxial strain (%)		InAsSbBi lattice constant (Å)	Low-temperature bandgap energy (eV)	Mole fractions		
		ε_{xx}	ε_{zz}			Bi	Sb	As
L19-064	360	-0.034	0.037	6.0980	0.2515	0.018	0.061	0.921
L19-066	360	-0.013	0.014	6.0967	0.2507	0.018	0.066	0.916
L19-067	385	-0.023	0.025	6.0973	0.2973	0.005	0.087	0.908

As in Section (1), one-dimensional X-ray diffraction line scans passing through the GaSb substrate and InAsSbBi layer peaks along the ω and 2θ scan directions are acquired from the symmetric (400) and asymmetric (511) reflections using the Panalytical X'Pert Pro MRD triple-axis diffractometer. The resulting line scans are fitted using a Gaussian function in MATLAB R2020a[9] to identify the reciprocal space coordinates of the peaks with an accuracy of ± 0.36 arcseconds. These scans are used to compute the out-of-plane lattice constant while accounting for a tilted layer. Similarly, the in-plane strain and lattice constant are calculated using the ω and 2θlinescans of the (511) planes.

The relaxation and tilt are listed for each sample in Table 15. The tilt angle between the substrate and layer for samples L19-064, L19-066, and L19-067 is -1.4, 0.4, and -0.4 arcseconds, respectively. Each sample is measured in the $< 110 >$ direction. The degree of layer relaxation for each sample is calculated to be 19.5%, 73.1%, and 23.3%, respectively. The relaxation measurements indicate that each sample is relaxed with respect to the substrate. As mentioned before, the relaxation calculations do not account for the maximum tilt between the substrate and layer. Each of the diffraction peaks in this sample set were relatively sharp and intense. However, each sample exhibited a high level of relaxation within the InAsSbBi layer. Partial relaxation is likely to occur unless the layer is very closely lattice matched to the GaSb substrate. The relaxation and relatively high intensity are both due to the large InAsSbBi layer thickness of 4 µm.

As in Section (1), Nomarski optical microscopy images are acquired to investigate the surface morphology of the nBn photodetector heterostructure InAsSbBi samples. Sample L19-064 grown at 360 °C is optically smooth and specular while samples L19-066 and L19-067 exhibit surface roughness and droplet-like features. Images at 100x magnification for all three nBn photodetector heterostructure samples are shown in Figure 25. The smooth sample L19-064 is grown with the highest As/In flux ratio, 1.110, while the other two rough samples L19-066 and L19-067 are grown with lower As/In flux ratios of 1.030 and 1.050, respectively. The higher As/In flux ratio used during growth of smooth sample L19-064 may contribute to increased rates of As-assisted desorption of excess unincorporated Bi, suppressing the formation of Bi-rich droplet features.

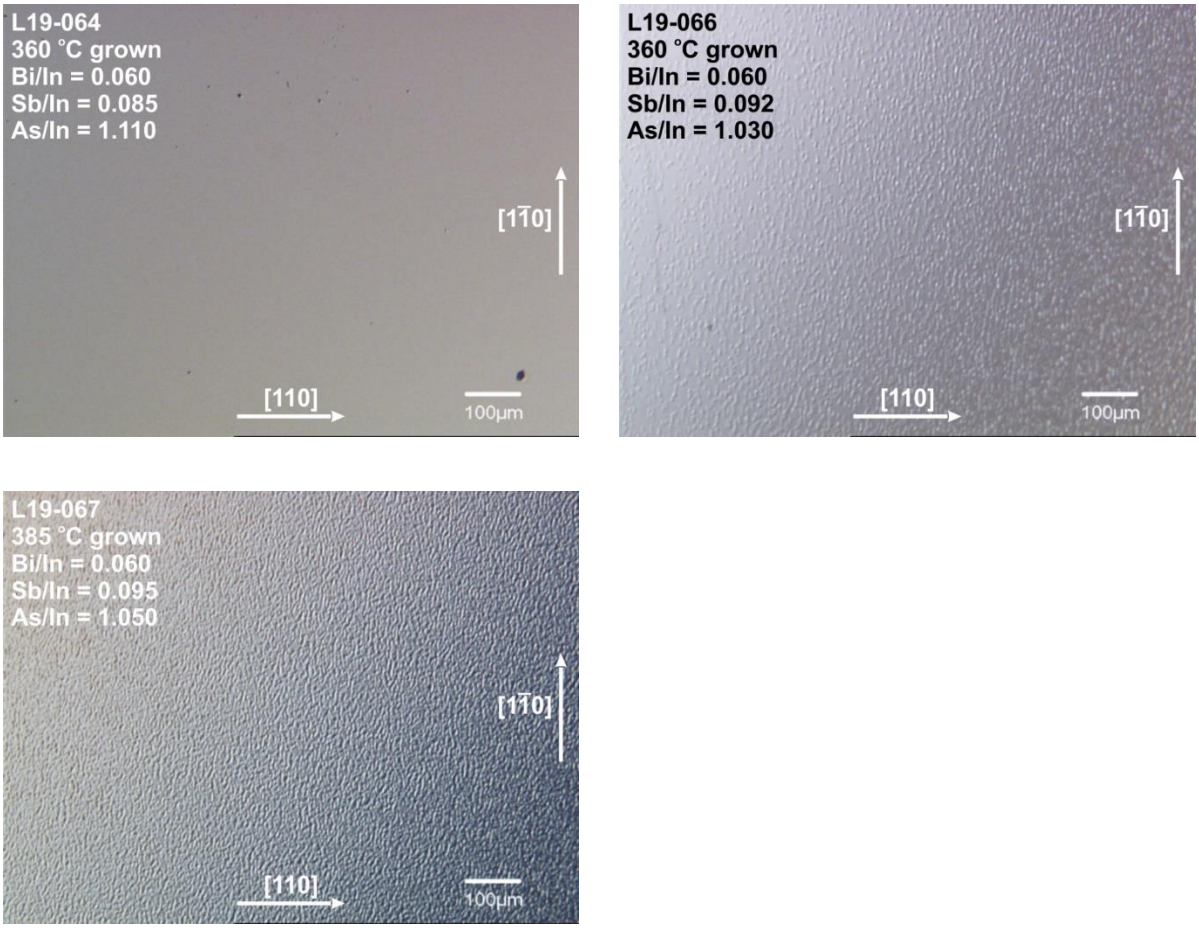

Figure 25. Nomarski optical microscopy images acquired at 100x magnification for nBn photodetector heterostructure samples L19-064 (upper-left), L19-066 (upper-right), and L19-067 (lower-left)

Table 15. Molecular beam epitaxy growth conditions, strain relaxation, layer tilt, and surface morphology of metal-modulation digital alloy InAsSbBi samples

Sample	Growth temperature (°C)	V/In flux ratios			Relaxation (%)	Tilt (arcsec)	Tilt measurement direction	Nomarski morphology
		Bi/In	Sb/In	As/In				
L19-064	360	0.060	0.085	1.110	19.5	-1.4	< 110 >	Smooth
L19-066	360	0.060	0.092	1.030	73.1	0.4	< 110 >	Rough
L19-067	385	0.060	0.095	1.050	23.3	-0.4	< 110 >	Rough

4.6 Photoluminescence study of radiation-damaged InAsSbBi

Several InAsSb and InAsSbBi samples are irradiated, and photoluminescence spectroscopy measurements were used to compare the optical quality of the material before and after the radiation treatment. The samples were grown at Arizona State University using solid source molecular beam epitaxy on ¼ 50mm (100)-oriented p-type GaSb substrates. The sample cross sections are illustrated in Figure 26. The growths consist of a 500 nm GaSb buffer, a 10 nm InAs/10 nm AlSb partially strain-balanced barrier, an active region containing InAs, InAsSb, or InAsSbBi bulk layers, and a 10 nm AlSb/10 nm InAs barrier and cap layer. The GaSb buffer layer is grown at 500 °C except for the last 70 nm, where the substrate temperature is reduced by 70–100 °C in preparation for the growth of the bulk layer. The growth conditions are summarized in Table 16.

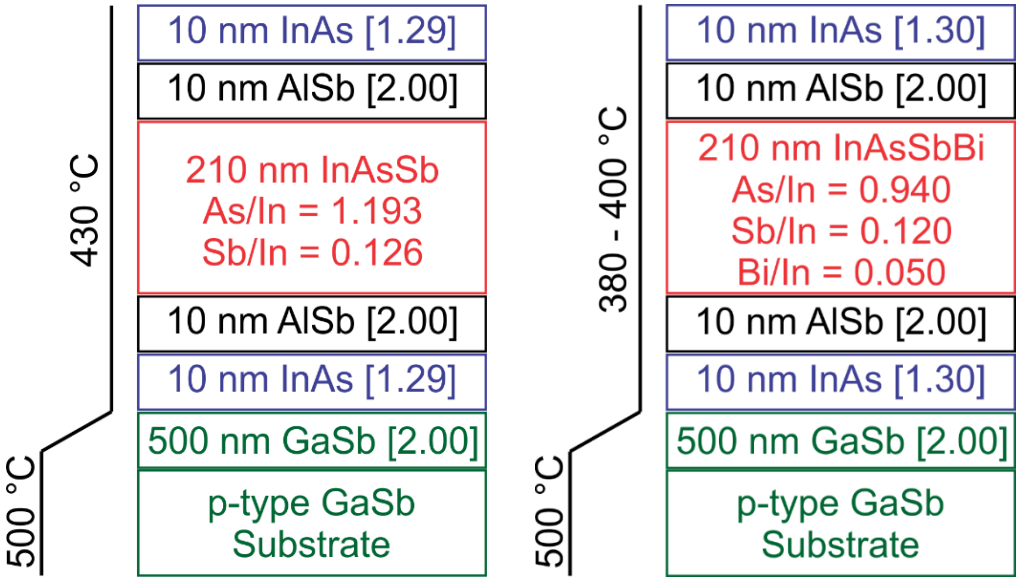

Figure 26. Growth cross-sections for InAsSb (left) and InAsSbBi (right) samples studied by photoluminescence spectroscopy. Molecular beam epitaxy growth conditions, including V/In flux ratios and growth temperatures, are listed on the figure. Quantities in square brackets indicate V/In flux ratios for the binary layers

Table 16. Molecular beam epitaxy growth conditions for samples studied by photoluminescence spectroscopy. Low temperature bandgap energy from photoluminescence measurements carried out prior to irradiation are listed

Run number	Sample description	Growth temperature (°C)	Flux Ratios			Low temperature bandgap E_0 (meV)
			Bi/In	Sb/In	As/In	
B2496	210 nm InAsSb on GaSb	430	0.00	0.126	1.193	322.4
B2511	210 nm InAsSbBi on GaSb	400	0.05	0.120	0.940	292.3
B2512	210 nm InAsSbBi on GaSb	380	0.05	0.120	0.940	234.5

The InAsSbBi samples are irradiated using a 63 MeV proton beam at the UC Davis Crocker Nuclear Laboratory. 63 MeV particle energy is used because it is sufficiently high that a uniform damage profile is expected over the thicknesses of typical devices. The samples are dosed at 100 krad, equivalent to a fluence of 7.5×10^{11} protons per cm^2.

The samples are examined using temperature- and excitation-dependent photoluminescence spectroscopy both before and after radiation treatment. The samples are mounted in a closed-loop He-refrigerated cryostat and optically pumped using a modulated 785 nm laser diode. The measurements are performed at various temperatures ranging from 12 to 295 K using an average pump power of 100mW (120 W/cm^2 incident intensity). The photoluminescence is collected using a Nicolet Magna-IR 760 Fourier Transform infrared spectrometer with an InSb detector with a cutoff wavelength of 5.5 µm. The pump laser is modulated at 50 kHz, and the detector signal is fed through a phase-locked loop amplifier for improved signal-to-noise. The system optical throughput is measured and corrected using the spectrum from a Mikron M305 black body source at 800 °C. Photoluminescence spectra from before and after radiation treatment are shown at each measurement temperature below in Figures 27 – 29.

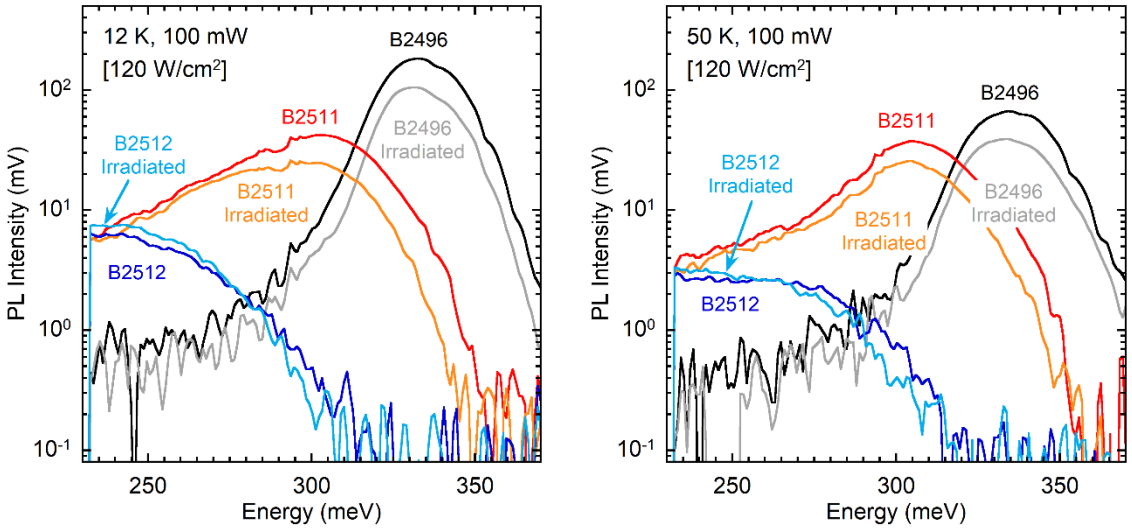

Figure 27. Photoluminescence spectra for InAsSb (black/grey) and InAsSbBi (red/orange and blue/cyan) samples at 100 mW pump laser power at (left) 12 K and (right) 50 K. The black, red, and blue curves indicate photoluminescence from samples prior to irradiation, while the grey, orange, and cyan curves indicate post-radiation treatment photoluminescence

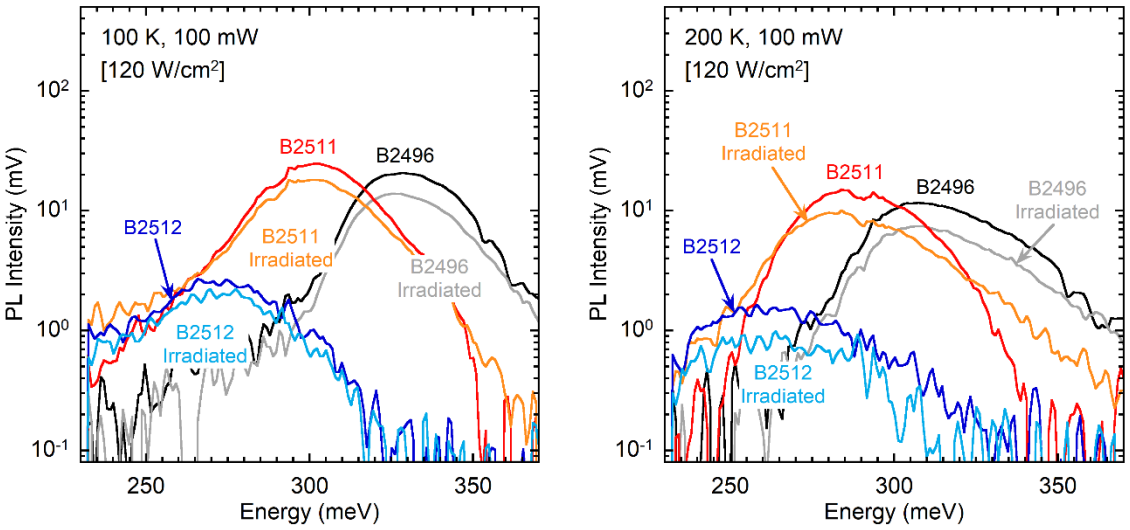

Figure 28. Photoluminescence spectra for InAsSb (black/grey) and InAsSbBi (red/orange and blue/cyan) samples at 100 mW pump laser power at (left) 100 K and (right) 200 K. The black, red, and blue curves indicate photoluminescence from samples prior to irradiation, while the grey, orange, and cyan curves indicate post-radiation treatment photoluminescence

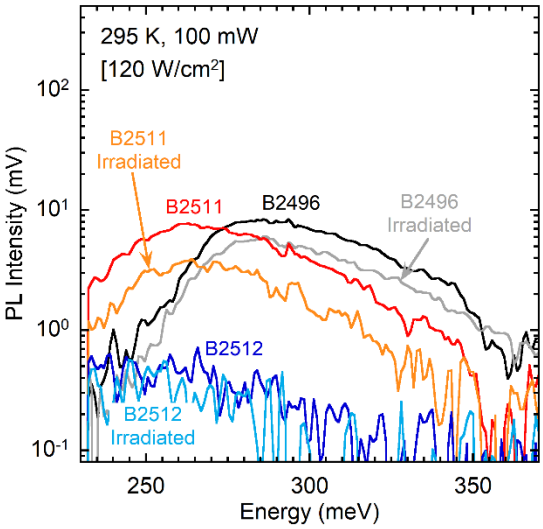

Figure 29. Photoluminescence spectra for InAsSb (black/grey) and InAsSbBi (red/orange and blue/cyan) samples at 100 mW pump laser power at 295 K. The black, red, and blue curves indicate photoluminescence from samples prior to irradiation, while the grey, orange, and cyan curves indicate post-radiation treatment photoluminescence

Integrated photoluminescence, defined as the integral of the photoluminescence intensity over the photon energy measurement range, is a useful figure of merit for comparing optical quality. Reduction in internal quantum efficiency due to radiation damage is indicated by a corresponding reduction in the integrated photoluminescence as shown in Figure 30.

Integrated photoluminescence generally decreases with temperature due to an increase in radiative lifetime and simultaneous increase in nonradiative lifetime. This trend is preserved in the samples both before and after irradiation, with no significant change in the temperature dependence observed.

Radiation treatment reduces the integrated photoluminescence by an average of 20-40% as shown on the right in Figure 30. The ratio of the integrated photoluminescence after radiation treatment to the integrated photoluminescence before irradiation is marginally higher for the InAsSbBi samples by about 5-10% relative to the InAsSb sample. This result indicates that incorporation of Bi may increase radiation hardness for III-V alloys, however further studies involving a greater number of samples with higher Bi content are needed to draw a formal conclusion.

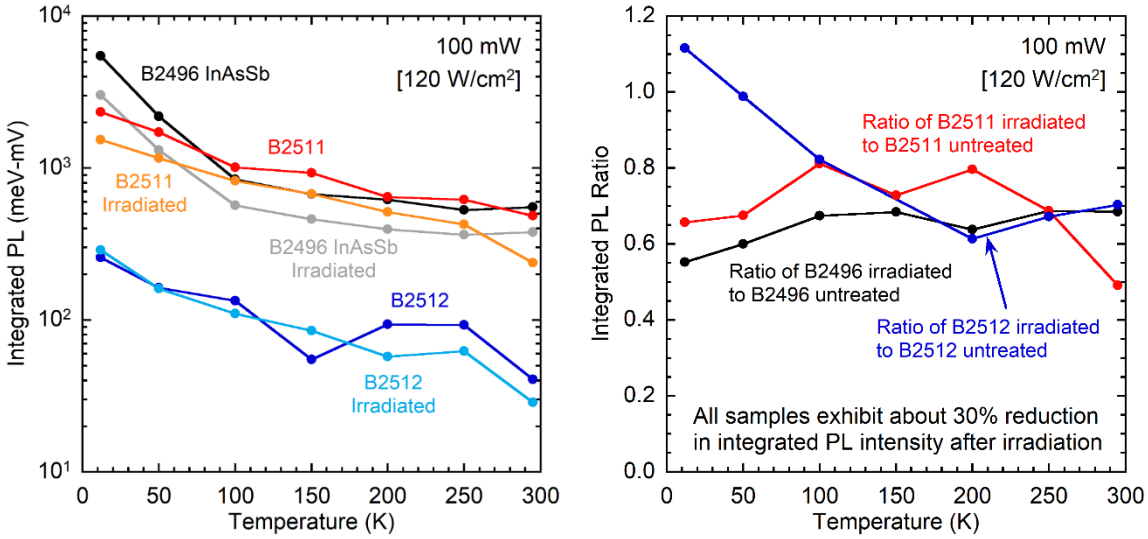

Figure 30. Left: Integrated photoluminescence versus temperature for InAsSb (black/grey) and InAsSbBi (red/orange and blue/cyan) samples at 100 mW pump laser power. Right: ratio of integrated photoluminescence after irradiation to integrated photoluminescence before irradiation for InAsSb (black) and InAsSbBi (red and blue) versus temperature. The black, red, and blue curves indicate integrated photoluminescence from samples prior to irradiation, while the grey, orange, and cyan curves indicate post-radiation treatment photoluminescence

4.7 Characterization of 210 nm thick bulk InAsSbBi samples

This work examines three $InAs_{1-x-y}Sb_yBi_x$ samples grown by solid-source molecular beam epitaxy at a rate of 15 nm/min on GaSb (100), (100) 1° to (011) and (100) 4° to (111) offcut-oriented substrates. The sample cross-section is shown in Figure 31 and consists of a 500 nm GaSb buffer, a 10 nm InAs/10 nm AlSb partially strain balanced barrier, the InAsSbBi active region, and a terminating 10 nm AlSb/10 nm InAs barrier/cap layer. The GaSb buffer layer is grown at 500 °C except for the last 70 nm where the substrate temperature is reduced by 70 to 100 °C in preparation for the growth of the InAsSbBi active layer. The InAsSbBi layers are grown at temperature of 400 °C, using V/In flux ratios 0.105 and 0.120 for Sb/In, 0.050 for Bi/In, and 0.911 for As/In. The temperatures and V/In flux ratios used during growth, and the in-plane biaxial strain of the InAsSbBi bulk layers are provided for each sample in Table 17.

Table 17. InAsSbBi sample name, substrate orientation, growth temperature, V/In flux ratios, average mole fractions, in-plane strain, and presence of surface droplet features

Sample	Substrate orientation	Growth temperature	V/In flux ratios			Mole fraction (%)			Strain (%)	Surface droplets
			Bi/In	Sb/In	As/In	Bi	Sb	As		
A	(100)	400 °C	0.050	0.120	0.911	0.78	9.52	89.70	-0.111	Yes
B	(100) 1° to (011)	400 °C	0.050	0.120	0.911	0.74	10.07	89.19	-0.146	Yes
C	(100) 4° to (111)	400 °C	0.050	0.105	0.911	0.65	8.83	90.52	-0.052	Yes

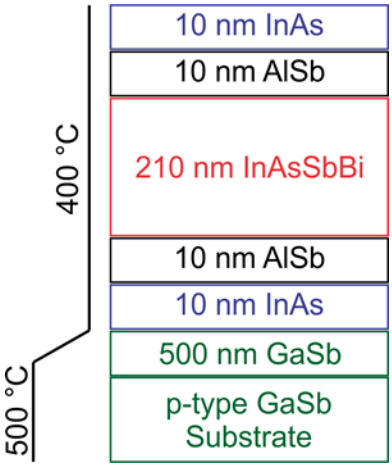

Figure 31. Nominal growth cross-section of the bulk InAsSbBi samples examined by x-ray diffraction

A schematic of the surfaces of the on-axis and two offcut substrates are shown in Figure 32. The offcut result in terraces and step edges. Terraces run along the $[0\bar{1}1]$ direction on (100) offcut surfaces. In both cases, monolayer step edges form along the $[011]$ and $[0\bar{1}1]$ directions, which results in a smooth terrace edge.

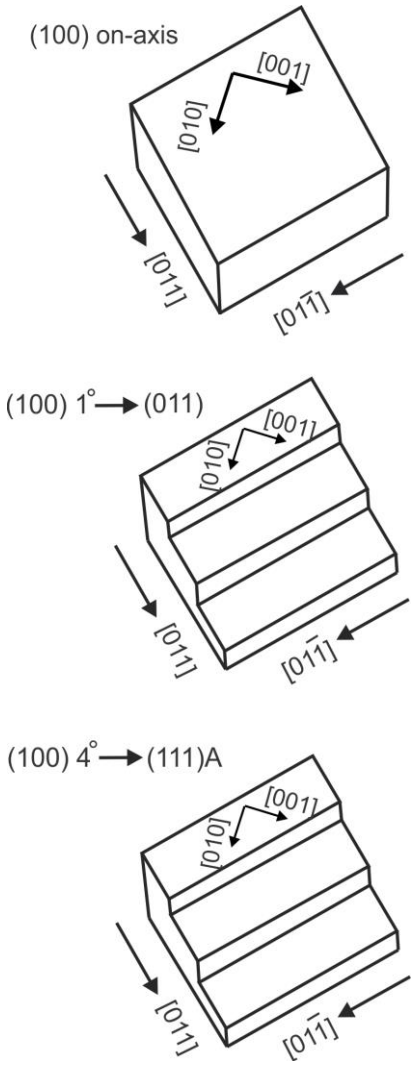

Figure 32. Surfaces of flat on-axis and terraced offcut substrates. The terrace edges are smooth and in the $[0\bar{1}1]$ direction on (100) surfaces offcut to (011) and to (111)A

The surface morphology of the samples is examined using Nomarski optical microscopy and atomic force microscopy (AFM). The Nomarski images are acquired using an Olympus MX50 optical microscope with Nomarski prism, analyzer, and polarizer components. The AFM images are acquired using a Brucker multimode 8 microscope with a lateral scan range of 100 microns and a vertical scan range of 5.5 microns. The structure and composition of InAsSbBi films are investigated using high-resolution X-ray diffraction (XRD) and transmission electron microscopy (TEM). The XRD measurements are performed using a PANalytical X'Pert Pro materials Research X-ray diffractometer with an instrumental resolution of 12 arcsec and Cu $K\alpha_1$ radiation with a 1.54 Å wavelength. Simulations of coupled diffraction scans are carried out using the PANalytical X'Pert Epitaxy[3] dynamical diffraction modeling software. Cross sectional TEM samples are prepared in the $[0\bar{1}1]$ projections using wedge polishing followed by Ar-ion milling at liquid nitrogen temperature. TEM imaging is carried out using a Philips CM 200 microscope operating at 200 kV, with an interpretable resolution of 2.5 Å. Scanning TEM imaging is carried out using an aberration corrected JEOL ARM 200F operated at an acceleration voltage of 200 kV, with a spatial resolution of 0.8 Å.

Nomarski optical microscopy images of the surface of the three InAsSbBi samples are shown in Figure 33. The images are 200 μm wide by 150 μm high and the significant growth conditions are shown for each. Surface droplet features are observed on all samples. These features have respective diameters and densities of 3 μm and 5×10^5 cm^{-2} in sample A, 5 μm and 7×10^5 cm^{-2} in sample B, and 3 μm, and 8×10^5 cm^{-2} in sample C. Additionally, sample B (Figure 33b) with step edge density 5.7×10^5 cm^{-1} exhibits anisotropic surface droplet features, indicating preferential diffusion of the Bi atoms along the step edges in the $[0\bar{1}1]$ direction.

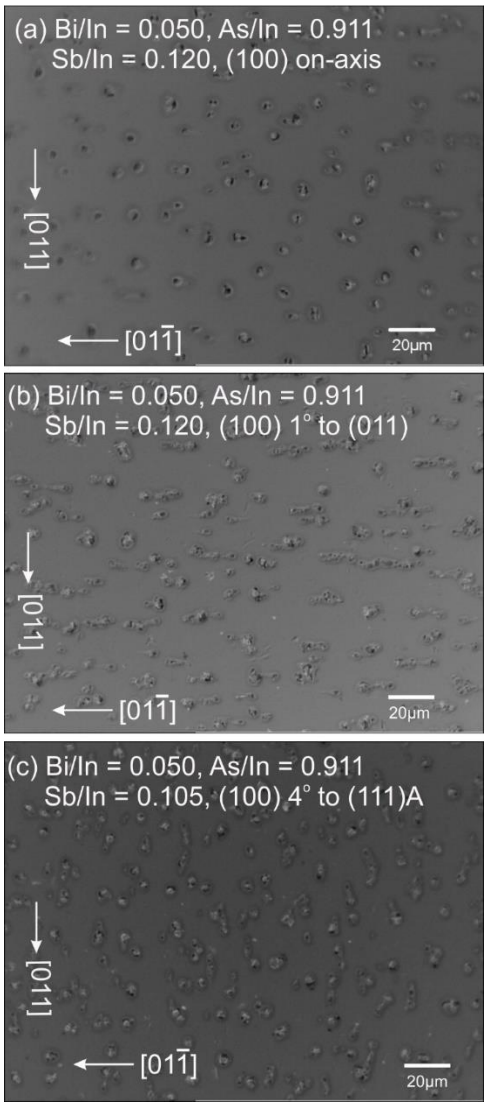

Figure 33. Nomarski optical measurements of the surface morphology of bulk InAsSbBi samples A through C, shown in (a) through (c) respectively. Image dimensions are 200 μm by 150 μm. The Bi/In, As/In, and Sb/In flux ratios and substrate orientation are shown for each sample

Atomic force microscopy images of the surface morphology of InAsSbBi samples A through C, labeled (a) through (c), are shown in Figure 34. The images are 100 μm by 100 μm on the left with a zoomed in 5 μm by 5 μm measurement on the right. The root mean square (RMS) roughness over each area imaged is shown in Table 18. With droplets over 200 nm high, the surfaces have a RMS roughness around 40 nm on the 100 μm length scale. The surface between the large droplet features is relatively smooth with a RMS roughness that is less than 1 nm on the

5 μm length scale. The difference in RMS roughness values attributed to minimization of surface energy by introduction of uniform array of monoatomic
growth steps. [14]

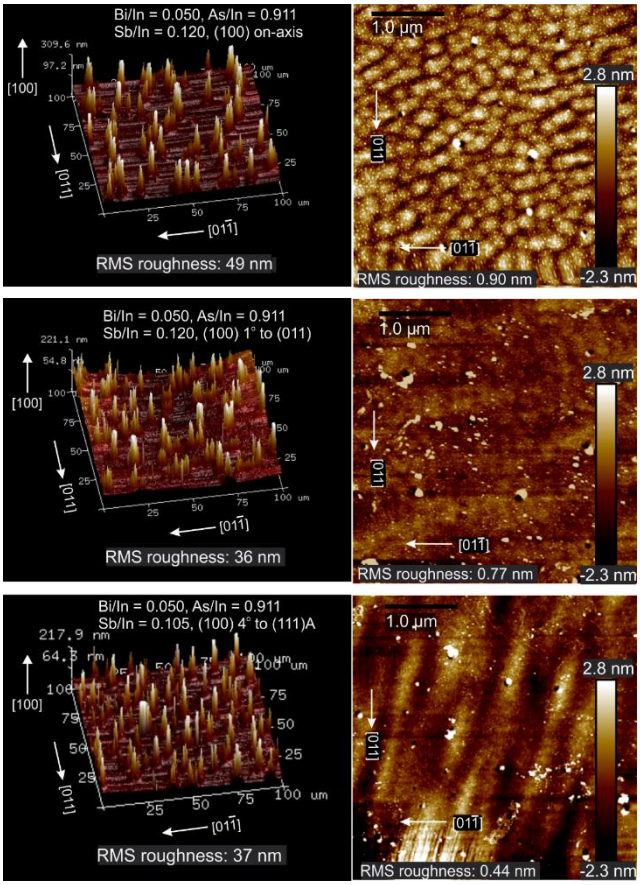

Figure 34. Atomic force microscopy images of the surface morphology of bulk InAsSbBi samples A through C, shown in (a) through (c) respectively. Images dimensions are 100 μm by 100 μm on the left and 5 μm by 5 μm on the right. The root mean square (RMS) roughness range from 45 nm to 37 nm over 100 μm length scale and 0.90 nm to 0.44 nm over 5 μm length scale. The Bi/In, As/In, and Sb/In flux ratios and substrate orientation are shown for each sample

Table 18. Root mean square (RMS) surface roughness of samples A through C from AFM measurements over surface areas of 100 μm by 100 μm, 5 μm by 5 μm, and 1 μm by 1 μm. The growth information is provided for the InAsSbBi layer of each sample

Sample	Substrate orientation	Flux ratios			RMS roughness (nm)		
		Bi/In	Sb/In	As/In	100 μm by100 μm	5 μm by 5 μm	1 μm by 1 μm
A	(100) on-axis	0.050	0.120	0.911	49	0.90	0.46
B	(100) 1° to (011)	0.050	0.120	0.911	36	0.77	0.52
C	(100) 4° to (111)A	0.050	0.105	0.911	37	0.44	0.41

The droplet sizes and densities, an estimation of the fraction of the surface covered by droplets, and the average droplet volume per unit area are reported in Table 19. The droplet volume relative to the InAsSbBi layer volume is respectively 5%, 10%, and 7% for samples A through C. Sample B with preferential diffusion along the $[0\bar{1}1]$ direction has the largest surface droplet coverage.

Table 19. Surface droplet density, diameter, height, fraction of surface area covered, and aggregate volume per unit area for each measurement method for samples A, B, and C

Sample	A, (100) on-axis		B, (100) 1° to (011)		C, (100) 4° to (111)A	
Method	Nomarski	AFM	Nomarski	AFM	Nomarski	AFM
Density (cm^{-2})	5×10^5	5×10^5	7×10^5	7×10^5	8×10^5	8×10^5
Diameter (μm)	3	3	5	5	3	3
Average Height (nm)	-	310	-	220	-	220
Surface Coverage (%)	4	4	10	10	6	6
Volume/unit area (nm)	-	11	-	22	-	14

The overall microstructure of the InAsSbBi layers is examined using cross-sectional TEM. Low magnification bright-field TEM micrographs from the three InAsSbBi samples are presented in Figure 35. The results indicate that the 210 nm thick InAsSbBi layers are pseudomorphic with no visible defects over large lateral distances. Furthermore, contrast modulation due to inhomogeneous composition[5] with a modulation period of approximately 30 nm is observed in samples A and C shown in Figs. 35a, and 35c respectively. Lateral composition modulation is not observed in sample B (see Figure 35b), which has a relatively lower density of step edges.

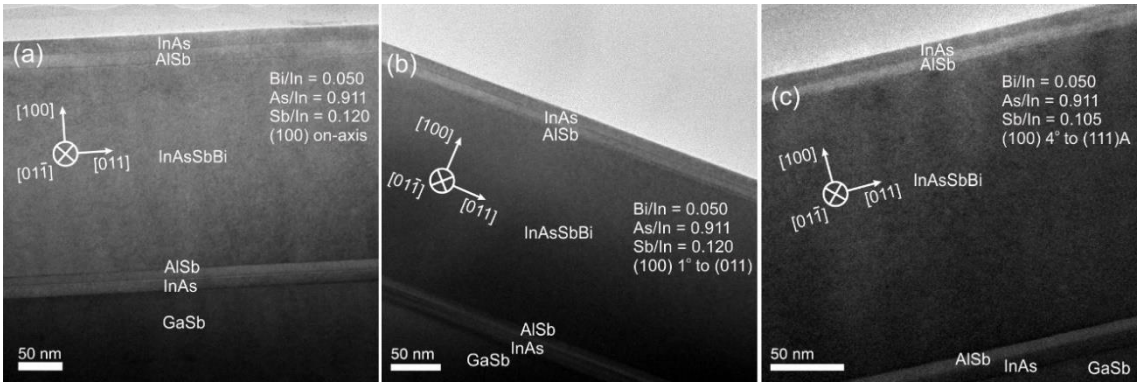

Figure 35. Bright field cross-section TEM images in the $[0\bar{1}1]$ projection showing the overall microstructure of InAsSbBi samples A through C, in (a) through (c) respectively. Contrast modulation with period of approximately 30 nm is observed perpendicular to the growth plane in (a), and (c). The Bi/In, As/In, and Sb/In flux ratios and substrate orientation are shown

The Bi mole fraction is estimated from chemically the sensitive (200) dark-field images using a method developed by Bithell and Stobbs.[85] In this method, according to kinematical approximation, the intensity of the dark field reflection, $I_{200,InAsSbBi}$, is proportional to the square of the specimen thickness d and the square of the structure factor for the (200) reflection that satisfies the selection rule $h + k + l = 4n + 2$. By considering the ratio of intensity scattered by InAsSbBi into the (200) reflection to that scattered by AlSb at same specimen thickness, the constant of proportionality and the specimen thickness are eliminated, and the ratio of the intensities is given as, [11]

$$\frac{I_{200,InAsSbBi}}{I_{200,AlSb}} = \frac{[f_{In} - (1-x-y)f_{As} - yf_{Sb} - xf_{Bi}]^2}{[f_{Al} - f_{Sb}]^2} \quad . \tag{4}$$

Using this relationship, the Bi mole fraction is expressed in terms of the scattering factors, the Sb mole fraction, and the ratio of the intensities, with

$$x = \frac{f_{As} - f_{In} + (f_{Sb} - f_{As})y + (f_{Al} - f_{Sb})\sqrt{\frac{I_{200,InAsSbBi}}{I_{200,AlSb}}}}{f_{As} - f_{Bi}}. \quad (5)$$

The atomic scattering factors f_{Al}, f_{In}, f_{As}, f_{Sb}, and f_{Bi} for Al, In, As, Sb, and Bi used in the analysis are determined from Doyle and Turner[86] by linearly interpolating their tabulated values to the relevant scattering angle parameter $s = 1/a_{\perp}$, where $a_{\perp}$ is the out-of-plane lattice constant of the strained InAsSbBi layer. The Sb mole fraction $y(x, a_{InAsSbBi})$ is a function of the Bi mole fraction x and the unstrained InAsSbBi lattice constant $a_{InAsSbBi}$ provided by the XRD analysis in the next section.

The lateral Bi mole-fraction profiles obtained from chemically sensitive (200) dark field images are shown in Figure 36. The specimen cross sections examined are approximately 80 nm thick. The Bi mole fraction varies laterally from 0.73% to 0.83% with an average of 0.78% in sample A, from 0.72% to 0.75% with an average of 0.74% in sample B, and from 0.63% to 0.69% with an average of 0.65% in sample C. The average InAsSbBi mole fractions are also reported in the TEM + XRD section of Table 20. In comparison, the combined photoluminescence (PL) and XRD measurements specify an average Bi value [1] of 0.71% for sample A, 0.81% for sample B, and 0.58% for sample C, which are reported in the PL + XRD section of the table. The Bi incorporation coefficient defined as the ratio of the Bi mole fraction to the incident Bi/In flux ratio is also provided. The results indicate that the presence of step edges on the offcut surfaces does not significantly impact Bi incorporation.

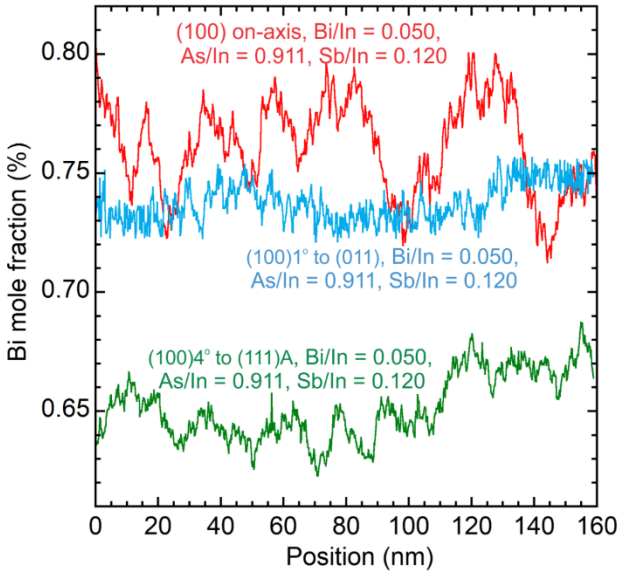

Figure 36. Lateral Bi mole fraction profiles obtained from chemically sensitive 200 dark-field images of InAsSbBi samples A through C, with the significant growth conditions shown for each

Table 20. InAsSbBi substrate orientation, average group-V mole fractions (%), and Bi incorporation coefficient (%) determined from X-ray diffraction (XRD) and dark field transmission electron microscopy (TEM + XRD) or photoluminescence[4] (PL + XRD)

Sample	Substrate orientation	TEM + XRD				PL + XRD			
		Bi	Sb	As	Bi incorporation coefficient (%)	Bi	Sb	As	Bi incorporation coefficient (%)
A	(100)	0.78	9.52	89.70	15.6	0.71	9.61	89.68	14.2
B	(100) 1° to (011)	0.74	10.07	89.19	14.8	0.81	10.05	89.14	16.2
C	(100) 4° to (111)A	0.65	8.83	90.52	13.0	0.58	8.92	90.50	11.6

High angle annular dark field scanning transmission electron micrographs from samples A, B, and C are shown in Figs. 37a, b, and c respectively. These images, commonly referred to as Z-contrast images, [87] provide mass thickness contrast that is primarily dependent on atomic number, and are particularly well suited for detecting heavier elements such as Bi. Intensity line profiles across the areas marked in the micrographs are shown below the images. Lateral quasi-periodic composition variation with a period of approximately 30 nm is observed in samples A and C, while lateral composition modulation is not observed in sample B. These results are consistent with the bright field TEM micrographs in Figure 35 and the lateral Bi mole fraction profiles in Figure 36.

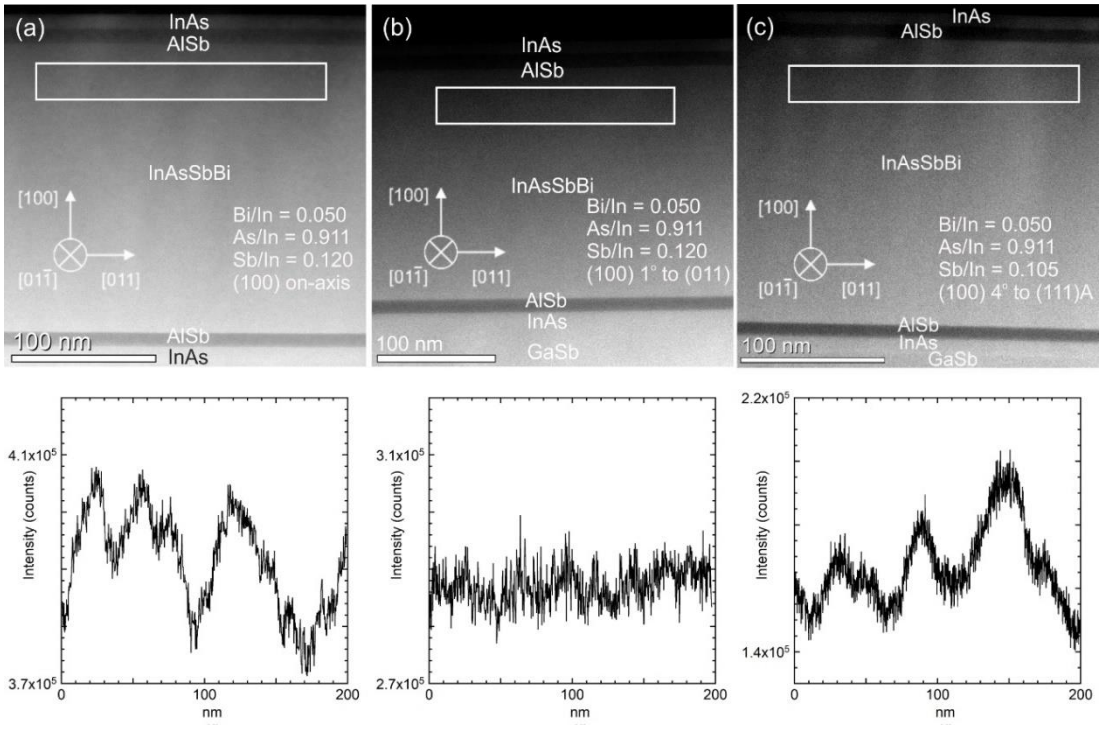

Figure 37. High angle annular dark field scanning TEM images in the $[0\bar{1}1]$ projection showing the overall microstructure of InAsSbBi samples A, B, and C, in (a), (b), and (c) respectively. Line scans of the image intensity from the regions marked by the rectangles parallel to the layer interface are shown. Contrast modulations perpendicular to the growth direction in (a) and (c) show composition inhomogeneity with a modulation period of approximately 30 nm. The Bi/In, As/In, and Sb/In flux ratios and substrate orientation are shown for all samples

Atomic resolution aberration-corrected high-angle-annular dark-field scanning transmission electron micrographs from samples A, B, and C are shown in Figure 38a, b, and c respectively. Images in the $[01\bar{1}]$ projection shows the top and bottom interfaces of InAsSbBi samples. Individual atomic columns are observed. The micrographs indicate that the InAsSbBi layers have high quality interfaces with no misfit dislocations. Atomic steps are observed on the surface of the offcut samples B and C.

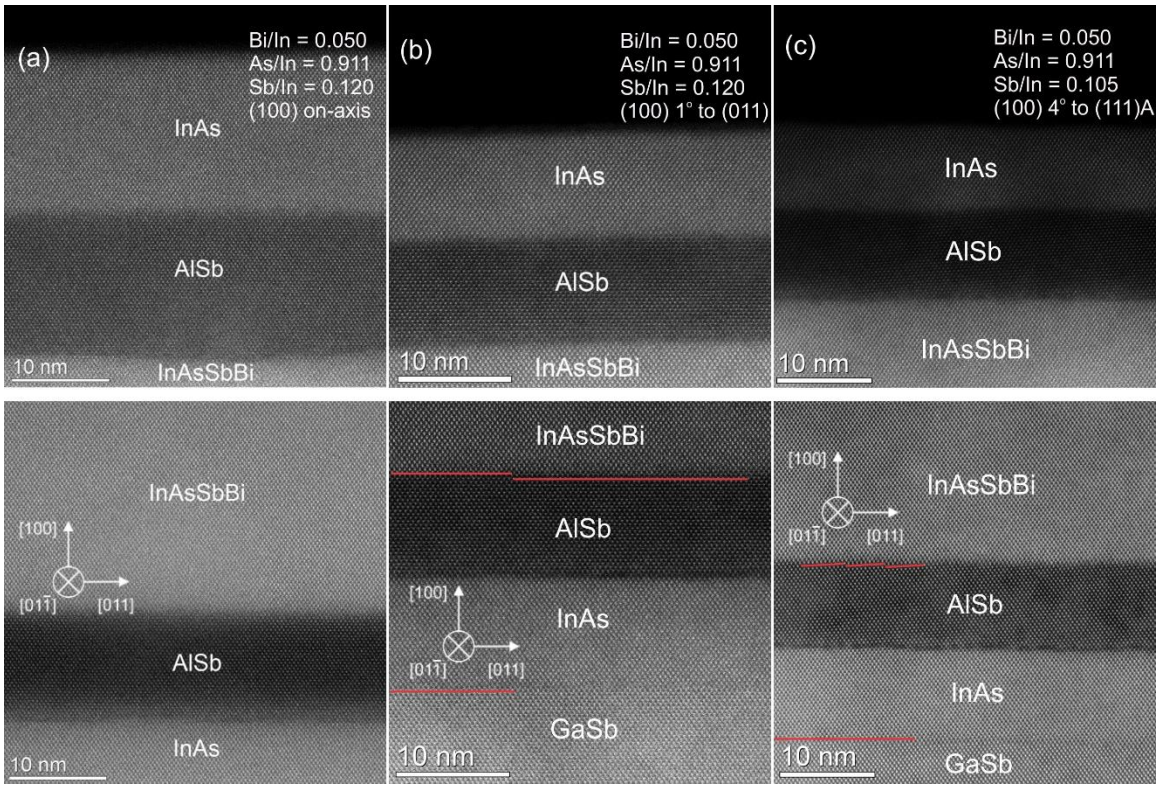

Figure 38. Atomic resolution high-angle-annular dark-field scanning TEM images in the $[01\bar{1}]$ projection showing the top and bottom interfaces of InAsSbBi samples A through C, in (a) through (c) respectively. Atomic steps are observed and marked in (b) and (c). The Bi/In, As/In, and Sb/In flux ratios and substrate orientation are shown

4.8 Crystallographic tilt in coherently strained InAsSbBi grown on offcut GaSb substrates

The X-ray diffraction measurements are performed using a PANalytical X'Pert Pro MRD X-ray diffractometer with an instrumental resolution of 12 arcsec and Cu $K\alpha_1$ radiation with a 1.540598 Å wavelength. Coupled scans of the (400) planes are measured for each sample in both the $[\bar{0}11]$ and $[0\bar{1}1]$ directions and used in a dynamical simulation to extract the Bragg angles of each InAsSbBi layer.

The coupled scans must cross through the center of each peak to accurately simulate the layer thicknesses and compositions. Coupled scans rotate the sample and the detector such that the angle of incidence is equal to the angle of diffraction. Tilt between the substrate and epilayer lattice planes creates an offset that the coupled scan must account for to cross through the center of each diffraction peak. An offset scan introduces a constant offset between the angles of incidence and diffraction.

If a layer contains tilted lattice planes and a coupled scan is measured in the direction of the tilt, the diffracted peak position of the layer will be offset by an amount equal to the tilt angle. However, coupled scans measured orthogonal to the tilt direction do not contain an offset since there is no tilt in that direction. Therefore, scans measured orthogonal to the tilt direction do not shift the layer peak positions. It is known that crystallographic tilt occurs in the offcut direction, therefore scans measured in the offcut direction also correspond to the epilayer tilt direction. The impact of tilt on coupled scan direction for the 4° offcut sample is shown in Figure 39.

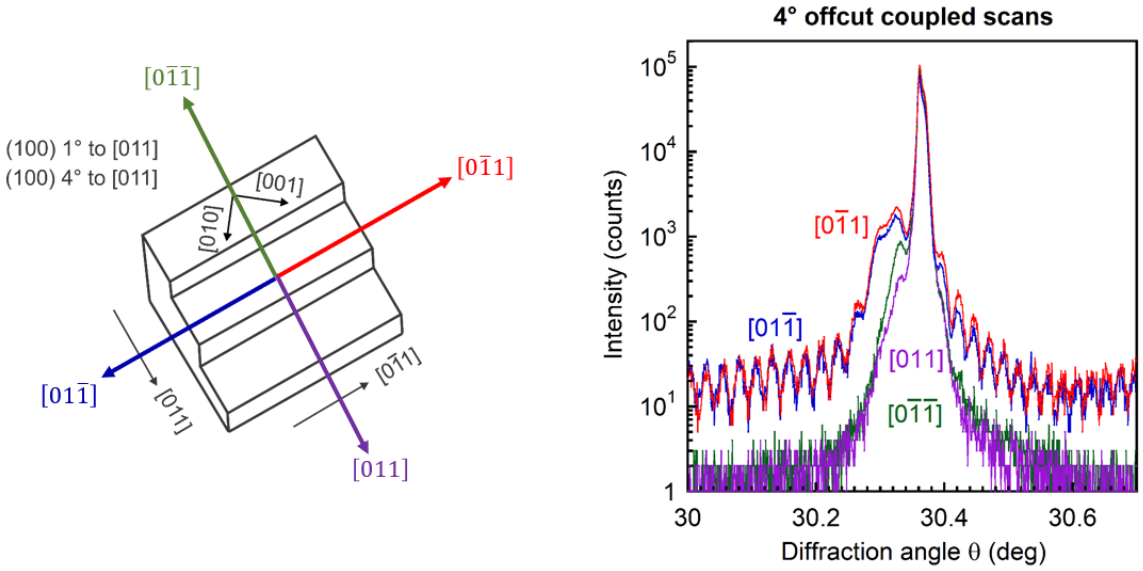

Figure 39. (Left) Coupled scans measured in the offcut direction corresponding to the $[0\bar{1}\bar{1}]$ (green) and $[011]$ (purple) directions and orthogonal to the offcut direction corresponding to the $[0\bar{1}1]$ (red) and $[01\bar{1}]$ (blue) directions along the offcut surface. (Right) Coupled scan intensity as a function of the diffraction angle θ for the 4° offcut InAsSbBi sample measured in the offcut direction in the $[0\bar{1}\bar{1}]$ (green) and $[011]$ (purple) directions, and orthogonal to the offcut direction in the $[0\bar{1}1]$ (red) and $[01\bar{1}]$ (blue) directions

Coupled scans are measured in the offcut direction corresponding to the $[0\bar{1}\bar{1}]$ (green) and $[011]$ (purple) directions and orthogonal to the offcut direction corresponding to the $[0\bar{1}1]$ (red) and $[01\bar{1}]$ (blue) directions along the offcut surface. The coupled scan intensity as a function of the diffraction angle θ is plotted for each scan direction. The coupled scans measured in the direction of the tilt, $[0\bar{1}\bar{1}]$ and $[011]$, do not cross through the center of the layer peak which results in a loss of epilayer diffraction intensity and the absence of measured Pendellösung fringes. However, the scans measured orthogonal to the tilt direction, $[0\bar{1}1]$ and $[01\bar{1}]$, cross through the center of the layer peaks which can be seen by an increase in layer peak intensity and the restoration of Pendellösung fringes.

Since the scans measured in the $[0\bar{1}1]$ and $[01\bar{1}]$ directions cross through both the substrate and epilayer diffraction peaks, they are dynamically simulated using the PANalytical X'Pert Epitaxy software and are shown in Figure 40.

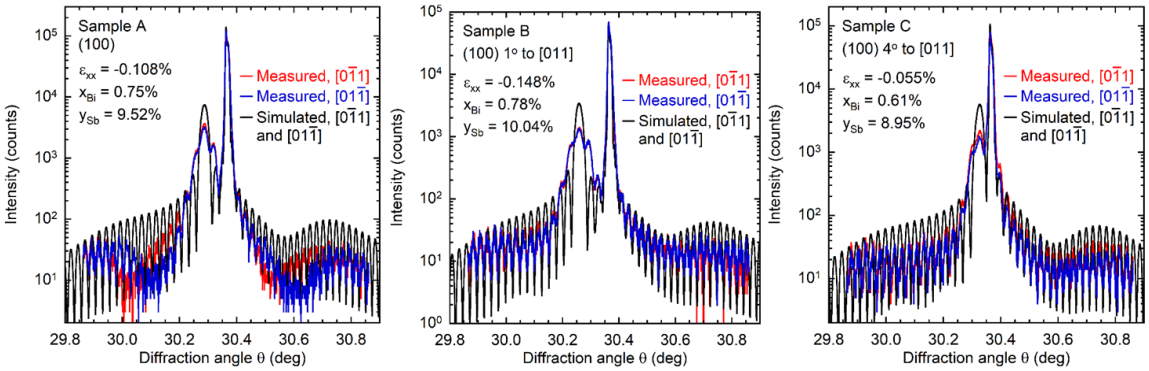

Figure 40. Coupled scans as a function of diffraction angle θ measured in the $[\bar{0}11]$ (red) and $[0\bar{1}\bar{1}]$ (blue) directions for the on-axis (left), 1° offcut (center), and 4° offcut (right) samples. Dynamical simulations (black) of each coupled scan are shown. Each sample contains a GaSb substrate peak, a compressive InAsSbBi layer peak, and a tensile GaAsSb buffer peak. The in-plane strain and the Bi and Sb mole fractions are shown for each sample

The diffraction pattern of each sample contains a GaSb substrate peak, a compressive InAsSbBi layer peak, and a tensile GaAsSb buffer peak. The Sb and Bi mole fractions are altered in the simulation until the simulated coupled scan matches the measured angular separation between the GaSb substrate and InAsSbBi layer. Further, the thicknesses of the InAsSbBi layer and AlSb barrier layers are adjusted so that the simulated period of the Pendellösung fringes matches that of the measured scans. The InAs layer thicknesses are found self-consistently assuming a constant In deposition rate used throughout the growth.

In the dynamical simulations, the InAsSbBi layer is assumed to be pseudomorphic as the lattice mismatch is sufficiently small that the critical thickness significantly exceeds that of the InAsSbBi layer in all samples. The results extracted from the simulations are summarized in Table 21.

Table 21. InAsSbBi layer properties extracted from the best visual fit of the dynamical simulations to the coupled scans measured orthogonal to the tilt direction

Sample	On-axis	1° offcut	4° offcut
Simulated thickness (nm)	194	189	190
Out-of-plane distortion $\varepsilon_{\perp}$ (%)	0.2264	0.3092	0.1148
In-plane biaxial strain ε_{xx} (%)	– 0.1083	– 0.1479	– 0.0550
Lattice constant $a_{InAsSbBi}$ (Å)	6.1025	6.1049	6.0993

The simulated thickness of each sample is approximately 20 nm less than the target 210 nm thick InAsSbBi layer. Each sample is compressively strained resulting in a unit cell that is distorted in the out-of-plane direction. Due to inadvertent incorporation of approximately 0.17% As in the GaSb buffer, a slight tensile peak is measured near the GaSb substrate peak. The As that incorporated unintentionally in the GaSb buffer is due to the As background pressure in the growth chamber.

The discrepancies between the simulated and measured InAsSbBi layer peak intensities can be attributed to peak broadening from the presence of surface droplets. The droplets on the surface of the sample are thought to scatter incident X-rays at various angles that broadens the layer peak as a result. The broadening necessarily lowers the intensity of the layer peak and is not observed in bulk InAsSbBi sample without the presence of surface droplets. Previous studies show that incorporation of Bi can result in Bi segregation on the growth surface leading to the formation of surface features such as droplets.

The lattice planes of the strained epilayers grown on the offcut substrates tilt relative to the plane of substrate offcut as a means to accommodate the in-surface biaxial-strain and the out-of-surface distortion. Under tensile strain the epilayers tilt in the $[011]$ direction of the offcut and under compressive strain the epilayers tilt in the opposite $[0\bar{1}\bar{1}]$ direction of the offcut. Since the maximum tilt angle occurs in the direction of the offcut, angle area scans are acquired in the $[011]$ and $[0\bar{1}\bar{1}]$ directions as a means to directly determine the tilt angle between the substrate and epilayer (400) planes.

The desired angle area maps are generated by acquiring a series of offset coupled scans with the offset angle $\theta - \omega$ varied such that both the substrate peak (zero offset) and the titled epilayer peaks are measured. With respect to (400) substrate reflection, ω is the angle of incidence (source position) and θ is the angle of diffraction (detector position). The series of scans form angle area contour maps of the diffracted peak positions, which are shown in Figure 41. The results are shown for all three samples with on-axis (left), 1° offcut (center), and 4° offcut (right) substrates, with the $[011]$ direction scans in the upper row and the $[0\bar{1}\bar{1}]$ direction scans in the lower row.

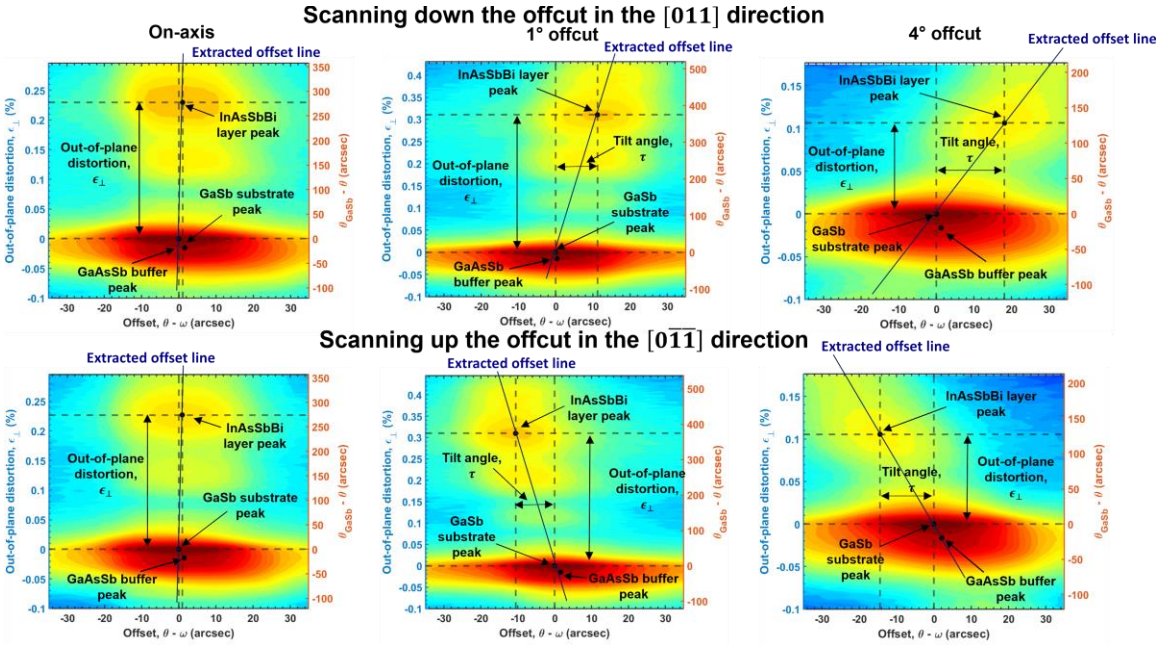

Figure 41. Angle area maps of the (400) planes of on-axis (left), 1° offcut (center), and 4° offcut (right) samples extracted in the and $[011]$ (top) and $[0\bar{1}\bar{1}]$ (bottom) directions. The left y-axis plots the out-of-plane distortion and the right y-axis plots the θ separation from the substrate. The substrate, buffer, and layer peak positions are plotted as black dots and found using a two-dimensional Gaussian fitting routine. The amount of tilt and out-of-plane distortion of the InAsSbBi layer is shown as double-sided arrows

The left-hand vertical axis shows the out of plane distortion of the epilayers, the right-hand vertical axis shows the epilayer diffraction angle relative to that of the substrate, and the horizontal axis shows the offset angle relative to the zero offset substrate peak. Since the scans are measured parallel to the tilt direction, the tilt angles of the epilayers are given by the offset angle. The substrate, buffer, and layer peak positions are shown as black dots and are determined using the two-dimensional Gaussian fitting routine described below. The amount of out-of-plane tilt and out-of-plane distortion is shown as double-sided arrows. The line labeled “extracted offset line” goes though the substrate and the InAsSbBi layer peaks, and is extracted from the two dimensional data set as a means to examine and simulate the variable offset coupled scan that is of interest. The X-ray diffractometer is not capable of directly measuring such a scan; therefore, it must be extracted from the set of measured offset scans.

The X'Pert Epitaxy software does not provide a capability to simulate angle area scans. Therefore, a fitting routine must be utilized to determine the diffracted peak positions. To accurately determine the peak locations in the angle area maps, the following two-dimensional elliptical Gaussian fitting function is fit to the data.

$$f(\theta-\omega,\theta,\vec{a}) = a_0 e^{-\frac{1}{2}\left(\frac{(((\theta-\omega)-a_1)\cos a_5-(\theta-a_2)\sin a_5)^2}{a_3^2}+\frac{(((\theta-\omega)-a_1)\sin a_5+(\theta-a_2)\cos a_5)^2}{a_4^2}\right)} + a_6 \quad (6)$$

where $\theta-\omega$ is the offset angle, θ is the diffraction angle, and the $\vec{a}$ vector contains the fitting parameters. a_1 is the offset angle peak location, a_2 is the diffraction angle peak location, a_3 is the standard deviation of the peak in the offset angle direction, a_4 is the standard deviation of the peak in the diffraction angle direction, a_5 is the rotation angle of the elliptical Gaussian, and a_6 is a constant intensity offset. An elliptical Gaussian is chosen because it allows the peaks' major axes to be rotated. This can be seen in 41 as the major axes of the layer peak contours for the offcut samples appear to be rotated relative to the substrate.

The Gaussian fitting routine is consistently implemented for each sample and locates the peak positions in-between measured data points. The results from the three peak locating methods and the Gaussian surface fit of the substrate and buffer in three-dimensions for the 4° offcut sample are shown in Figure 42.

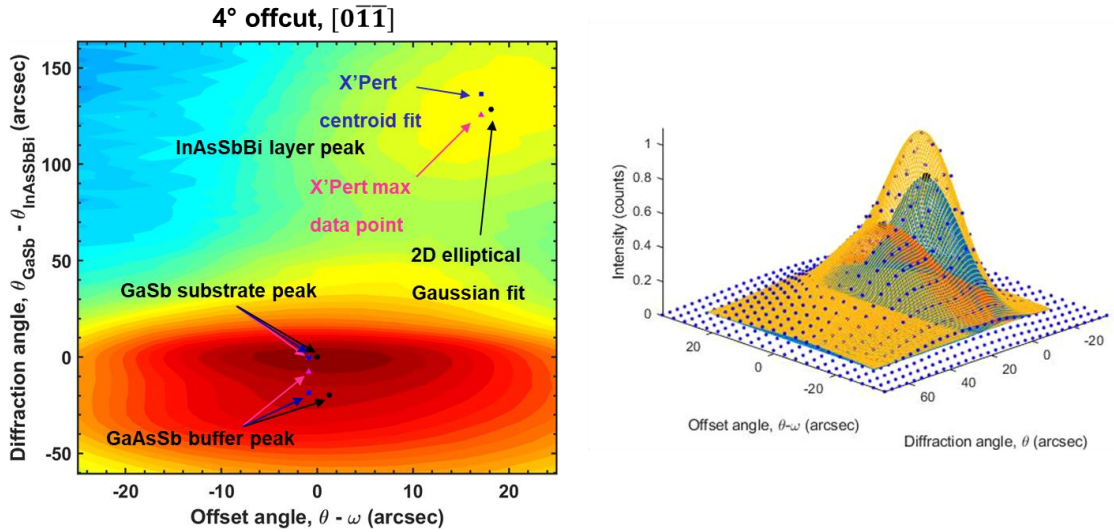

Figure 42. (Left) Comparison of peak locating methods from X'Pert Epitaxy and two-dimensional Gaussian fitting routine on the 4° offcut sample angle area map. The X'Pert Epitaxy maximum data point and centroid peak locations are shown as pink triangles and blue squares, respectively. The two-dimensional Gaussian peak locations are shown as black dots. (Right) A two-term, two-dimensional Gaussian fit of the substrate and buffer peaks from the 4° offcut sample. The individual Gaussians for the substrate and buffer are shown as blue and orange meshes, respectively. The total fit is shown as the yellow mesh. The substrate and buffer peak locations are shown as black dots

The X'Pert Epitaxy software provides two methods of extracting the peak positions of angle area maps: the maximum data point method and the centroid method. For both peak locating methods, the user selects a rectangular region on the map to find the peak position. Within the selected region, the maximum data point method selects the most intense data point and the centroid method fits a centroid to determine the peak location. Locating the peaks through both of these methods provides inconsistent results since the selected region is chosen arbitrarily. Further, both methods are limited to the resolution of the measured data. That is, once a peak

finding method is used in X'Pert Epitaxy, the peak location is not interpolated and is listed as a measured data point. In practice, the peak location can be found more accurately by interpolation from a fit.

The X'Pert Epitaxy maximum data point and centroid peak locations are shown as pink triangles and blue squares, respectively. The two-dimensional Gaussian peak locations are shown as black dots. Both X'Pert peak location methods show the substrate and layer peaks to appear skewed to the left of the center of the contours. The two-dimensional Gaussian approach appears to locate the peak positions in the center of the contours. However, the buffer peak position found using this approach appears to be skewed to the right. This may be due to interference effects which are discussed below.

Dynamical simulations are useful for extracting the Bragg angle of the epilayers as they account for interference effects. Although X'Pert Epitaxy does not provide the capability to simulate angle area scans, offset lines can be extracted from angle area scans for use in a dynamical simulation to accurately determine the out-of-plane distortion. The offset lines extracted from angle area scans measured in the $[0\bar{1}\bar{1}]$ and $[011]$ directions and the coupled scans measured in the $[0\bar{1}1]$ and $[0\bar{1}1]$ directions are plotted in Figure 43.

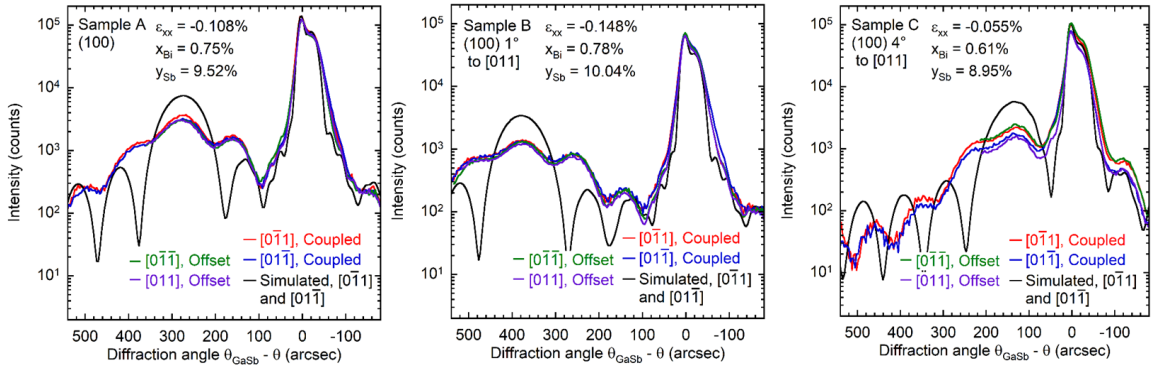

Figure 43. Diffraction patterns for the on-axis (left), 1° offcut (center), and 4° offcut (right) samples from offset lines extracted from angle area scans in the $[0\bar{1}\bar{1}]$ (green) and $[011]$ (purple) directions, coupled scans measured in the $[0\bar{1}1]$ (red) and $[01\bar{1}]$ (blue) directions, and the dynamical simulation (black)

There appears to be no difference between the diffraction patterns extracted from different forms of measurement. Since the coupled scans measured perpendicular to the tilt direction and the offset lines extracted from angle area scans cross through the substrate and epilayer diffraction peaks, the resulting diffraction patterns are equivalent. Therefore, the diffraction pattern measured from either method can be used in a dynamical simulation to account for interference effects.

Thin-film interference and peak interference shift the position of a diffraction peak of interest. X-ray diffraction thin-film interference is the interference of X-rays diffracting from the upper and lower boundaries of an individual layer within the sample structure. In addition to a layer interfering with itself from thin-film interference, other layers within the sample interfere with the diffraction peak. Since the mole fractions are adjusted in the simulation until the simulated peak matches the measured peak, the lattice constant of each layer is computed. Subsequently, the Bragg angle is found from the lattice constant. It is worth noting that the Bragg angle extracted from the dynamical simulation is not equivalent to the peak position in the simulated diffraction pattern. The Bragg angle obtained from the dynamical simulation accounts for interference effects while the peak of the simulated diffraction pattern does not.

A common strategy for finding diffraction pattern peak positions without the use of dynamical simulation is to fit a Gaussian to each individual peak. However, merely locating the peak positions of a coupled scan is not an effective method for calculating lattice constants because

interference effects are not accounted for. To illustrate this point, Table 22 compares the Bragg angle separations of the GaSb substrate and the InAsSbBi layer and GaAsSb buffer extracted from dynamical simulations to the angular separations from the simulated diffraction patterns, the coupled scans measured perpendicular to the tilt direction, and angle area scans measured in the tilt direction.

Table 22. Results from $[0\bar{1}1]$ and $[\bar{0}11]$ coupled scans aligned to the substrate peak for both the InAsSbBi layer and the GaAsSb buffer layer. Angular separations between the Bragg angles extracted from the dynamical simulations, $\theta_{GaSb} - \theta_{Layer}$, the peak separations from the simulated diffraction pattern, $\theta_{GaSb} - \theta_{Simulated}$, the peak separations from the coupled scans, $\theta_{GaSb} - \theta_{Coupled}$, and the peak separations from the angle area scans, $\theta_{GaSb} - \theta_{Area}$ are shown

Sample		On-axis		1° offcut		4° offcut	
		InAsSbBi layer	GaAsSb buffer	InAsSbBi layer	GaAsSb buffer	InAsSbBi layer	GaAsSb buffer
Bragg angle separation $\theta_{GaSb} - \theta_{Layer}$ (arcsec)		273.6	-14.9	373.6	-14.9	138.7	-14.9
Peak separation from simulated pattern $\theta_{GaSb} - \theta_{Simulated}$ (arcsec)		270.9	-24.1	375.0	-22.8	129.8	-21.3
Peak separation from coupled scans $\theta_{GaSb} - \theta_{Coupled}$ (arcsec)	$[0\bar{1}1]$	272.5	-20.5	373.9	-17.2	129.3	-16.3
	$[\bar{0}11]$	273.2	-19.2	375.3	-17.7	129.0	-15.1
Peak separation from angle area scans $\theta_{GaSb} - \theta_{Area}$ (arcsec)	$[\bar{0}\bar{1}1]$	274.0	-17.8	374.2	-18.3	127.1	-19.8
	$[011]$	277.2	-18.6	375.0	-17.2	128.3	-19.7

Angular separations between the Bragg angles extracted from the dynamical simulations, $\theta_{GaSb} - \theta_{Layer}$, the peak separations from the simulated diffraction pattern, $\theta_{GaSb} - \theta_{Simulated}$, the peak separations from the coupled scans, $\theta_{GaSb} - \theta_{Coupled}$, and the peak separations from the angle area scans, $\theta_{GaSb} - \theta_{Area}$ are shown. The peak positions of the substrate and buffer are found by fitting a two-term Gaussian to both the simulated and measured scans. One term in the Gaussian fit corresponds to the substrate and the other to the buffer. The InAsSbBi layer peak positions are found by fitting a one-term Gaussian to both the simulated and measured scans. The difference between the Bragg angle and peak separation is relatively small for the InAsSbBi layer in the on-axis and 1° offcut sample. However, this difference is larger for the 4° offcut sample since the InAsSbBi layer contains less strain than the other samples and is therefore

closer in angle to the substrate and buffer. Thus, the less strained InAsSbBi layer peak from the 4° offcut sample experiences more interference.

This interference effect is also present in the diffraction peak of the buffer layers in each sample. Since the buffer peaks contain such low levels of strain, the substrate diffraction peak heavily interferes with the buffer diffraction peak. Thus, the difference between the Bragg angle and peak position separation is larger for the buffer peaks than from the InAsSbBi peak. The discrepancy between the peak separations and Bragg angle separations shows that performing a dynamical simulation is necessary to account for the effects of thin-film interference.

For growth of a strained layer on an (100) on-axis substrate, the epilayer experiences in-plane biaxial strain on the surface of the wafer. Therefore, the strained epilayer undergoes tetragonal distortion in the out-of-plane direction to accommodate lattice mismatch. When the substrate is offcut, the surface is no longer a (100) plane but rather a high index plane. An epilayer grown on the high index plane of an offcut substrate surface experiences biaxial strain in that surface plane. Just as in the on-axis case, the epilayer distorts normal to the offcut surface to accommodate strain. Since cubic materials contain isotropic strain, the biaxial strain in the offcut surface will distort the epilayer unit cell normal to the surface. This distortion normal to the offcut surface tilts the epilayer both out-of-the-plane and in-the-plane

Since the epilayer distorts normal to the offcut surface, the epilayer contains both an out-of-plane and in-plane distortion component. As a result, the strained epilayer tilts relative to the substrate lattice planes to accommodate the lattice mismatch and boundary conditions. A diagram for a tilted epilayer coherently strained to an offcut substrate is shown in Figure 44 where the vertical and horizontal lattice planes of the epilayer (in red) are registered to the respective lattice planes of the substrate (in black).

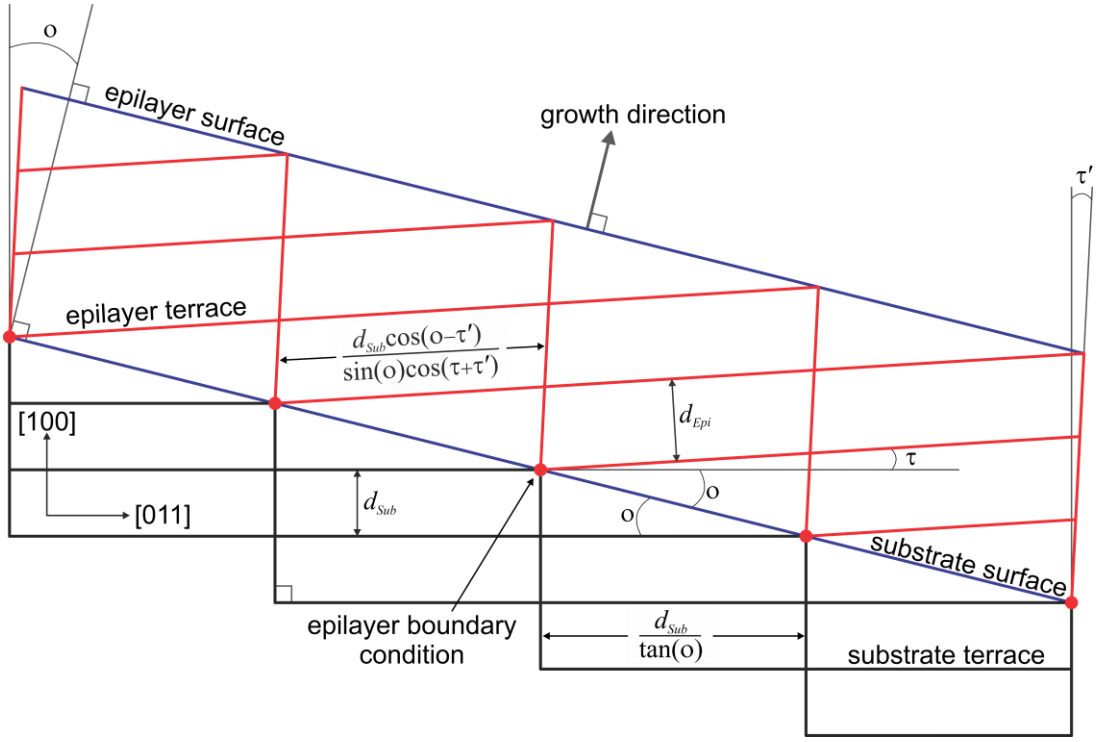

Figure 44. Diagram of strained epilayers grown on offcut substrates. The substrate is shown in black with step edges a height of half of one monolayer. The epilayer, shown in red, grows tilted by an angle τ to accommodate strain at the step edges

The substrate offcut angle is labeled o for offcut and the epilayer tilt angle is labeled τ for tilt. As the growth progresses away from the substrate, the distorted epilayer forms a tilted set of orthogonal lattice planes as shown in red in the cross-section, which is valid for epilayers that are much thicker than the epilayer lattice constant. The epilayer boundary conditions are such that it is registered both in-the-plane on the step terrace and out-of-the-plane at the step edge, shown as red circles.

The tilt between the epilayer and substrate lattice planes can be modeled according to the boundary conditions of the growth. This can be more clearly seen at the boundary of a substrate step edge along one full terrace length shown in Figure 45.

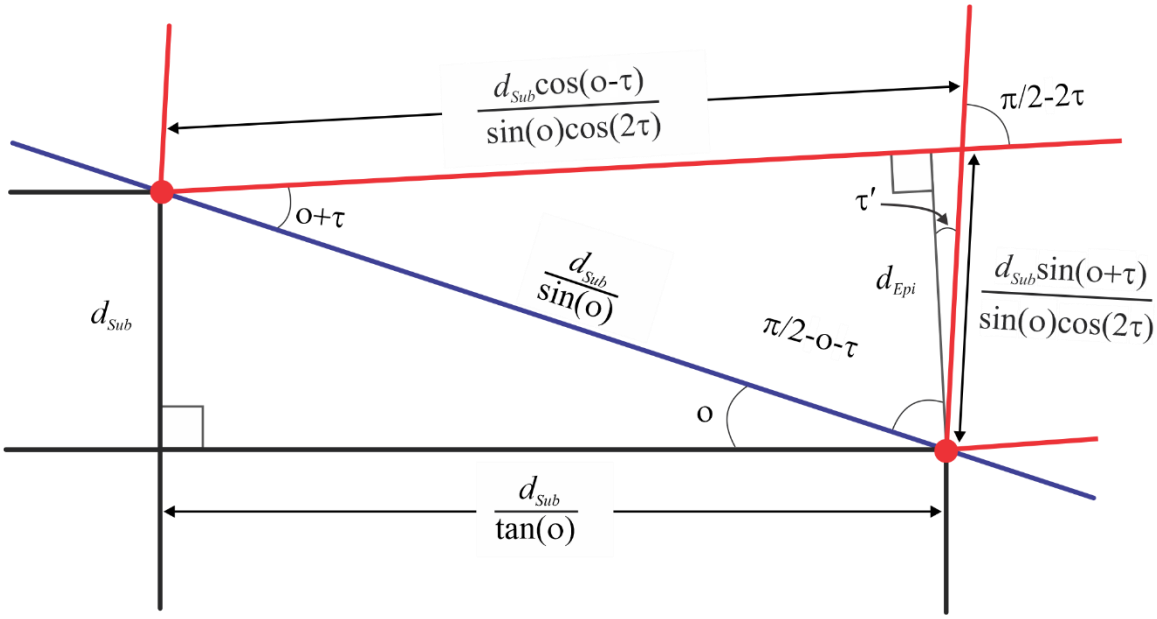

Figure 45. Diagram of tilt model at a step edge. The step heights and terrace lengths for both the substrate and epilayer are listed. Growth of the strained epilayer on the offcut substrate must be registered to the boundary conditions on the step edges shown as red circles

For cubic materials, each substrate step edge has a height equal to the thickness of one half of a monolayer $d_{Sub} = \frac{1}{2}a_{Sub}$ and the length of each step terrace has length $\frac{d_{Sub}}{\tan o}$. The substrate surface (blue) is offset from the substrate terrace by the offcut angle o. Relative to the substrate surface, the epilayer step terrace is offset by an angle $o + \tau$. The epilayer step terrace length is $\frac{d_{Sub}\cos(o+\tau)}{\sin(o)\cos(2\tau)}$ and step edge height is $\frac{d_{Sub}\sin(o+\tau)}{\sin(o)\cos(2\tau)}$. The perpendicular distance between the epilayer lattice planes in the direction normal to the epilayer step terraces is $d_{Epi} = \frac{1}{2}a_{\perp}$.

The tilt between the substrate and epilayer lattice planes is related to their interplanar spacings through the following relation

$$\sin(o+\tau) = \frac{d_{Epi}}{d_{Sub}}\sin(o) \tag{7}$$

The ratio of the spacing between the epilayer and substrate lattice planes is equivalent to the of out-of-plane distortion. That is, $\frac{a_{\perp}}{a_{Sub}} = \frac{d_{Epi}}{d_{Sub}} = (\epsilon_{\perp} + 1)$ such that Eq. (7) becomes

$$\sin(o+\tau) = (\epsilon_{\perp} + 1)\ \sin(o). \tag{8}$$

Solving Eq. (8) for the tilt angle and expanding as a power series for small out-of-plane distortion, $\epsilon_\perp$, yields an approximation for the tilt angle,

$$\tau = \sin^{-1}(\sin(o)\,(\epsilon_\perp + 1)) - o = \epsilon_\perp \tan(o) + \epsilon_\perp^2 \frac{\tan^3(o)}{2} + \cdots \approx \epsilon_\perp \tan(o). \tag{9}$$

The tilt model for the epilayer out-of-plane tilt is comprised of Eq. (9) which defines that a strained epilayer will tilt as a function of the amount of out-of-plane distortion it experiences and the offcut angle it is growing upon.

In addition to tilting out-of-the-plane, the epilayer unit cell also tilts in-the-plane by an angle τ'. The in-plane tilt τ' is derived from the diagram in Figure 46.

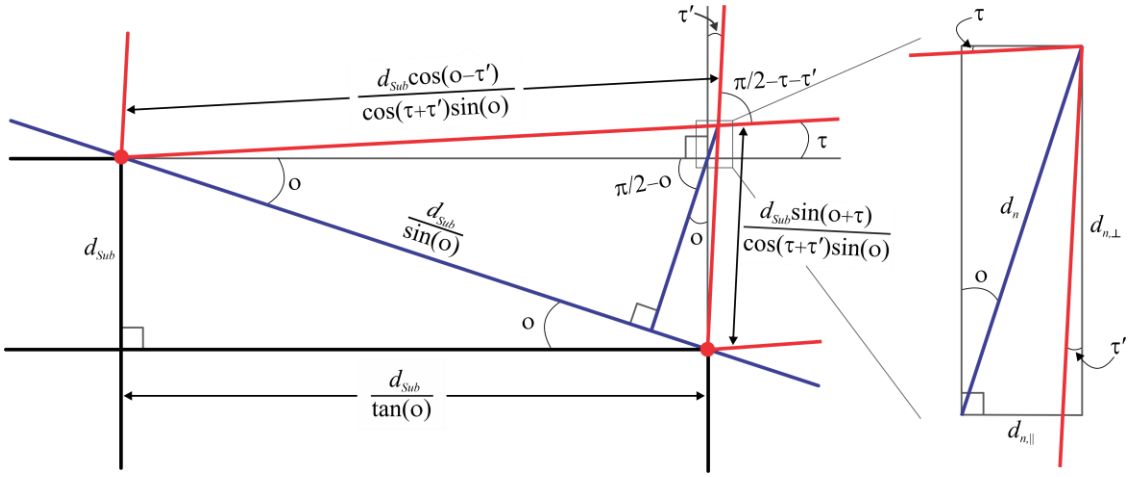

Figure 46. (Left) Diagram of tilt model at a step edge illustrating the distortion occurs normal to the growth direction. The substrate step edge is shown as a reference as a gray line. (Right) The epilayer distortion, d_n, occurs normal to the substrate surface for materials with isotropic strain

The epilayer distorts normal to the substrate surface by an amount d_n. The total distortion can be decomposed into out-of-plane and in-plane distortion components given by $d_{n,\perp}$ and $d_{n,||}$, respectively. The out-of-plane distortion component is the amount the epilayer step distorts normal to the substrate terrace and is given as

$$d_{n,\perp} = d_{Sub}\frac{\cos(o-\tau')\sin(\tau)}{\cos(\tau+\tau')\sin(o)}. \tag{10}$$

The in-plane distortion component is the amount the epilayer terrace distorts normal to the substrate step and is given as

$$d_{n,||} = d_{Sub}\frac{\sin(o+\tau)\sin(\tau')}{\cos(\tau+\tau')\sin(o)}. \tag{11}$$

The ratio of the in-plane to out-of-plane distortion components forms the tangent of the offcut angle, given as

$$\tan(o) = \frac{d_{n,||}}{d_{n,\perp}} = \frac{d_{Sub}\frac{\sin(o+\tau)\sin(\tau')}{\cos(\tau+\tau')\sin(o)}}{d_{Sub}\frac{\cos(o-\tau')\sin(\tau)}{\cos(\tau+\tau')\sin(o)}} = \frac{\sin(o+\tau)\sin(\tau')}{\cos(o-\tau')\sin(\tau)} \tag{12}$$

$$= \frac{(\sin(o)\cos(\tau)+\cos(o)\sin(\tau))\sin(\tau')}{(\cos(o)\cos(\tau')+\sin(o)\sin(\tau'))\sin(\tau)} = \frac{\frac{\sin(o)}{\tan(\tau)}+\cos(o)}{\frac{\cos(o)}{\tan(\tau')}+\sin(o)} = \frac{\frac{\tan(o)}{\tan(\tau)}+1}{\frac{1}{\tan(\tau')}+\tan(o)}$$

Solving for the tangent of the in-plane tilt τ' yields the expression

$$\frac{1}{\tan(\tau')} = \frac{\frac{\tan(o)}{\tan(\tau)}+1}{\tan(o)} - \tan(o) = \frac{\frac{\tan(o)}{\tan(\tau)}+1-\tan^2(o)}{\tan(o)} = \frac{\frac{\tan(o)}{\tan(\tau)}+\frac{2\tan(o)}{\tan(2o)}}{\tan(o)} \quad (13)$$
$$= \frac{1}{\tan(\tau)} + \frac{2}{\tan(2o)}.$$

Solving for the in-plane tilt angle and expanding for small out-of-plane tilt angles gives

$$\tau' = \tan^{-1}\left(\frac{\tan(\tau)\tan(2o)}{2\tan(\tau)+\tan(2o)}\right) = \tau - \frac{2}{\tan(2o)}\tau^2 + \frac{4}{\tan^2(2o)}\tau^3 - \cdots \approx \tau \quad (14)$$

Thus, the in-plane tilt angle is approximately the same as the out-of-plane tilt angle. For varying degrees of offcut angle, the in-plane tilt obeys the following relations,

$$\tau' < \tau, \qquad o < 45° \quad (15a)$$

$$\tau' = \tau, \qquad o = 45° \quad (15b)$$

$$\tau' > \tau, \qquad o > 45°. \quad (15c)$$

Since the offcut angles of the GaSb substrates are less than 45°, the in-plane tilt of the InAsSbBi epilayers is slightly smaller than the out-of-plane tilt. Using the offcut angle provided by the wafer manufacturer and the out-of-plane distortion extracted from a dynamical simulation of coupled scans, the in-plane and out-of-plane tilt angles are provided in Table 23.

Table 23. Calculated out-of-plane tilt τ and in-plane tilt τ' of the InAsSbBi epilayer grown on on-axis, 1° offcut, and 4° offcut GaSb substrates

	Tilt (arcsec)	
	In-plane tilt τ	Out-of-plane tilt τ'
On-axis	0	0
1° offcut	11.13	11.10
4° offcut	16.56	16.54

The tilt model presented in the previous sections can be tested experimentally from the (400) angle area map results presented in Figure 41 on page 47. The scans are measured in the maximum tilt directions ($[0\bar{1}1]$ and $[011]$) for each sample. The tilt angle of the InAsSbBi layer and the GaAsSb buffer layer are measured directly from the (400) angle area maps. The experimental results are compared to the tilt model presented in the previous section, shown in Figure 47.

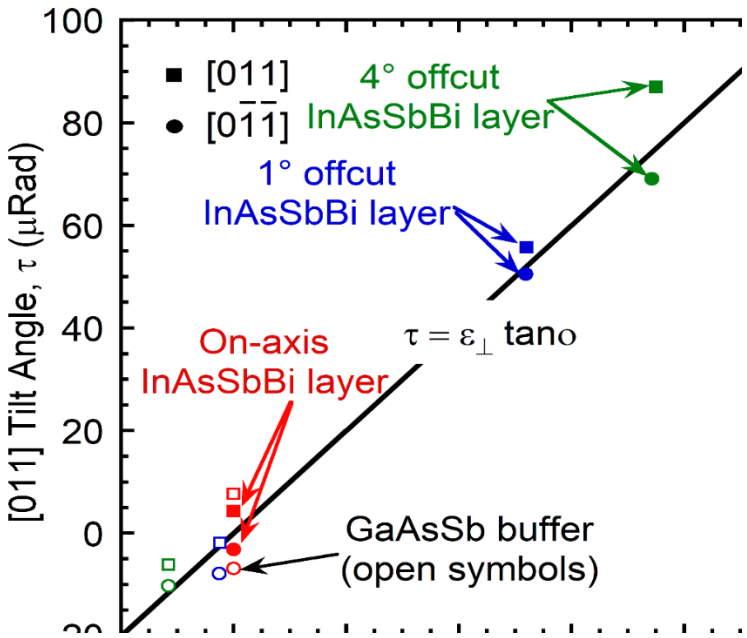

Figure 47. Modeled (black line) versus measured tilt angle for the InAsSbBi layer (filled data points) and the GaAsSb buffer (open data points) in the $[0\bar{1}\bar{1}]$ (circles) and $[011]$ (squares) directions. The tilt model equation is displayed in the black line

The modeled tilt angle is drawn as a straight line and the GaAsSb buffer (open data points) and InAsSbBi layer (filled data points) measured tilt angles are plotted as points. The tilt angles are plotted as circles when measured in the $[0\bar{1}\bar{1}]$ direction and squares when measured in the $[011]$ direction. The calculated tilt from the model and average measured tilt from the two scan directions is listed in Table 24. The tilt from the model is calculated from Eq. (9) using the supplied offcut angle and the out-of-plane distortion extracted from dynamical simulations of the X-ray diffraction pattern.

Table 24. Calculated tilt from model and average measured tilt from angle area scans in the $[0\bar{1}\bar{1}]$ and $[011]$ directions

	Tilt from model (arcsecs)		Average tilt from measurement (arcsecs)	
	InAsSbBi layer	GaAsSb buffer	InAsSbBi layer	GaAsSb buffer
On-axis	0	0	1.6	0.1
1° offcut	10.8	-0.51	10.8	-1.0
4° offcut	15.4	-2.4	15.3	-1.7

The epilayer unit cell is a monoclinic oblique rhombic prism as a result of the in-plane and out-of-plane distortion and tilt. A monoclinic unit cell defined by three angles α, β, and γ. and three lattice constants a, b, and c is displayed in Figure 48. The unit cell is distorted by an angle τ' in-the-plane as well as an angle τ out-of-the-plane in the direction of the offcut resulting in a total tilt of $\tau + \tau' \approx 2\tau$ relative to the substrate unit cell.

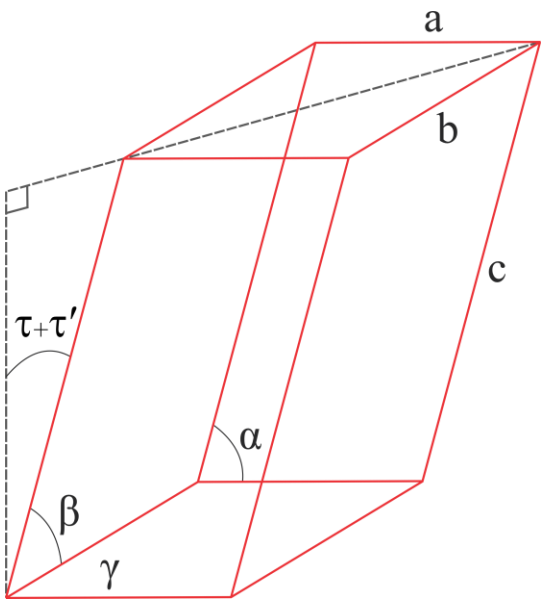

Figure 48. Monoclinic unit cell drawn relative to the InAsSbBi epilayer terrace. The lattice constants are a, b, and c and the three angles characterizing the monoclinic distortion are α, β, and γ. The total distortion of the unit cell is $\tau + \tau' \approx 2\tau$ in the direction of the offcut. The tilt direction is drawn along the diagonal of the unit cell

Since the epilayer unit cell is distorted, the orthogonal distance between the out-of-plane lattice that X-ray diffraction measures is not equal to the out-of-plane lattice constant of the epilayer unit cell. Thus, the epilayer out-of-plane lattice constant is not measured directly. Instead, the interplanar distance $2d_{Epi}$ is measured which is offset from the out-of-plane lattice constant by an angle $\tau + \tau' \approx 2\tau$. The out-of-plane lattice constant is then

$$\begin{aligned} c &= \frac{a_{Sub}\sin(o+\tau)}{\cos(\tau+\tau')\sin(o)} \\ &= a_{Sub}\left(1+\frac{1}{\tan(o)}\tau+\frac{3}{2}\tau^2+\cdots\right) = a_{Sub}(\varepsilon_\perp+1)(1+2\tau^2+\cdots) \\ &\approx a_{Sub}\left(1+\frac{1}{\tan(o)}\tau\right) = a_{Sub}(1+\epsilon_\perp), \end{aligned} \tag{16}$$

which is derived from the epilayer step height in Figure 45. When the tilt is in the diagonal unit cell direction, the epilayer in-plane lattice constants are equal, $a = b$, by symmetry. However, the lengths along the diagonals of the unit cell are slightly different. In the direction along the step edge, the diagonal of the epilayer unit cell is registered to the diagonal of the substrate unit cell. However, in the direction of the tilt, the diagonal of the epilayer unit cell is slightly elongated, as seen in the epilayer terrace in Figure 45.

Due to the boundary conditions, the ratio of the epilayer to substrate terrace lengths is equal to the ratio of the epilayer to substrate diagonal unit cell lengths. That is, the ratio of the epilayer to substrate terrace lengths is $\frac{\cos(o-\tau')}{\cos(\tau+\tau')\cos(o)}$ and the ratio of the epilayer to substrate diagonal unit

cell lengths is $\frac{l}{\sqrt{2}a_{sub}}$. Setting these two ratios equal and solving for the diagonal length l in the direction of the tilt provides

$$l = \sqrt{2}a_{Sub}\frac{\cos(o-\tau')}{\cos(\tau+\tau')\cos(o)}. \tag{17}$$

An epilayer unit cell viewed from above is shown in Figure 49.

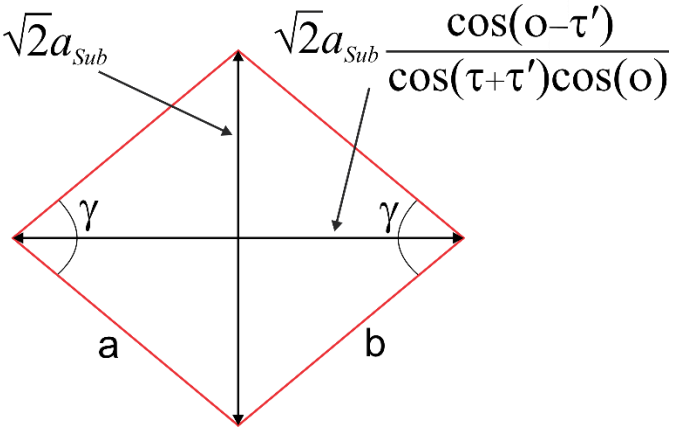

Figure 49. Epilayer unit cell viewed from above. The lengths of the diagonals are shown as double-sided arrows and the in-plane unit cell angle γ is shown

The lengths of the diagonals are shown as double-sided arrows and the in-plane unit cell angle γ is shown. Using the Pythagorean Theorem in **Figure** 49, the epilayer in-plane lattice constants are

$$a = b = \frac{\sqrt{2}a_{Sub}}{2}\sqrt{1+\left(\frac{\cos(o-\tau')}{\cos(\tau+\tau')\cos(o)}\right)^2}. \tag{18}$$

The unit cell angle γ is defined as $\tan\left(\frac{\gamma}{2}\right) = \frac{\cos(o)\cos(\tau+\tau')}{\cos(o-\tau')}$ from **Figure** 49. Solving for γ provides

$$\gamma = 2\tan^{-1}\left(\frac{\cos(o)\cos(\tau+\tau')}{\cos(o-\tau')}\right) = \frac{\pi}{2} - \tan(o)\,\tau - \frac{1}{2\cos^2(o)}\tau^2 - \cdots \approx \frac{\pi}{2} - \tan(o)\,\tau. \tag{19}$$

Since the distortion occurs in the direction diagonal to the unit cell, the angles α and β are symmetric. A triangular plane intersecting the unit cell is shown in Figure 50 to determine these angles.

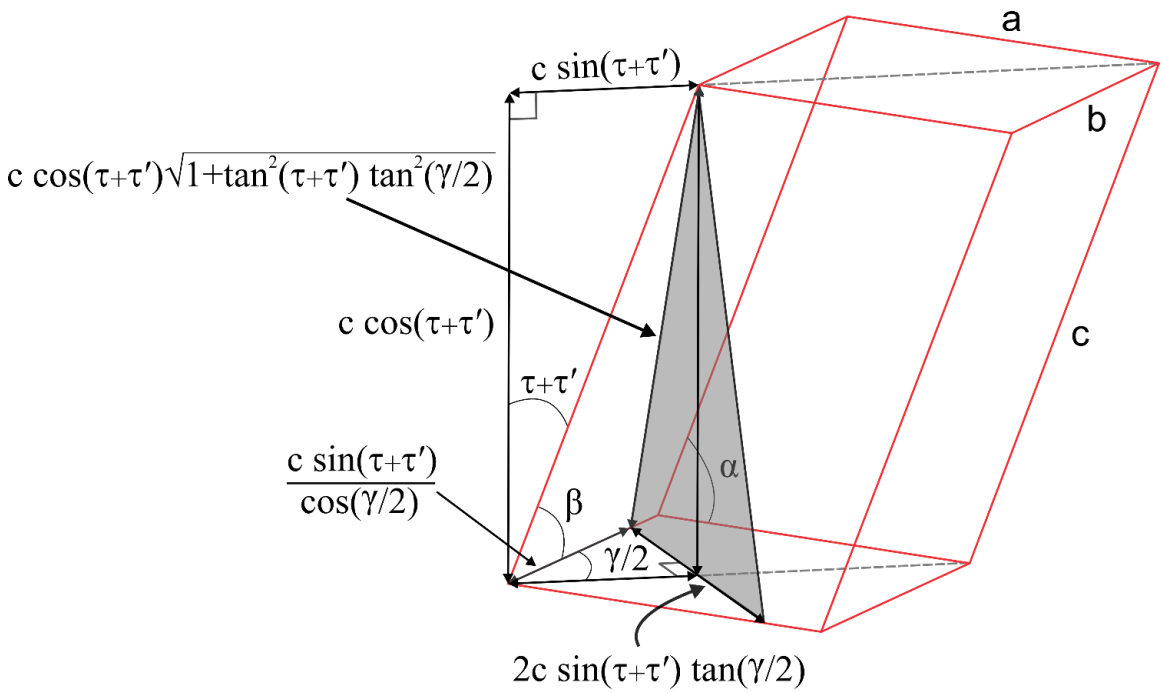

Figure 50. Unit cell angles α and β are extracted from a triangular plane intersecting the unit cell, shown in gray. All relevant lengths are shown

The intersecting triangular plane forms a triangle on the face of the unit cell containing the angle β. Using the law of cosines, $\cos(\alpha)$ and $\cos(\beta)$ are found to be

$$\cos(\alpha) = \cos(\beta) = \sin(\tau+\tau')\cos\left(\frac{\gamma}{2}\right) = \frac{\sin(\tau+\tau')}{\sqrt{1+\frac{\cos^2(o)\cos^2(\tau+\tau')}{\cos^2(o-\tau)}}} \tag{20}$$

Solving for the out-of-plane angles gives

$$\alpha = \beta = \cos^{-1}\left(\frac{\sin(\tau+\tau')}{\sqrt{1+\frac{\cos^2(o)\cos^2(\tau+\tau')}{\cos^2(o-\tau')}}}\right) = \frac{\pi}{2} - \sqrt{2}\tau + \frac{\sqrt{2}\left(\frac{1}{\tan(o)} - 2\tan(o)\right)}{2}\tau^2 - \cdots \approx \frac{\pi}{2} - \tau\sqrt{2}. \tag{21}$$

The epilayer unit cell lattice constants and angles are defined in terms of the substrate lattice constant and offcut angle and the epilayer tilt angle. Using the calculated tilt angles, the unit cell angle and lattice constant differences between the epilayer and substrate are calculated and listed in Table 25.

Table 25. InAsSbBi unit cell angles, tilt angles, and lattice constants differences from the GaSb substrate for the on-axis, 1° and 4° offcut InAsSbBi samples

	Unit cell tilt (arcsec)		Unit cell lattice constants		Unit cell angles (arcsec)	
	τ	τ'	$a - a_{GaSb}$, $b - a_{GaSb}$	$c - a_{GaSb}$	$\pi/2 - \alpha$, $\pi/2 - \beta$	$\pi/2 - \gamma$
On-axis	0	0	0	0.0138	0	0
1° offcut	11.13	11.10	2.8758×10^{-6}	0.0188	15.72	0.19
4° offcut	16.56	16.54	1.7119×10^{-5}	0.0070	23.40	1.16

The lattice planes of the strained epilayers grown on the offcut substrates tilt relative to the plane of substrate offcut as a means to accommodate the in-surface biaxial-strain and the out-of-surface distortion. The crystallographic tilt and the out-of-plane distortion results in an monoclinic oblique rhombic prism unit cell when the offcut is in the high symmetry $[011]$ direction, rather than tetragonal for on-axis growth. In addition to the out-of-plane tilt τ of the epilayer, there is an in-plane tilt of $\tau' \approx \tau$ at the step edge. Both tilts are a result of the epilayer boundary conditions, which is constrained in the plane of the substrate surface by coherent growth on both the (100) terrace surface and the (011) step edge surface, and distorts in the growth direction that is perpendicular to the surface of the offcut substrate. Both the in-plane and out-of-plane lattice constants are larger than the GaSb substrate lattice constants. The unit cell angles are all less than the substrate unit cell angle $\pi/2$. The unit cell has two equal in-plane and one unequal out of plane lattice constants ($a = b \neq c$) and two equal out of plane and one unequal in plane lattice angles ($\alpha = \beta \neq \gamma$).

4.9 Characterization of InAsSb, GaInAsSb, InAsSbBi, and GaInAsSbBi

This work compares the structural and optical properties of InAsSb, GaInAsSb, InAsSbBi, and GaInAsSbBi. The sample cross sections are shown in Figure 51.

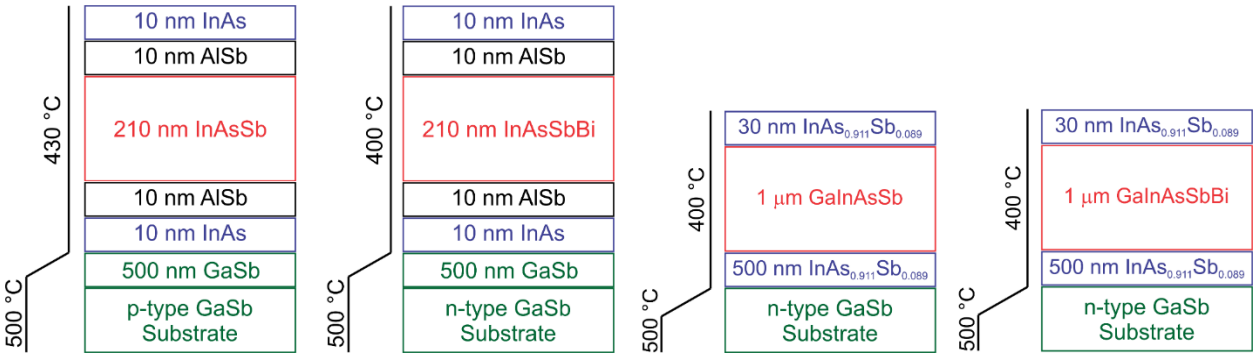

Figure 51. Sample cross sections of InAsSb, InAsSbBi, GaInAsSb, and GaInAsSbBi

The InAsSb and InAsSbBi samples consist of a 500 nm GaSb buffer, a 10 nm InAs/10 nm AlSb partially strain balanced barrier, the InAsSb or InAsSbBi active region, and a terminating 10 nm AlSb/10 nm InAs barrier/cap layer. The GaSb buffer layer is grown at 500 °C except for the last 70 nm where the substrate temperature is reduced by 70 to 100 °C in preparation for the growth

of the InAsSb or InAsSbBi active layer. The GaInAsSb and GaInAsSbBi samples consist of a 500 nm buffer and 30 nm cap of lattice matched InAsSb with a 1 μm thick active region of GaInAsSb or GaInAsSbBi. The sample growth parameters, substrate orientation, surface morphology, in-plane strain, zero-temperature bandgap energy, and mole fractions determined from X-ray diffraction and photoluminescence measurements are listed in Table 26.

Table 26. Sample run number, substrate orientation, growth temperature, V/In flux ratios, average mole fractions, in-plane strain, and presence of surface droplet features

Sample	Material	Growth Temp (°C)	Flux Ratios				Mole Fractions (%)					In-plane strain ϵ_{xx} (%)	Zero-temp. bandgap (meV)	GaSb substrate orientation	Surface Droplets
			Ga/III	Bi/III	Sb/III	As/III	Ga	In	Bi	Sb	As				
B2496	InAsSb	430	0	0	0.126	1.193	0	100	0	8.11	91.89	0.0566	325.9	(100) on axis	No
L21-045	GaInAsSb	400	0.029	0	0.112	0.963	3.52	96.48	0	12.41	87.59	-0.0079	308.6	(100) 0.35° to [011]	No
L21-046	GaInAsSbBi	400	0.029	≈0.02	0.108	0.966	3.52	96.48	0.17	12.44	87.39	-0.0258	300.6	(100) 0.35° to [011]	No
B2563	InAsSbBi	400	0	0.05	0.105	0.911	0	100	0.65	8.83	90.52	-0.055	292.6	(100) 4° to [011]	Yes
B2561	InAsSbBi	400	0	0.05	0.12	0.911	0	100	0.78	9.52	89.7	-0.111	280.7	(100) on axis	Yes
B2562	InAsSbBi	400	0	0.05	0.12	0.911	0	100	0.74	10.07	89.19	-0.149	271.3	(100) 1° to [011]	Yes

The samples are examined using temperature-dependent photoluminescence spectroscopy. The experimental setup is identical to that described in Section (1). Selected photoluminescence spectra at 12 K and Einstein single oscillator fits are shown for each sample in Figure 52.

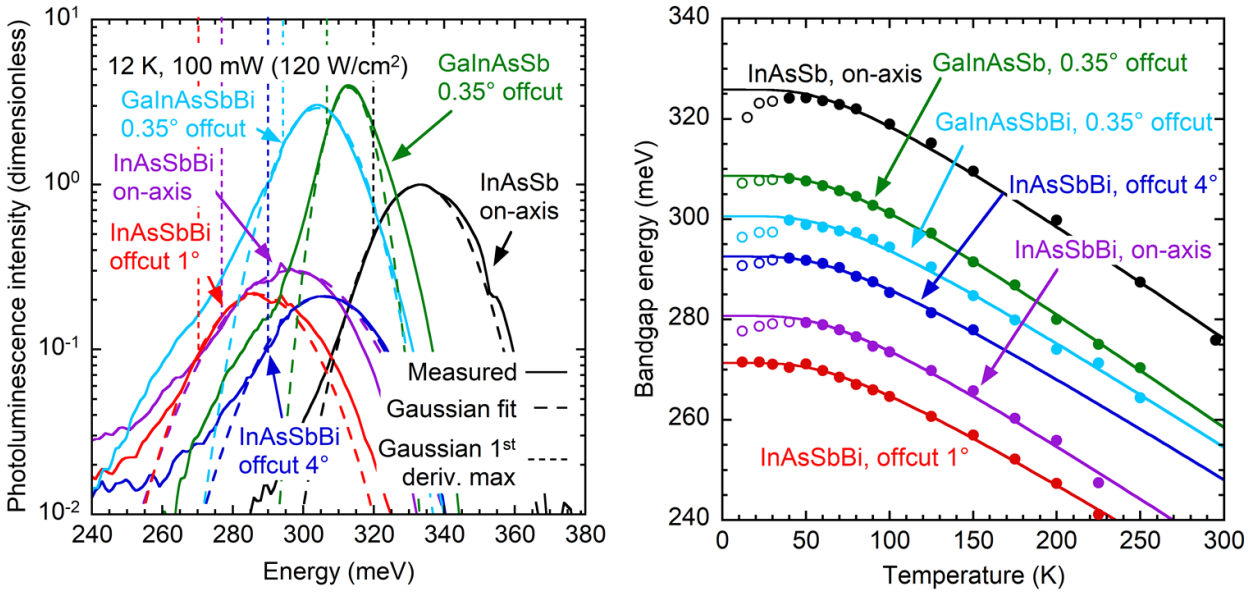

Figure 52. (Left) Photoluminescence spectra of InAsSb, GaInAsSb, InAsSbBi, and GaInAsSbBi samples at 12 K and 100 mW pump power. The solid line represents the measure data, the dashed line represents the Gaussian fit, and the vertical dashed line indicates the bandgap energy. (Right) Einstein single oscillator fits to the temperature dependent bandgaps of the InAsSb, GaInAsSb, InAsSbBi, and GaInAsSbBi samples at temperatures ranging from 12 K to 300 K. The solid circles represent the fitted data points and the open circles are the data points not used in the fit

Each sample exhibits a single well-defined photoluminescence intensity peak. The bandgap at each temperature is identified as the first derivative maximum of the photoluminescence spectrum. The zero-temperature bandgaps are then extracted from an Einstein single oscillator fit provided in Eq. (1). The Einstein single oscillator fit is performed using a constant Einstein temperature of $T_e = 200\,K$. The zero-temperature bandgap energy and coupling parameter extracted from the fits are provided in Table 27.

Table 27. Low-temperature bandgap energy with the corresponding low-temperature wavelength and the coupling parameter extracted from Einstein single oscillator fits to the temperature dependent bandgaps of the InAsSb, GaInAsSb, InAsSbBi, and GaInAsSbBi samples

Sample	Low-temp. bandgap $E_g(x,y,0)$ (meV)	Low-temp. wavelength $\lambda\ (\mu m)$	Coupling parameter S_0 (dimensionless)
InAs	413.2	3.00	3.231
InAsSb	325.9	3.80	2.734
GaInAsSb	308.6	4.02	2.703
GaInAsSbBi	300.2	4.12	2.524
InAsSbBi 4° offcut	292.6	4.24	2.447
InAsSbBi On-axis	280.7	4.42	2.598
InAsSbBi 1° offcut	271.3	4.57	2.433

The integrated photoluminescence intensity is plotted as a function of temperature in Figure 53. Two characteristic slopes appear in the temperature dependent integrated photoluminescence intensity. The initial slope at low temperatures is caused by the increase in the radiative lifetime. More carriers are recombining non-radiatively. At high temperature, another slope emerges as the recombination becomes non-radiatively dominated.

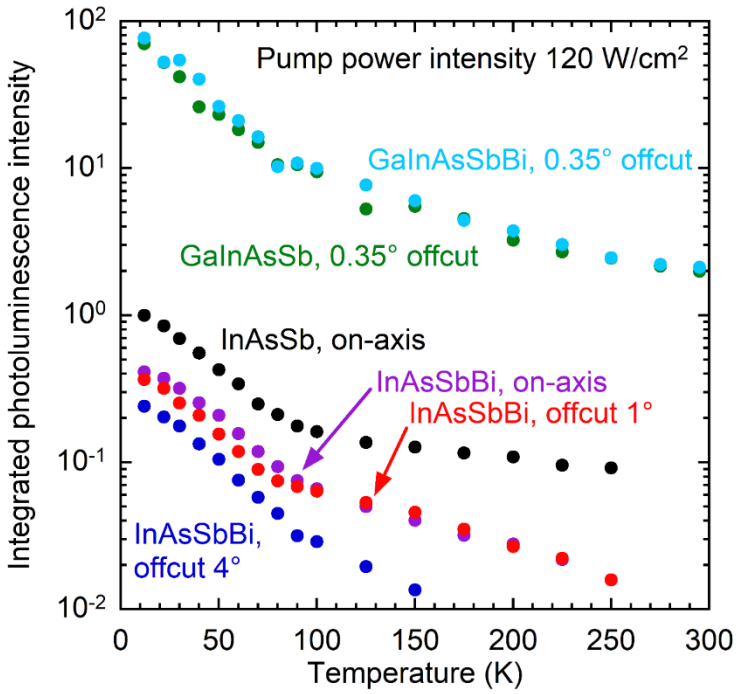

Figure 53. Temperature dependent integrated photoluminescence intensity for the InAsSb, GaInAsSb, InAsSbBi, and GaInAsSbBi samples

The photoluminescence width is plotted as a function of temperature in Figure 54. The zero-temperature photoluminescence width for both the InAsSb and GaInAsSb samples is relatively small around 3 meV. The zero-temperature photoluminescence width increases linearly by 13.2meV/%Bi and 0.29 meV/%Sb. After removing the bandgap shift due to strain, the zero-temperature bandgap decreases linearly by -52.4 meV/%Bi and -10.1 meV/%Sb. These plots show that photoluminescence width can be used as an indicator of how much Bi has incorporated. Further, Bi incorporation drastically impacts the photoluminescence width as well as the reduction in the bandgap energy.

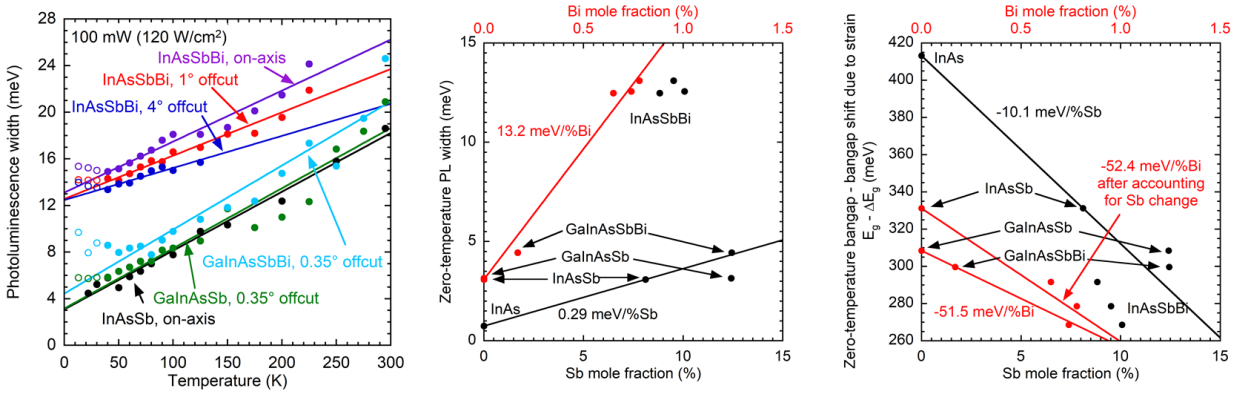

Figure 54. (Left) Photoluminescence width as a function of temperature for the InAsSb, GaInAsSb, InAsSbBi, and GaInAsSbBi samples. Solid lines represent a linear fit, solid circles are the fitted data, and open circles are data not fitted. (Center) Zero-temperature photoluminescence width as a function of Sb and Bi mole fraction where solid lines indicate linear fits. (Right) Zero-temperature bandgap minus the bandgap shift due to strain as a function of the Sb and Bi mole fraction

The Bi mole fraction, zero-temperature width intercept, and photoluminescence width slope is provided in Table 28.

Table 28. Bi mole fraction, zero-temperature width intercept, and photoluminescence width slope for the InAsSb, GaInAsSb, InAsSbBi, and GaInAsSbBi samples

Sample	InAsSbBi, on-axis	InAsSbBi, 1° offcut	InAsSbBi, 4° offcut	GaInAsSbBi, 0.35° offcut	GaInAsSb, 0.35° offcut	InAsSb	InAs
Bi mole fraction (%)	0.78	0.74	0.65	0.17	0	0	0
Zero-temperature width intercept	13.1	12.56	12.47	4.44	3.15	3.09	0.75
Photoluminescence width slope	0.507	0.431	0.319	0.638	0.599	0.586	0.377

The X-ray diffraction measurements are performed using a PANalytical X'Pert Pro MRD X-ray diffractometer with an instrumental resolution of 12 arcsec and Cu $K\alpha_1$ radiation with a 1.540598 Å wavelength. Coupled scans of the (400) planes are measured for each sample and used in a dynamical simulation to extract the Bragg angles of each InAsSbBi layer, which are shown in Figure 55.

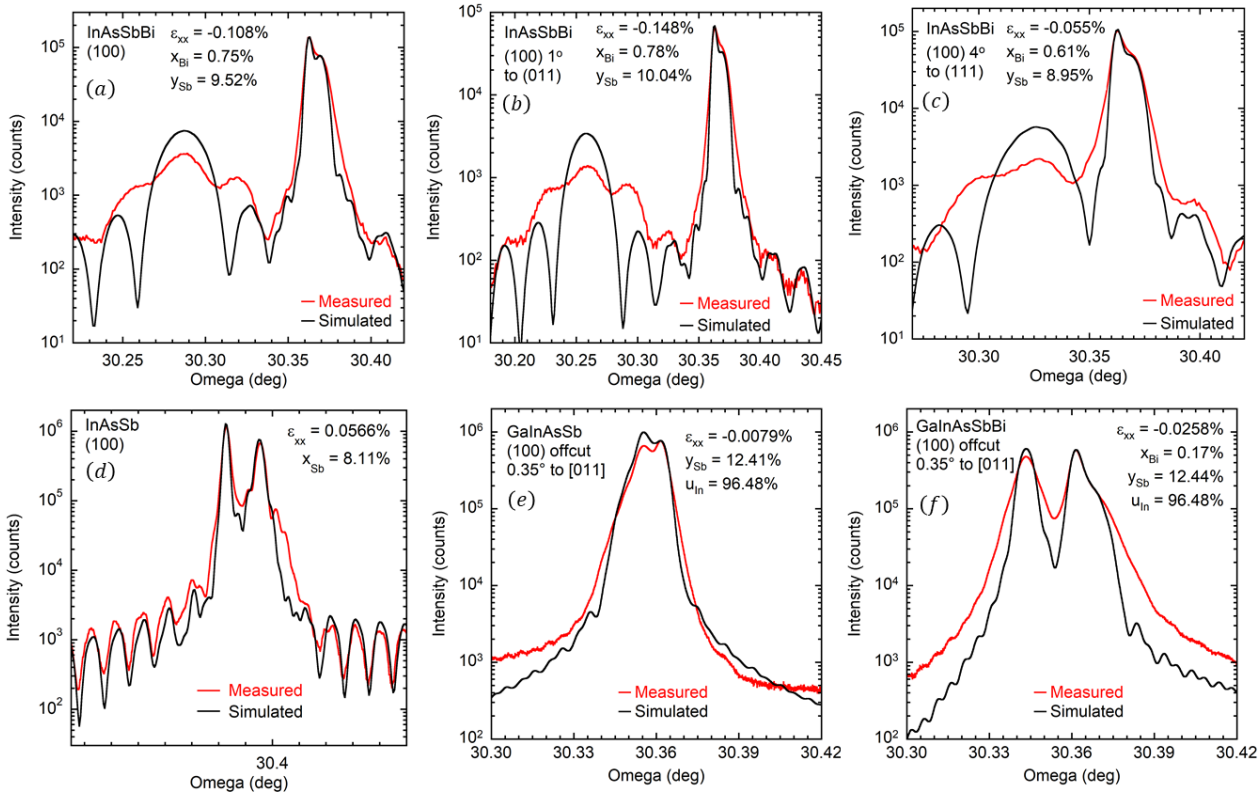

Figure 55. X-ray diffraction coupled scans of InAsSbBi (a-c), InAsSb (d), GaInAsSb (e), and GaInAsSbBi (f). The measured scans are shown as red lines and the simulated diffraction patterns are shown as black lines. Substrate orientation, strain, and mole fractions for each sample are provided in each plot

The InAsSb, GaInAsSb, InAsSbBi, and GaInAsSbBi simulated thickness, in-plane biaxial strain, and lattice constant are provided in Table 29. The InAsSb sample is tensiley strained while all other samples are compressively strained.

Table 29. Simulated thickness, in-plane biaxial strain, and lattice constant extracted from the dynamical simulation of the coupled scans for the InAsSb, GaInAsSb, InAsSbBi, and GaInAsSbBi samples

Sample	Simulated thickness (nm)	In-plane biaxial strain ε_{xx} (%)	Lattice constant $a_{InAsSbBi}$(Å)
InAsSb	265	0.0566	6.0925
GaInAsSb 0.35° offcut	1000	-0.0079	6.0964
GaInAsSbBi 0.35° offcut	1000	-0.0258	6.0975
InAsSbBi 4° offcut	190	– 0.0550	6.0993
InAsSbBi On-axis	194	– 0.1083	6.1025
InAsSbBi 1° offcut	189	– 0.1479	6.1049

The mole fractions for each sample are determined numerically based on the lattice constant measured by X-ray diffraction and zero-temperature bandgap energy determined from photoluminescence. The Sb mole fraction written in terms of the constituent lattice constants and mole fractions is

$$y = \frac{a_{Ga_{1-u}In_uAs_{1-x-y}Sb_yBi_x} - ua_{InAs} - xa_{GaBi} + ux(a_{GaBi} + a_{InAs} - a_{InBi}) - (1-u)(1-x)a_{GaAs}}{a_{GaAs} - a_{GaSb} + u(a_{GaSb} + a_{InAs} - a_{InSb} - a_{GaAs})} \quad (22)$$

where $a_{Ga_{1-u}In_uAs_{1-x-y}Sb_yBi_x}$ is the fully relaxed GaInAsSbBi lattice constant determined from X-ray diffraction, a_{InAs}, a_{GaBi}, a_{InBi}, a_{GaAs}, a_{GaSb}, and a_{InSb} are the InAs, GaBi, InBi, GaAs, GaSb, and InSb lattice constants, respectively, and u, x, and y are the In, Bi, and Sb mole fractions, respectively.

A bandgap bowing model is introduced to determine the quinary zero-temperature bandgap in terms of the mole fractions.

The model is written as

$$\begin{aligned} E_{g,GaInAsSbBi}(u,x,y) &= u(1-x-y)E_{g,InAs} + uyE_{g,InSb} + uxE_{g,InBi} \\ &+(1-u)(1-x-y)E_{g,GaAs} + (1-u)yE_{g,GaSb} + (1-u)xE_{g,GaBi} \\ &-uy(1-x-y)b_{g,InAsSb} - ux(1-x-y)b_{g,InAsBi} - uxyb_{g,InSbBi} \\ &-(1-u)(1-x-y)yb_{g,GaAsSb} - (1-u)(1-x-y)xb_{g,GaAsBi} - (1-u)xyb_{g,GaSbBi} \\ &-u(1-u)(1-x-y)b_{g,InGaAs} - u(1-u)yb_{g,\,GaInSb} - u(1-u)xb_{g,\,GaInBi} + \Delta E_g, \end{aligned} \quad (23)$$

where $E_{g,GaInAsSbBi}$ is the zero-temperature bandgap energy determined from photoluminescence measurements, $E_{g,InAs}$, $E_{g,InSb}$, $E_{g,InBi}$, $E_{g,GaAs}$, $E_{g,GaSb}$, $E_{g,GaBi}$ are the InAs, InSb, InBi, GaAs, GaSb, and GaBi bandgaps, respectively, $b_{g,InAsSb}$, $b_{g,InAsBi}$, $b_{g,InSbBi}$, $b_{g,GaAsSb}$, $b_{g,GaAsBi}$, $b_{g,GaSbBi}$, $b_{g,InGaAs}$, $b_{g,GaInSb}$, $b_{g,GaInBi}$ are the InAsSb, InAsBi, InSbBi, GaAsSb, GaAsBi, GaSbBi, InGaAs, GaInSb and GaInBi bowing parameters, respectively, and ΔE_g is the bandgap shift due to strain calculated from the Pikus-Bir Hamiltonian.

Solving Eq. (23) for the Sb mole fraction y, and setting equal to Eq. (22) provides a means of computing the Bi and In mole fractions numerically. The parameters used to compute the mole fractions in Eqs. (22-23) are provided in Table 30.

Table 30. Lattice constants, zero-temperature bandgaps, bowing parameters, and the source for each parameter used for determining the mole fractions of InAsSb, GaInAsSb, InAsSbBi, and GaInAsSbBi samples

Compound	Lattice constant	Zero-temp. bandgap energy (eV)	Bowing parameter b_g (eV)	Source
InAs	6.0583	0.4134		Vurgaftman et al.(2001)
InSb	6.4794	0.2297		Vurgaftman et al.(2001)
InBi	6.6108[a]	-1.63[b]		[a]Shalindar et. al. (2016), [b]Janotti et al.
GaAs	5.6325	1.519		Vurgaftman et al.(2001)
GaSb	6.0959	0.821		Vurgaftman et al.(2001)
GaBi	6.33[a]	-1.45[b]		[a]Francoeur et. al. (2003), [b]Janotti et al.
InAsSb			0.901	Measured, Schaefer et al. (2019)
InAsBi			$3.629e^{-x/0.229}$	Measured, Schaefer et al. (2019)
InSbBi			$b_{InAsSb} + b_{InAsBi}$	Assumption, Schaefer et al. (2019)
GaAsSb			1.43	Vurgaftman, et al.(2001)
GaAsBi			2.69	Fit to VBAC expression from Alberi et al. (2007) in $0 \leq x_{Bi} \leq 10\%$ range
GaSbBi			1.23	Fit to VBAC expression from Alberi et al. (2007) in $0 \leq x_{Bi} \leq 10\%$ range
InGaAs			0.477	Vurgaftman et al.(2001)
InGaSb			0.413	Roth (1980)
InGaBi			0.000	No published values

To fully characterize the GaInAsSbBi mole fractions, three independent measurements would need to be completed. However, only X-ray diffraction and temperature-dependent photoluminescence measurements were performed. Therefore, it is assumed that the Ga mole fraction is the same between the GaInAsSb and GaInAsSbBi since the Ga flux was the same for both growths. That is, the Ga mole fraction is calculated to be 3.52% for the GaInAsSb sample and is then set exactly equal for the GaInAsSbBi sample. Then the numerical mole fraction analysis described above is applied to determine the Sb and Bi mole fractions.

4.10 Characterization of type-II InAs/InAsSb and InGaAs/InAsSb superlattices

This work aims to compute the mobility of InAs/InAsSb and InGaAs/InAsSb type-II superlattices using steady-state and time-resolved photoluminescence measurements. The sample structures considered are shown in Figure 56.

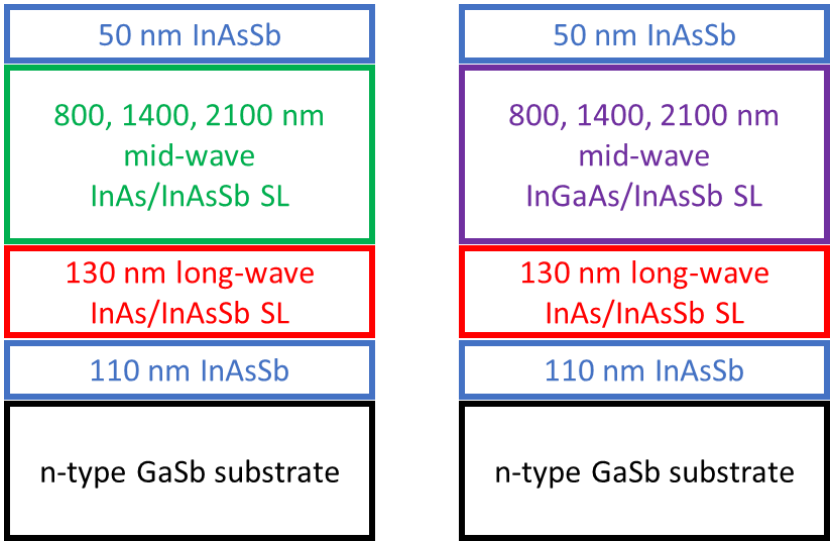

Figure 56. Sample cross sections of InAs/InAsSb and InGaAs/InAssb mid-wave superlattices grown on long-wave InAs/InAsSb superlattices. Each sample is grown on a GaSb substrate with a 110 nm buffer and 50 nm capping layer of lattice matched InAsSb for carrier confinement

The sample run numbers, mid-wave and long-wave superlattice material and thicknesses are provided in Table 31.

Table 31. Sample run numbers, mid-wave and long-wave superlattice material and thicknesses

Sample run number	Mid-wave SL	Long-wave SL	Mid-wave SL thickness (nm)	Long-wave SL thickness (nm)
GN2092	InAs/InAsSb	-	1000	0
GN2095	-	InAs/InAsSb	0	1000
GN2100	InGaAs/InAsSb	-	1000	0
GN2098	InAs/InAsSb	InAs/InAsSb	2100	130
GN2101	InAs/InAsSb	InAs/InAsSb	1400	130
GN2102	InAs/InAsSb	InAs/InAsSb -	800	130
GN2107	InGaAs/InAsSb	InAs/InAsSb	2100	130
GN2104	InGaAs/InAsSb	InAs/InAsSb	1400	130
GN2105	InGaAs/InAsSb	InAs/InAsSb	800	130

Time-resolved photoluminescence as a function of temperature ranging from 77 K to 300 K were measured for both mid-wave benchmark samples, GN2092 (InAs/InAsSb) and GN2100 (InGaAs/InAsSb) at Air Force Research Laboratory. The photoluminescence decay as a function of time at 77 K and the minority carrier lifetime as a function of temperature is plotted in Figure 57.

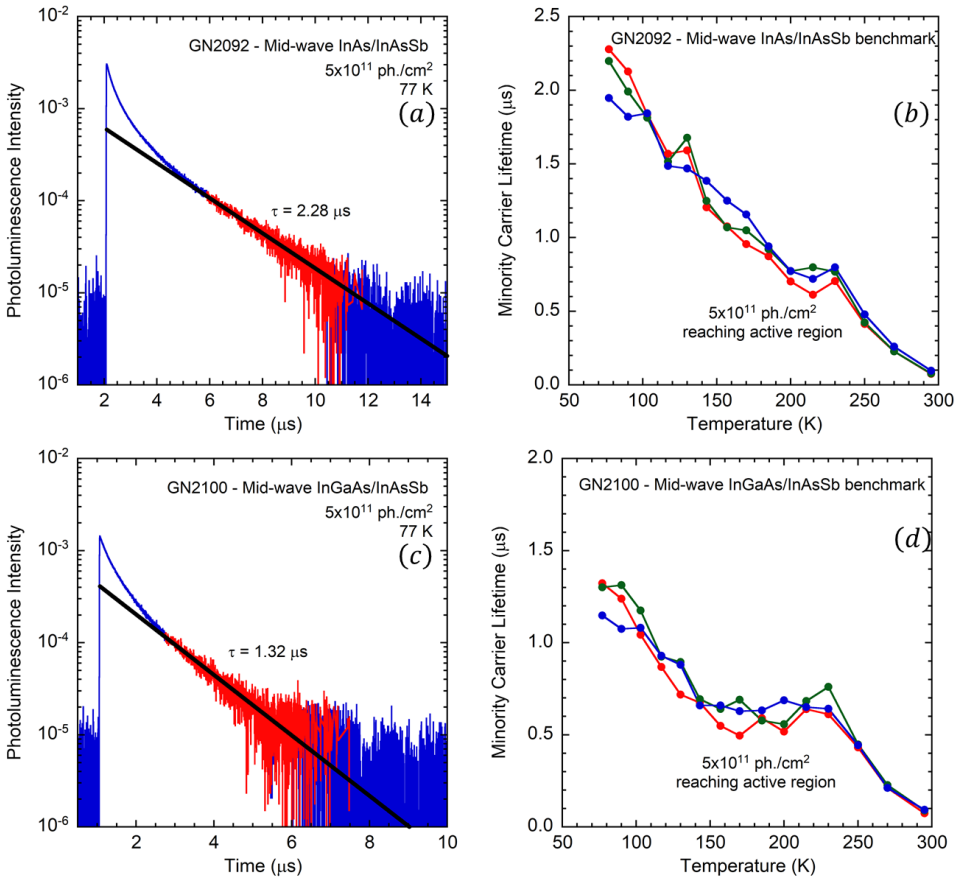

Figure 57. Photoluminescence decay as a function of time at 77 K and minority carrier lifetime as a function of temperature for the mid-wave InAs/InAsSb (a,c) and InGaAs/InAsSb (b,d) benchmark samples. A single exponential (black line) is fit to the red data from the measured photoluminescence (blue data). The lifetimes at 77 K for the InAs/InAsSb and InGaAs/InAsSb superlattices are 2.28 μs and 1.32 μs

The samples are examined using temperature-dependent photoluminescence spectroscopy. The experimental setup is identical to that described in Section (1). Photoluminescence spectra measured at temperatures ranging from 12 K to 300 K for each sample are shown in Figure 58. The mid-wave superlattices luminesce near 240 meV while the long-wave superlattices luminesce around 110 meV. For the mid and long-wave structures, the long-wave region does not begin to luminesce until higher temperatures are reached. However, as the thickness of each mid-wave region is reduced, the long-wave region begins to luminesce at cooler temperature as seen in samples GN2098, GN2101, and GN2102. The long-wave superlattice only luminesces for a short temperature range from 12K at the lowest to 125 K at the highest. Each sample was measured using an InAs reference sample, (run number B2380) which luminesces around 430 meV.

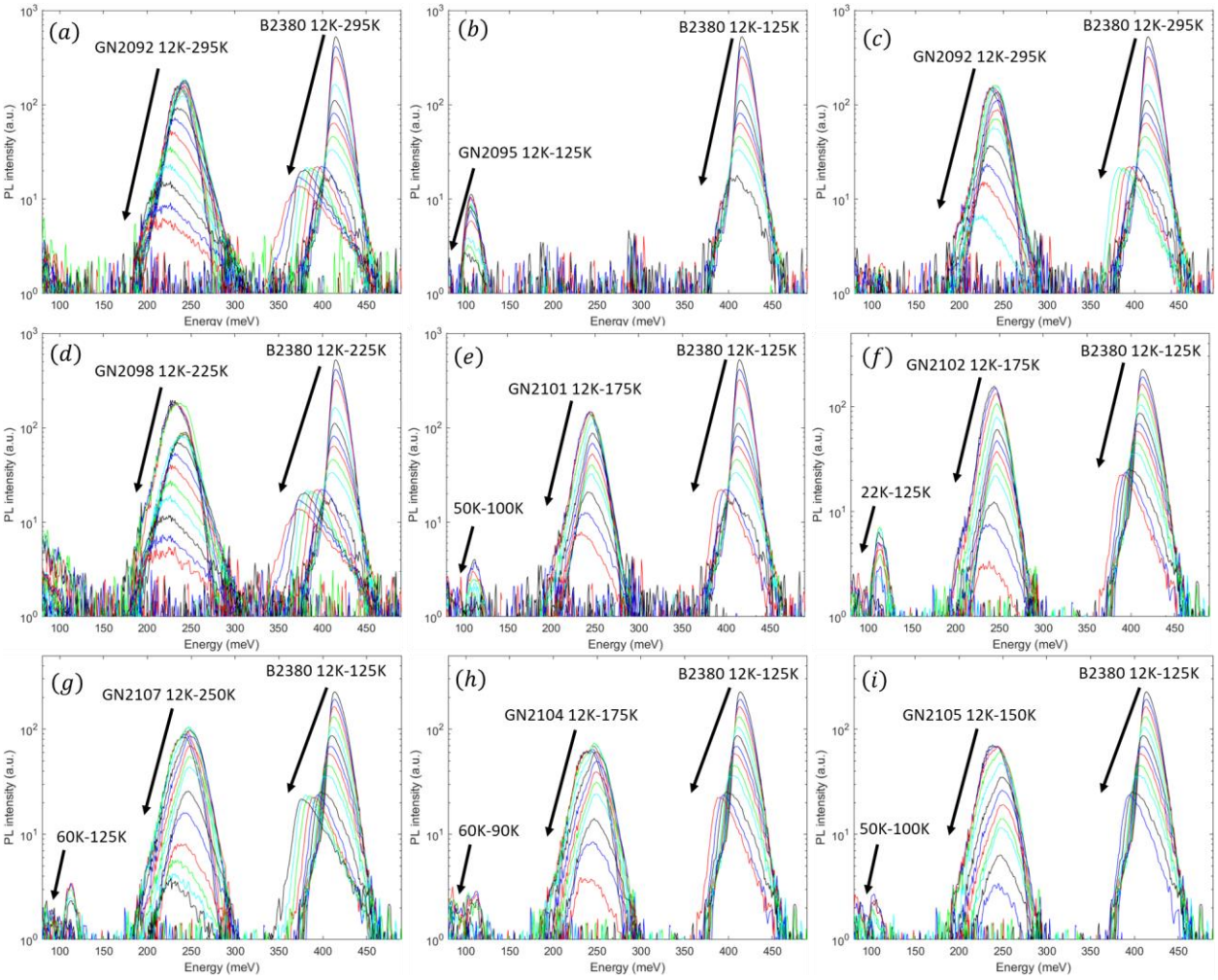

Figure 58. Photoluminescence spectra measured at temperatures ranging from 12 K to 300 K for each sample. Sample B2380 is an InAs reference sample

A diffusion model is introduced that relates the change in the excess electron-hole pairs of the mid-wave region to the long-wave region. The model consists of

$$\frac{\partial n_{MWSL}(z,t)}{\partial t} = J - \frac{n_{MWSL}(z,t)}{\tau_{MWSL}} + D_{amb}\frac{\partial^2 n_{MWSL}(z,t)}{\partial z^2} \tag{24}$$

$$\frac{\partial n_{LWSL}(t)}{\partial t} = -\frac{n_{LWSL}(t)}{\tau_{MWSL}} + D_{amb}\left|\frac{\partial n_{MWSL}(z,t)}{\partial z}\right|_{z=L} \tag{25}$$

where . $J = J_0 e^{-\alpha z}$, $J_0 = \alpha\Phi$, n_{MWSL} and n_{LWSL} are the excess electron-hole pair densities of the mid-wave and long-wave regions, respectively, τ_{MWSL} and τ_{LWSL} are the lifetimes of the mid-wave and long-wave regions, respectively, J is the carrier generation rate, J_0 is the initial peak density, α is the absorption coefficient, and Φ is the incident photon flux. Solving Eqs. (24-25) under steady state conditions, $(\frac{\partial n_{MWSL}(z,t)}{\partial t} = \frac{\partial n_{LWSL}(t)}{\partial t} = 0)$ and using the boundary conditions $\frac{dn_{MWSL}(z)}{dz}|_{z=0} = 0$; $n_{MWSL}(z)|_{z=L} = 0$ yields

$$n_{MWSL}(z) = -\frac{J_0 \tau_{MWSL} e^{-\frac{z}{L_D} - \alpha(L+z)}}{(1 + e^{\frac{2L}{L_D}})\ (L_D^2\alpha^2 - 1)}$$

$$(e^{\frac{z}{L_D}+\alpha L} + e^{\frac{2L+z+\alpha L L_D}{L_D}} - e^{\frac{L}{L_D}+\alpha z} - e^{\frac{L+2z+\alpha z L_D}{L_D}} - \alpha L_D e^{\frac{2L}{L_D}+\alpha(L+z)} + \alpha L_D e^{\frac{2z}{L_D}+\alpha(L+z)}) \quad (26)$$

and

$$n_{LWSL}(z) = \tau_{LWSL} D_{amb} \left|\frac{\partial n_{MWSL}(z)}{\partial z}\right|_{z=L}$$

$$= \frac{J_0 e^{-\alpha L} L_D \tau_{LWSL}}{1 + e^{\frac{2L}{L_D}}} \left|\frac{1 - \alpha L_D + 2\alpha L_D e^{L(\alpha+\frac{1}{L_D})} - (\alpha L_D - 1) e^{-\frac{2L}{L_D}}}{L_D^2\alpha^2 - 1}\right| \quad (27)$$

where z is the vertical length through the sample and L_D is the diffusion length. The integrated photoluminescence intensities for the mid-wave and long-wave regions are described as

$$I_{MWSL} = \int_0^L \eta_{MWSL} \frac{n_{MWSL}(z)}{\tau_{MWSL}} dz$$

$$= \frac{\eta_{MWSL} J_0 L_D e^{-\alpha L}}{\alpha\,(1 + e^{\frac{2L}{L_D}})\ (L_D^2\alpha^2 - 1)} (1 - \alpha L_D - 2\alpha^2 L_D^2 e^{L(\frac{1}{LD}+\alpha)} + e^{\frac{2L}{L_D}}(1 + \alpha L_D) + e^{\alpha L}(L_D^2\alpha^2 - 1) + e^{L(\frac{2}{LD}+\alpha)}(L_D^2\alpha^2 - 1)) \quad (28)$$

and

$$I_{LWSL} = \eta_{LWSL} D_{amb} \left|\frac{\partial n_{MWSL}(z)}{\partial z}\right|_{z=L} = \eta_{LWSL} D_{amb} \frac{J_0 e^{-\alpha L} L_D}{1 + e^{\frac{2L}{L_D}}} \left|\frac{1 - \alpha L_D + 2\alpha L_D e^{L(\alpha+\frac{1}{L_D})} - (\alpha L_D - 1) e^{-\frac{2L}{L_D}}}{L_D^2\alpha^2 - 1}\right|. \quad (29)$$

The diffusion model is described by the ratio of the integrated photoluminescence intensity of the long-wave region over the mid-wave region,

$$R = \frac{I_{LWSL}}{I_{MWSL}}. \quad (30)$$

The measured integrated photoluminescence intensity is then used to numerically solve for the diffusion length of the mid-wave superlattice. The measured integrated photoluminescence intensity for each mid-wave/long-wave structure is shown in Figure 59.

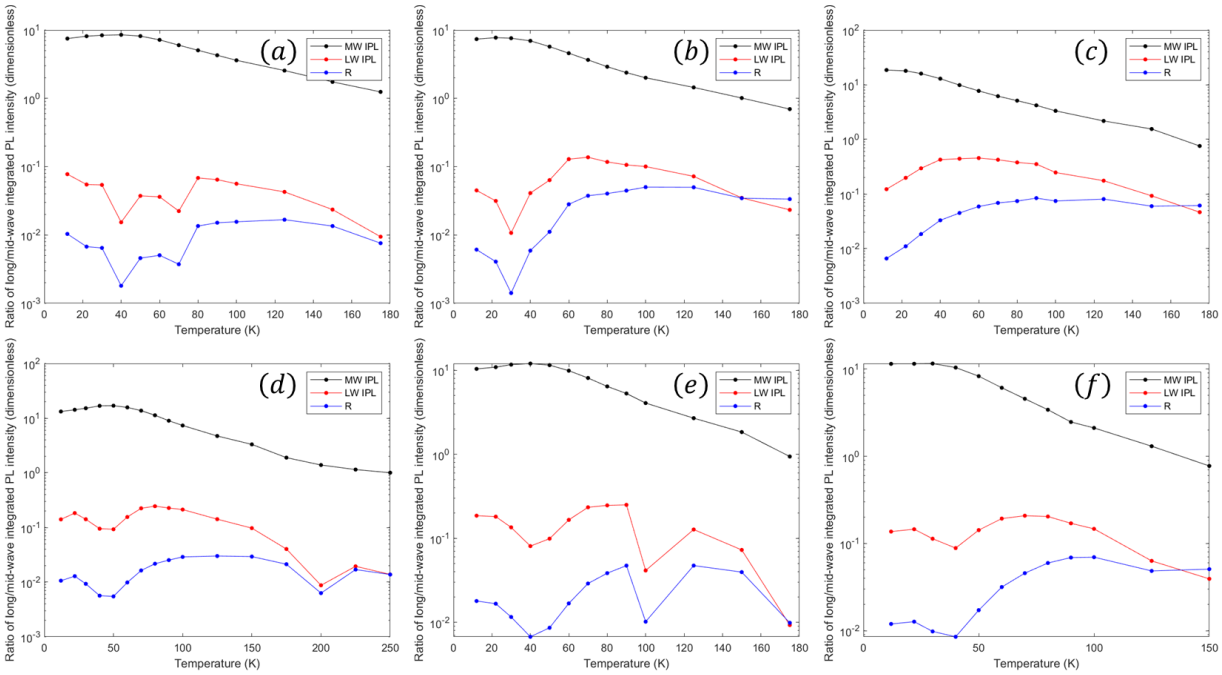

Figure 59. Integrated photoluminescence intensity of the long-wave superlattice region (red), mid-wave superlattice region (black), and the ratio of their intensities (blue) for the InAs/InAsSb and InGaAs/InAsSb mid-wave superlattices at 2100 nm, 1400 nm, and 800 nm (a-c) and (d-f), respectively

The ratio of the integrated photoluminescence intensity is used in Eq. (30) to numerically compute the diffusion length, L_D. The laser used to illuminate the samples has a wavelength of 785 nm corresponding to a photon energy of 1.58 eV. Since the superlattices are mainly comprised of InAs and their ground state transition occurs approximately 0.1 eV away from the InAs bandgap, the absorption coefficient for InAs at 1.68 eV $\alpha = 1.355 \times 10^5 cm^{-1}$ is used for the calculations. The calculated diffusion length as a function of temperature are shown in Figure 60.

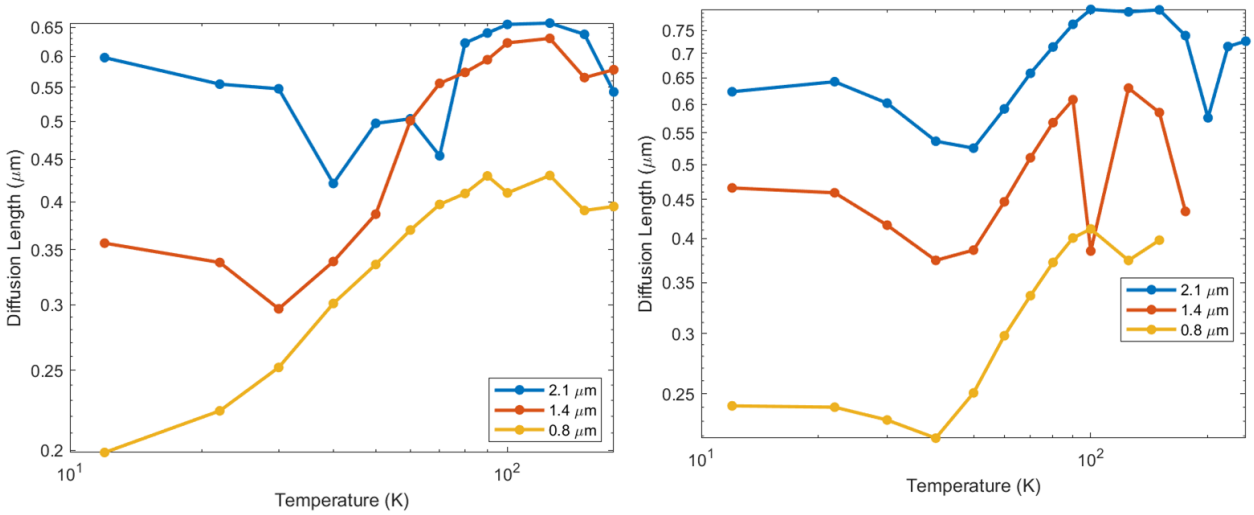

Figure 60 Calculated diffusion length as a function of temperature for the mid-wave InAs/InAsSb superlattice (left) and InGaAs/InAsSb superlattice (right) at 2100 nm, 1400 nm, and 800 nm thicknesses

It is assumed that the ambipolar diffusion is mainly dominated by hole diffusion so the following assumption is used $D_{amb} = \frac{n\mu_e D_h + p\mu_h D_e}{n\mu_e + p\mu_h} \approx D_h$, where D_{amb} is the ambipolar diffusion, n is the electron density, μ_e is the electron mobility, p is the hole density, μ_p is the hole mobility, D_e is the electron diffusion coefficient, and D_h is the hole diffusion coefficient. The hole diffusion length is related the mobility from $L_D = \sqrt{D_h \tau_{MWSL}}$. The hole mobility can then be calculated using Einstein's relation $\mu_h = \frac{D_h q}{k_B T}$. The minority carrier lifetime, average calculated mobility, and average calculated diffusion length for each mid-wave superlattice is shown in Table 32.

Table 32. Minority carrier lifetime, average calculated mobility, and average calculated diffusion length for each mid-wave superlattice

Sample	Lifetime (us)	Mobility ($\frac{cm^2}{Vs}$)	Diffusion length (um)
InAs/InAsSb	2.28	0.1	0.31
InGaAs/InAsSb	1.32	0.2	0.33

4.11 Kinetic model for molecular beam epitaxy growth of InAsSbBi alloys

The kinetic growth model presented here borrows elements from the work of Lu *et al*[15]. Lewis *et al* [16], and Tait and Millunchick [17]. Specifically these include the concepts of a weakly-bound surface layer of Bi distinct from the crystal termination layer [15,16,17], the possibility of anion exchange with Bi incorporated in the termination layer [15,17], and the accumulation of surface Bi into droplets [17]. In particular, this model of molecular beam epitaxy growth consists of six mechanisms, illustrated schematically in Figure 61. (1) Incident Bi flux physically adsorbs to the growth surface in a weakly-bound surface layer. (2) The physisorbed Bi desorbs from the surface, depleting the surface layer, or (3) chemisorbs to a group V lattice site in the crystal termination layer by forming an In-Bi bond. (4) Incident As or Sb flux displaces Bi from the crystal termination layer back into the physisorbed surface layer, breaking the In-Bi bond and replacing it with an In-As or In-Sb bond. (5) The desorption of excess As or Sb flux from the surface results in anion-assisted removal of Bi from the surface layer. Only the portion of the As or Sb flux that does not incorporate in the film is available to participate in anion-assisted removal of Bi. This stands in contrast to the model presented by Tait and Millunchick [17] which assumes that this process is proportional to the total incident As flux. Finally, (6) the coalescence of excess physisorbed Bi into Bi-rich droplet features commonly observed in bismide alloys.[1,10,11,17,18]

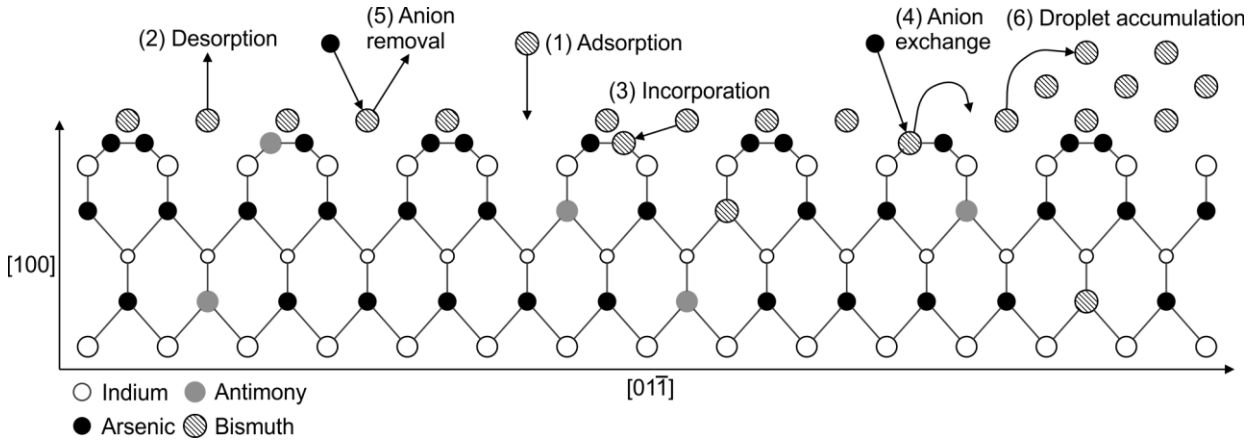

Figure 61. Schematic of (100) growth surface illustrating the six processes occurring during molecular beam epitaxy growth. (1) Adsorption of incident Bi flux into the surface layer. (2) Desorption of Bi from the surface layer. (3) Incorporation of Bi on a group V lattice site. (4) Anion exchange wherein an incident As or Sb atom displaces a Bi atom from a group V lattice site back into the adsorbed surface layer. (5) Anion-assisted removal wherein the desorption of As or Sb from the surface participates in the removal of Bi from the surface layer. (6) Accumulation of adsorbed Bi into Bi-rich surface droplets

The physisorbed Bi layer covers a fraction θ_{Bi} of the growth surface and is initially absent at the beginning of growth. It is assumed that i) all incident Bi flux physisorbs to this surface layer, ii) the Bi mole fraction in the crystal termination layer is the same as that of the bulk crystal, and iii) all processes affecting the Bi surface layer occur at its surface or interface with the crystal termination layer. A reflection of any part of the incident Bi flux without physisorption into the surface Bi layer is not distinguishable from the Bi desorption process, and is hence accounted for in that term.

In principle, the rate equations for the Bi surface coverage θ_{Bi} and Bi mole fraction can be developed for the time-dependent growth of InAsSbBi given appropriate knowledge of rates, probabilities, initial conditions, and the density of available sites in the surface layer and crystal termination layer. However these properties are generally not well characterized and the time-dependent solution of these equations is intractable except in the simplest cases. In this work the assumption of steady state growth is invoked, where the Bi surface coverage and mole fraction are constant with respect to time. Key to this assumption is that the relaxation time to achieve steady state growth is significantly less than the total InAsSbBi epilayer growth duration. The Bi surface layer coverage is thus governed by the balance between mechanisms that increase the coverage and those that reduce it, with

$$F_{Bi} + \hat{x}(F_{As}P_{exc,As} + F_{Sb}P_{exc,Sb}) = \theta_{Bi}(R_{des} + R_{inc} + R_{dro} + \Delta F_{As}P_{rem,As} + \Delta F_{Sb}P_{rem,Sb}). \quad (31)$$

The terms on the left-hand side serve to increase the Bi surface coverage. The first term, F_{Bi}, is the incident Bi flux, labeled as (1) in Figure 61. The second bracketed term is the anion-assisted exchange, labeled as (4) in Figure 61. This process is proportional to the modeled Bi mole fraction $\hat{x}$, the incident As and Sb fluxes F_{As} and F_{Sb}, and the probabilities $P_{exc,As}$ and $P_{exc,Sb}$ that an As or Sb atom displaces a Bi atom back into the surface layer.

The terms on the right-hand side scale with and serve to decrease the Bi surface coverage θ_{Bi}. The first, second, and third terms are the rates of Bi self-desorption R_{des}, Bi incorporation R_{inc}, and droplet accumulation R_{dro}, labeled as (2), (3), and (6) respectively in Figure 61. The fourth and fifth terms are anion-assisted removal of Bi by the excess As and Sb fluxes ΔF_{As} and ΔF_{Sb} and the associated probabilities $P_{rem,As}$ and $P_{rem,Sb}$, labeled as (5) in Figure 61. Excess flux is defined as the fraction of incident flux that does not incorporate.

By similar logic the modeled Bi mole fraction $\hat{x}$ in the crystal termination layer is given by the sum of the rates of the incorporation and removal processes, with

$$\hat{x}F_{In} = \theta_{Bi}R_{inc} - \hat{x}(F_{As}P_{exc,As} + F_{Sb}P_{exc,Sb}). \tag{32}$$

Where F_{In} is the In flux that is observed to (and hence assumed to) fully incorporate into the surface termination layer. The anion-assisted exchange removes Bi from the crystal termination layer into the surface layer; a process that is proportional to the density of Bi occupied group V sublattice sites and hence the Bi mole fraction. Solving the system of Eqs. 31 and 32 yields the steady state solution for the Bi surface coverage and the Bi mole fraction, with

$$\theta_{Bi} = \frac{F_{Bi}(F_{In} + F_{As}P_{exc,As} + F_{Sb}P_{exc,Sb})}{(F_{In} + F_{As}P_{exc,As} + F_{Sb}P_{exc,Sb})(R_{des} + R_{dro} + \Delta F_{As}P_{rem,As} + \Delta F_{Sb}P_{rem,Sb}) + F_{In}R_{inc}}, \tag{33}$$

$$\begin{aligned}\hat{x} &= \frac{\theta_{Bi}R_{inc}}{(F_{In} + F_{As}P_{exc,As} + F_{Sb}P_{exc,Sb})} \\ &= \frac{F_{Bi}R_{inc}}{(F_{In} + F_{As}P_{exc,As} + F_{Sb}P_{exc,Sb})(R_{des} + R_{dro} + \Delta F_{As}P_{rem,As} + \Delta F_{Sb}P_{rem,Sb}) + F_{In}R_{inc}}.\end{aligned} \tag{34}$$

Eqs. 33 and 34 constitute the model for bismuth incorporation in the molecular beam epitaxy growth of InAsSbBi. The model parameters determined by experimental measurements are the In, As, Sb, and Bi fluxes (F_{In}, F_{As}, F_{Sb}, and F_{Bi}), the excess As and Sb fluxes (ΔF_{As} and ΔF_{Sb}), and the droplet accumulation rate (R_{dro}). The model parameters determined by a best fit of Eq. 34 to experimental measurements of the Bi mole fraction are the desorption and incorporation rates (R_{des} and R_{inc}), the exchange probabilities ($P_{exc,As}$ and $P_{exc,Sb}$), and the removal probabilities ($P_{rem,As}$ and $P_{rem,Sb}$), some of which may in general depend on growth temperature. In addition, the model outputs the best fit values for the Bi surface coverage θ_{Bi} and the Bi mole fraction $\hat{x}$.

In the absence of *in-situ* measurements of the droplet evolution, it is assumed that the presence of any surface droplets accumulate at an average rate of $\theta_{Bi}R_{dro}$ during growth, with the rate of accumulation determined using *ex-situ* measurements of the surface droplets after growth. It is observed that the Bi-rich droplets do not significantly desorb or diffuse across the growth surface during the growth of the InAsSbBi layers or the subsequent capping layers or during the ramp-down of the sample to room temperature. Therefore the droplet surface coverage and associated droplet accumulation rate R_{dro} is treated as an independent variable in the analysis whose value is determined by atomic force microscopy measurements that are described below.

It is instructive to consider several limiting cases of the growth model, all subject to the assumption that the total group V/In flux ratio is greater than or equal to unity for group-III limited growth. If the probabilities of anion-assisted removal and anion exchange are zero, the Bi surface layer coverage θ_{Bi} given by Eq. 33 reduces to $F_{Bi}/(R_{des} + R_{dro} + R_{inc})$ while the Bi mole fraction $\hat{x}$ given by Eq. 34 approaches $(F_{Bi}/F_{In})\,R_{inc}/(R_{des} + R_{dro} + R_{inc})$; i.e. the Bi/In flux ratio scaled by the parallel combination of desorption, droplet uptake, and incorporation rates. Additionally, if the rates of desorption and droplet accumulation are small compared to the rate of incorporation, the Bi surface layer coverage θ_{Bi} given by Eq. 33 reduces to F_{Bi}/R_{inc} while the Bi mole fraction $\hat{x}$ given by Eq. 34 approaches F_{Bi}/F_{In}. Physically this corresponds to the case where Bi removal and exchange mechanisms are turned off, e.g. for very low temperature growth. The result is growth of an alloy with Bi mole fraction equal to the incident Bi/In flux.

If the Bi desorption rate R_{des} or anion-assisted removal rate $\Delta F_{As}P_{rem,As} + \Delta F_{Sb}P_{rem,Sb}$ is very large, e.g. for high-temperature growth or very high As and Sb fluxes, and the Bi

incorporation rate R_{inc} is very small, then both the Bi surface coverage θ_{Bi} and Bi mole fraction $\hat{x}$ approach zero.

Nearly-lattice-matched bulk InAsSbBi and InAsSb/InAsSbBi/InAsSb quantum well structures are grown by molecular beam epitaxy on ¼ 50mm (100) oriented GaSb substrates at temperatures of 400 °C and 420 °C. The sample structures are illustrated in Figure 62 with 210 nm thick bulk InAsSbBi layers shown in (a) and 10 nm thick InAsSbBi quantum wells shown in (b). The growths consist of a 500 nm GaSb buffer, a 10 nm InAs/10 nm AlSb partially strain-balanced barrier, an active region containing InAsSbBi bulk or quantum well layers, and a 10 nm AlSb/10 nm InAs barrier and cap layer. The GaSb buffer layer is grown at 500 °C except for the last 70 nm, where the substrate temperature is reduced by 80 to 100 °C in the preparation for the growth of InAsSbBi. The substrate temperature is measured using an Ircon Modline 3 (model 3G-10C05) pyrometer. The samples are grown with a constant In flux of 4.4 × 10^{14} cm^{-2} s^{-1} corresponding to an InAsSbBi on the GaSb growth rate of about 15 nm/min or 0.82 monolayers per second.[1] The In growth rate is calibrated by X-ray diffraction measurements of InAs/AlSb superlattices grown on GaSb and is maintained on an ongoing basis from measurements of bulk InAsSb and InAsSbBi growths.[1] The As/In and Sb/In fluxes are calibrated prior to each growth by growing InAs on InAs and InSb on InSb and slowly lowering the V/In flux ratio until the transition from a group V to a group III rich surface reconstruction is observed. This procedure accurately and repeatably calibrates the one-to-one V/In flux ratios for As and Sb.[1] The Bi flux is initially calibrated using scanning electron microscope measurements of the thickness of 190 nm of elemental Bi deposited on GaAs at 100 °C.[1] The Bi flux calibration is maintained on an ongoing basis by Rutherford back-scattering and x-ray diffraction measurements of InAsBi layers grown on GaSb substrates at 270 - 280 °C and near-unity As/In flux ratio, resulting in near-unity Bi incorporation coefficient.[2]

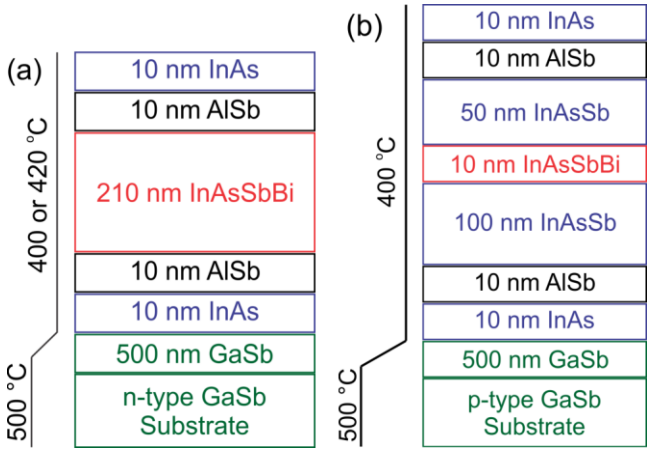

Figure 62. Sample cross sections for (a) 210 nm bulk InAsSbBi (samples A through D and H through O) and (b) 10 nm InAsSbBi quantum wells (samples E through G). The 10 nm thick compressive AlSb and tensile InAs barriers provide carrier confinement. Growth temperature profiles are shown on the left

The Bi and Sb mole fractions are ascertained from the unstrained zero-temperature bandgap measured by photoluminescence and the lattice constant measured by X-ray diffraction.[1] Symmetric $\omega - 2\theta$ X-ray diffraction scans of the (400) crystal plane and subsequent dynamical simulations yield the in-plane strain of the InAsSbBi epilayer. Assuming the layer is coherently strained (no relaxation), the tetragonal distortion of the layer and its unstrained lattice constant are calculated. This assumption is justified for the samples considered here as the in-plane strain is less than 0.18% with a corresponding Matthews-Blakeslee critical thickness[8] greater than 210 nm.

Steady state photoluminescence spectroscopy measurements yield the bandgap energy as a function of temperature in the range of 12 K to 300 K. The samples are mounted in a closed-loop He-refrigerated cryostat and optically pumped using a modulated 785 nm laser diode at an average pump power of 100 mW, providing an active layer excitation density of 36 W/cm^2.[1] The photoluminescence is collected using a Nicolet Magna-IR 760 Fourier Transform infrared spectrometer with an InSb detector with a cutoff wavelength of 5.5 μm.[1] The pump laser is modulated at 50 kHz and the detector signal is fed through a phase-locked loop amplifier for improved signal-to-noise.[1] The system optical throughput is measured and corrected using the spectrum from a Mikron M305 black body source at 800 °C.[1]

The bandgap energy is determined from the first derivative maximum of the photoluminescence spectrum, which corresponds to the energy at which the joint optical density of states increases at its greatest rate.[1,19-22] An Einstein single oscillator model is fit to the temperature-dependent bandgap energy data to determine the low-temperature bandgap energy of each InAsSbBi sample.[1,19,23,24]

The measured InAsSbBi lattice constant and low-temperature bandgap energy are related to the Bi, Sb, and As mole fractions through Vegard's Law[25] and the InAsSbBi bandgap bowing model.[1] This system of two equations is numerically solved to determine the Bi and Sb mole fractions x and y respectively, from which the As mole fraction is calculated simply as $1 - x - y$.

The standard deviation, or uncertainty, σ_i in the Bi mole fractions determined in this manner is given by the sum of uncertainty in X-ray diffraction measurements of lattice constant, σ_a, and the uncertainty in photoluminescence spectroscopy measurements of bandgap energy, σ_g, with

$$\sigma_i{}^2 = \sigma_a{}^2 + \left(\sigma_g(x_i)\right)^2, \tag{35}$$

where the lattice constant uncertainty σ_a is independent of Bi mole fraction while the bandgap energy uncertainty depends on the average Bi mole fraction x_i of the *i*-th sample. Here it is assumed that the covariance of σ_a and σ_g is zero; i.e. the X-ray diffraction and photoluminescence measurements are uncorrelated.

Seven InAsSbBi samples grown at 400 °C and the ten samples grown at 420 °C are examined and summarized in Table 33. The sample name, growth cross-section, growth temperature, incident group-V/In flux ratios, group-V mole fractions, Bi mole fraction uncertainty, and visual appearance (smooth or rough) are provided. Also shown are the excess As/In and Sb/In flux ratios, which are given by the incident flux ratio less the incorporated mole fraction. Although not directly controlled, the excess As/In flux ratio is targeted for each growth as it is observed to be a strong mediator of the incorporation of Bi and the formation of Bi-rich surface droplets. For the Sb/In and Bi/In flux ratios used here, As/In flux ratios near 0.9 result in near unity incorporation of the incident As flux, while larger values result in the presence of excess As at the growth surface. The total group-V flux is greater than unity, and in particular there is excess Sb flux present, therefore at the very least a small positive excess As flux is expected. Nevertheless, the reported excess As/In flux ratio is slightly negative for two growths, -0.2% for sample E and -0.1% for sample M. Even so, when considering the uncertainties in the mole fraction measurements and the As/In flux calibrations, these values lie in the vicinity of a small positive excess As flux.

Table 33. InAsSbBi sample cross section, growth temperature, V/In flux ratios, excess As and Sb flux ratios, group-V mole fractions, Bi mole fraction uncertainty, and visual appearance. The "Bulk" cross section is the 210 nm thick InAsSbBi layer shown in Figure 62a. The "QW" cross section is the 10 nm thick InAsSbBi quantum well shown in Figure 62b

Sample	Cross section	Growth temperature (°C)	Flux ratios			Excess flux ratios		Measured mole fractions (%)			Bi mole fraction uncertainty, σ_i (%)	Surface appearance
			Bi/In	Sb/In	As/In	As/In	Sb/In	Bi	Sb	As		
A	Bulk	400	0.05	0.120	0.940	0.036	0.029	0.58	9.06	90.36	0.21	Smooth
B	Bulk	400	0.05	0.120	0.911	0.014	0.024	0.71	9.61	89.68	0.22	Rough
C	Bulk	400	0.05	0.120	0.911	0.020	0.020	0.81	10.05	89.14	0.22	Rough
D	Bulk	400	0.05	0.105	0.911	0.006	0.016	0.58	8.92	90.50	0.21	Rough
E	QW	400	0.10	0.100	0.911	-0.002	0.032	1.86	6.85	91.29	0.31	Smooth
F	QW	400	0.10	0.100	0.911	0.009	0.018	1.67	8.17	90.16	0.31	Smooth
G	QW	400	0.10	0.100	0.911	0.014	0.011	1.35	8.90	89.75	0.31	Smooth
H	Bulk	420	0.05	0.120	0.940	0.040	0.023	0.29	9.70	90.01	0.18	Smooth
I	Bulk	420	0.05	0.120	0.940	0.036	0.026	0.22	9.42	90.36	0.17	Smooth
J	Bulk	420	0.05	0.120	0.930	0.027	0.025	0.21	9.48	90.31	0.17	Smooth
K	Bulk	420	0.05	0.120	0.920	0.017	0.025	0.20	9.46	90.34	0.17	Smooth
L	Bulk	420	0.05	0.120	0.910	0.010	0.023	0.23	9.74	90.03	0.18	Smooth
M	Bulk	420	0.05	0.120	0.900	-0.001	0.023	0.21	9.67	90.12	0.17	Rough
N	Bulk	420	0.05	0.080	0.977	0.043	0.015	0.12	6.48	93.40	0.16	Smooth
O	Bulk	420	0.05	0.080	0.947	0.011	0.018	0.20	6.18	93.62	0.17	Rough
P	Bulk	420	0.10	0.080	0.977	0.043	0.017	0.29	6.28	93.43	0.18	Smooth
Q	Bulk	420	0.20	0.080	0.947	0.012	0.018	0.33	6.18	93.49	0.19	Rough

The Bi-rich droplet surface coverage is measured by Nomarski optical microscopy using an Olympus MX50 optical microscope with Nomarski prism, analyzer, and polarizer components. The Nomarski images indicate that 400 °C grown samples B, C, D, and 420 °C grown samples M, O, and Q exhibit significant droplet coverage, while the remaining samples are essentially droplet-free, in agreement with the visual classification of samples as either specular or rough in Table 33.

The six droplet-covered samples are investigated further using atomic force microscopy (AFM) to determine the total amount of Bi, N_{Bi}, accumulated in droplet features. The measurements are performed using a Brucker multimode 8 with a lateral scan range of 153 μm and vertical scan range of 5.5 μm. Typical images are displayed in Figure 63 for samples B and M. The images are 100 μm by 100 μm and are captured using ScanAsyst-AIR tips in the Bruker ScanAsyst-in-air imaging mode. The droplet morphology varies between samples with large droplets present on the 400 °C grown samples and small, sparse droplets on the 420 °C grown samples.

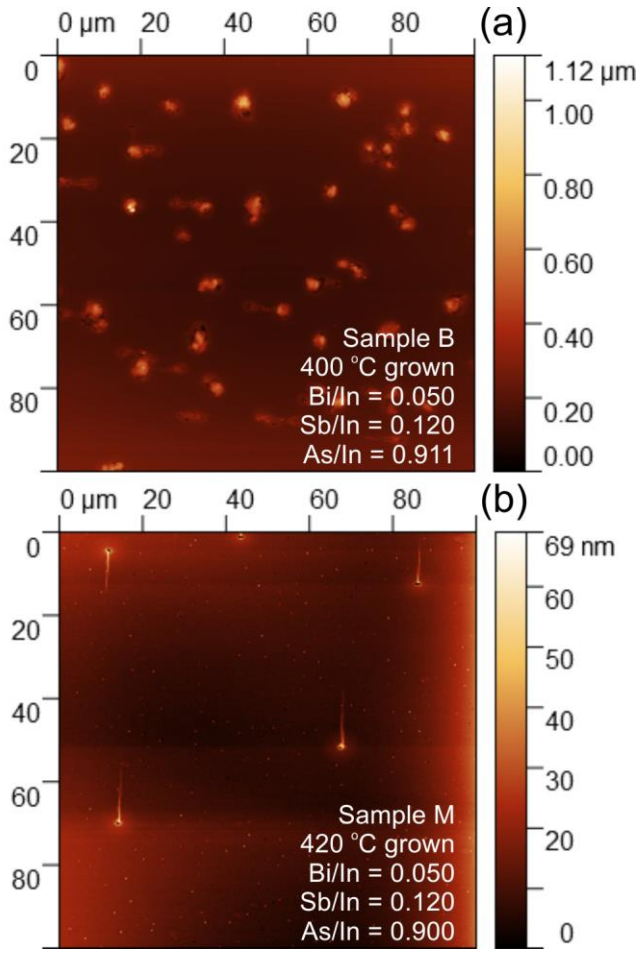

Figure 63. Unprocessed 100 µm by 100 µm atomic force microscopy images of (a) 400 °C grown sample B and (b) 420 °C grown sample M. Large, dense droplets are observed on the 400 °C grown samples B, C, and D. By contrast droplets on 420 °C grown sample M are small and sparse with a streaky morphology

The measured images are flattened and corrected for probe streaking using the Gwyddion[26] image analysis software. This process converts the surface of the unprocessed image into a uniform plane on which the droplet features reside. The droplet features are then masked using simple height thresholding. The height threshold is 35 nm for 400 °C grown samples B, C, and D, while the threshold height varies from 4.0 to 10 nm for the 420 °C grown samples M, O, and Q. The volume contained within the masked droplets is then calculated in the Gwyddion software using a Laplacian background basis.[26] Dividing the total droplet volume by the image area of 10^4 µm^2 yields the volume per unit area, $h_{droplet}$, contained within the droplet features. Table 34 summarizes the key droplet coverage statistics from AFM measurements.

Table 34 Key droplet coverage statistics from atomic force microscopy (AFM) analysis, including density, average area of a single droplet, fraction of surface covered by droplets, and volume per unit area contained by droplets. Only the bulk InAsSbBi samples which exhibit significant roughness under Nomarski optical microscopy are shown. The remaining samples are specular and do not exhibit droplet features

Sample	Growth temperature (°C)	Droplet density (cm^{-2})	Average droplet area (μm^{-2})	Droplet surface coverage (%)	Droplet volume/unit area (nm)
B	400	1.04×10^6	7.79	8.10	8.59
C	400	1.19×10^6	10.58	12.59	10.24
D	400	1.88×10^6	6.69	12.58	10.02
M	420	3.72×10^6	0.10	0.37	0.05
O	420	1.95×10^7	0.11	2.18	0.08
Q	420	1.11×10^7	0.09	1.04	0.08

The droplets are hypothesized to be composed of a mixture of metallic Bi and In. Evidence to support this can be found in transmission electron microscopy (TEM) studies of sub-micron size droplets on InAsSbBi which were found to be composed of Bi, In, and Sb.[11] Under the growth conditions examined in this work, where Sb incorporates with a nearly uniform incorporation coefficient of 80% across all samples, Sb is not expected to accumulate in the droplets in significant amounts. TEM images indicate that the InAsSbBi layer thickness in the 400 °C grown samples is 7 – 14 nm smaller than the target 210 nm thickness. This thickness difference, h_{diff}, is due to metallic In accumulation in the droplet features, since group III elements including In do not desorb from the surface during MBE growth[27,28] due to their low vapor pressure.[29] The total amount of In per unit area, N_{In}, accumulated in the droplets is calculated directly from the thickness difference. The corresponding amount of metallic Bi per unit area, N_{Bi}, contained within the droplets is given from difference between the total volume per unit area of droplet features, $h_{droplet}$, from Table 34 and the metallic In volume per unit area, h_{In}. Finally, the rate of Bi accumulation in droplets, R_{dro}, normalized to the In flux is determined by dividing the amount of metallic Bi per unit area by the total amount of In incident on the surface during growth. Table 35 summarizes the InAsSbBi layer thickness, volume per unit area of metallic In and Bi, the total amount of In and Bi per unit area, and the Bi droplet uptake rate.

Table 35. Bulk InAsSbBi layer thickness, volume per unit area of metallic In and Bi, total atomic density contained within droplet features, and Bi droplet accumulation rate for the six droplet-covered samples. Indium is present in the droplets on the 400 °C grown samples only. The droplets are assumed to be composed entirely of metallic Bi for the 420 °C grown samples

Sample	Growth temperature (°C)	InAsSbBi layer thickness (nm)			Volume/unit area (nm)		Total atomic density in droplets (cm^{-2})		Bi droplet accumulation rate, R_{dro}
		Target	TEM	Difference, h_{diff}	In, h_{In}	Bi, h_{Bi}	In, N_{In}	Bi, N_{Bi}	
B	400	210	203	7	3.22	5.37	1.23×10^{16}	1.51×10^{16}	4.10×10^{-2}
C	400	210	196	14	6.42	3.82	2.46×10^{16}	1.08×10^{16}	2.91×10^{-2}
D	400	210	198	12	5.52	4.50	2.12×10^{16}	1.27×10^{16}	3.43×10^{-2}
M	420	210	-	-	-	0.05	-	1.27×10^{14}	3.43×10^{-4}
O	420	210	-	-	-	0.08	-	2.23×10^{14}	6.02×10^{-4}
Q	420	210	-	-	-	0.08	-	2.28×10^{14}	6.17×10^{-4}

The inputs to the steady state kinetic growth model embodied by Eqs. 33 and 34 are the growth temperature, Bi/In, Sb/In, and As/In flux ratios, and excess As/In and Sb/In flux ratios listed in Table 33 and measured droplet accumulation rate R_{dro} listed in Table 35. Without loss of generality, all fluxes and rates are normalized to the incident In flux F_{In}. The growth model parameters R_{des}, R_{inc}, $P_{exc,As}$, $P_{exc,Sb}$, $P_{rem,As}$ and $P_{rem,Sb}$ are treated as independently

adjustable parameters in the fitting algorithm so that the best fit to the measured Bi mole fractions at 400 °C and 420 °C can be achieved. Because the MBE growth rate is directly proportional to the incident group III flux,[27,28] all processes are assumed to scale with the In flux and the rates R_{des}, R_{dro}, and R_{inc} are normalized to the In flux and are dimensionless. To realize physically reasonable results, all six fitting parameters are subject to the lower and upper bounds listed in Table 36. The upper bounds on the probabilities are unity while the upper bounds on desorption, incorporation, and droplet accumulation rates are determined heuristically from published works. The Bi desorption rate is capped at unity since the rate of Bi desorption is not expected to exceed the incoming In flux. The Bi incorporation rate is capped at 1.00 since the Bi incorporation coefficient, defined as Bi mole fraction divided by Bi/In flux ratio, ranges from about 0.02 to 0.10 at these growth temperatures.[1]

Table 36. Lower and upper bounds on the six dimensionless growth model parameters

Fitting range	Rates (relative to In flux)		Probabilities			
	R_{des}	R_{inc}	$P_{exc,As}$	$P_{exc,Sb}$	$P_{rem,As}$	$P_{rem,Sb}$
Lower bound	0.00	0.00	0.00	0.00	0.00	0.00
Upper bound	1.00	1.00	1.00	1.00	1.00	1.00

The model parameters are fitted to the Bi mole fractions of the combined set of 17 samples grown at 400 °C and 420 °C. The probabilities of anion-assisted exchange and removal are not expected to be strongly temperature dependent and are fitted as constant with respect to growth temperature. On the other hand, the Bi self-desorption rate R_{des} is expected to be a strong function of temperature and therefore is allowed to vary with growth temperature in the fit. The Bi incorporation rate R_{inc} is also expected to be a strong function of temperature, however it is closely correlated with Bi self-desorption rate. For this reason it is not possible to fit the incorporation and desorption rates independently at both 400 °C and 420 °C growth temperatures. An Arrhenius temperature dependence is assumed for the Bi incorporation rate to remove the correlation in the fit:

$$R_{inc}(T) = R_{inc}(400)e^{-\frac{(T-400)}{T_c}}. \tag{36}$$

The incorporation rate at 400 °C, $R_{inc}(400)$, is a fitting parameter while the characteristic temperature of incorporation T_c = 20.56 K is obtained from Figure 5 in Ref. [1], Bi incorporation coefficient vs growth temperature. In this way the Bi incorporation rate is assumed to vary with temperature in the same manner as the Bi incorporation coefficient. At 420 °C the Bi incorporation rate is $R_{inc}(420) = 0.378 \cdot R_{inc}(400)$. A total of 7 independently adjustable parameters are thus fit to the 17 samples: $R_{des}(400)$, $R_{des}(420)$, $R_{inc}(400)$, $P_{exc,As}$, $P_{exc,Sb}$, $P_{rem,As}$, and $P_{rem,Sb}$. An analysis of fitting uncertainty and correlation is discussed in Appendix D.

Fitting to the Bi mole fraction is accomplished using the `lsqnonlin()` nonlinear least-squares fitting function in MATLAB R2020a.[9] The objective function to be minimized by `lsqnonlin()` is the squared error between measured and modeled Bi mole fractions, weighted by the variance in each measured Bi mole fraction as summarized in Table 33:

$$\chi^2 = \sum_{1}^{N} (x_i - \hat{x}_i)^2 / {\sigma_i}^2 . \tag{37}$$

Here, x_i and $\hat{x}_i$ are the measured and modeled Bi mole fractions respectively for the i-th sample.

A satisfactory fit quality is difficult to acquire as the number of fitting parameters increases. Therefore the fit options must be judiciously chosen so a good fit is achieved. The default 'Trust-region-reflective' algorithm provided by MATLAB is used as it handles bounds on the fitting parameters, unlike the 'Levenberg-Marquardt' algorithm. The fit options including limits, tolerances, and iterations are shown in Table 37.

Table 37. Fit options specified for the `lsqnonlin()` function. Fit options not listed use the default values provided in MATLAB R2020a[9]

Fit option	Value
`options.Algorithm`	`Trust-region-reflective`
`options.FiniteDifferenceType`	`central`
`options.FunctionTolerance`	`1e-6`
`options.MaxFunctionEvaluations`	`4000`
`options.MaxIterations`	`2000`
`options.OptimalityTolerance`	`1e-6`
`options.StepTolerance`	`1e-6`

Stochastic initialization is used to locate the global minimum of the fit. A set of 1000 initial conditions are randomly generated for the growth model parameters, subject to the range constraints in Table 36. The fitting algorithm is iterated for each of the 1000 sets of initial conditions and the minimized least-squared error given by Eq. 38 is evaluated. A global minimum of $\chi^2 = 5.228$ for the combined 400 °C and 420 °C sample set is identified. The best fit parameters are summarized in Table 38 below. The asymptotic standard error of the fit parameters,[30] σ_p, is also shown. The reduced χ^2 error criterion, χ_v^2, is a measure of the quality of the fit and is given by:[30]

$$\chi_v^2 = \frac{\chi^2}{m - n + 1}, \tag{38}$$

Here, $m \times n$ is the size of the Jacobian matrix,[30,31] or the number of samples times the number of fitting parameters, 17×7. Large values of the reduced χ^2 error criterion, $\chi_v^2 \gg 1$, indicate a poor fit. Conversely, small values of the reduced χ^2 error criterion, $\chi_v^2 \ll 1$, indicate the model is over-fitting the data. χ_v^2 = 0.4753 for the fit presented in Table 38, indicating the fit error is on the same order as the measurement error as desired.[30] Allowing the other model parameters to vary with growth temperature results in marginal reductions in the least-squared error, however the fitted values of the parameters vary orders of magnitude from 400 °C to 420 ° C and χ_v^2 is reduced, indicating the model is fitting to measurement noise. Therefore only the Bi desorption rate R_{des} and incorporation rate R_{inc} are allowed to vary with temperature while all other parameters are held constant, which leads to physically interpretable fit results.

Table 38. Best fit growth model parameters and their asymptotic standard errors, σ_p, for the globally minimized least-squared error on Bi mole fraction

Value ± σ_p	Rates (relative to In flux)		Probabilities			
	R_{des}	R_{inc}	$P_{exc,As}$	$P_{exc,Sb}$	$P_{rem,As}$	$P_{rem,Sb}$
400 °C growth	0.1300 ±1.977×10^{-6}	0.0512 ±1.407×10^{-5}	1.0000	2.352×10^{-12}	1.0000	1.509×10^{-11}
420 °C growth	0.3504 ±3.546×10^{-6}	0.0194 ±5.319×10^{-6}	±3.005×10^{-5}	±2.662×10^{-5}	±5.345×10^{-4}	±2.742×10^{-4}

The dimensionless growth model parameters R_{des}, R_{inc}, $P_{exc,As}$, $P_{exc,Sb}$, $P_{rem,As}$ and $P_{rem,Sb}$ listed in Table 38 are plotted in Figure 64. Solid blue circles indicate the 400 °C growth parameters while red squares indicate the 420 °C growth parameters. Black circles indicate parameters which are constant with growth temperature. It is evident that the Bi incorporation rate decreases with growth temperature while the desorption rate increases. The characteristic temperatures of the Bi desorption rate R_{des} and incorporation rate R_{inc} are 20.17 K and 20.56 K[1] respectively. The results indicate thermally-activated behavior for the Bi incorporation and droplet desorption rates, consistent with literature.[15,16,32] The characteristic temperature of the Bi desorption and incorporation rates closely track each other and the growth temperature difference of 20 K, justifying the *a priori* assumption of a characteristic temperature of incorporation of 20.56 K. The net result is smaller Bi mole fractions at the higher growth temperature, consistent with experimental growth of dilute bismide alloys including InAsSbBi,[1,2] InAsBi,[10] GaAsBi[15,16,33], and GaSbBi.[17,34] The As-assisted removal mechanism is seen to play a dominant role in Bi desorption, evident from the unity probability $P_{rem,As}$ of removal by excess As flux. With relatively high As flux and unity probability of Bi removal, the As-assisted removal mechanism is primarily responsible for reduction of excess surface Bi. Additionally, As is observed to displace Bi from the crystal termination layer with unity probability $P_{exc,As}$. By contrast the probabilities of Sb-assisted removal and exchange mechanisms are effectively zero. Therefore, the Sb flux has essentially no effect on the Bi surface coverage and Bi mole fraction.

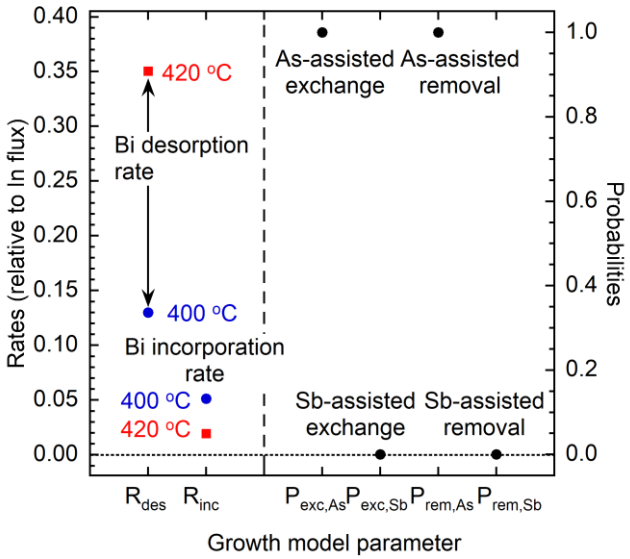

Figure 64. Best-fit growth model parameters for 400 °C (blue circles) and 420 °C (red squares) grown InAsSbBi. Black circles indicate parameters which are constant with growth temperature. Bi desorption and incorporation rates shown on the left-hand axis, and As and Sb assisted exchange and removal probabilities shown on the right-hand axis

Figure 65 shows the measured and modeled Bi mole fractions as solid circles and open squares respectively. Light error bars on the measured Bi mole fractions are the uncertainties σ_i as reported in Table 33. Heavy error bars on the modeled Bi mole fractions are the asymptotic standard errors of the fit. Bi/In, Sb/In, and As/In flux ratios for each sample are labeled directly in the figure. The measured Bi mole fractions range from 0.12% for 210 nm thick bulk InAsSbBi grown at 420 °C (sample M) to 1.86% for a 10 nm thick InAsSbBi quantum well (sample E) grown at 400 °C. The model predicted Bi mole fractions agree to within +19/-18% relative error of the measured mole fraction for 400 °C growth and to within +57/-62% relative error for 420 °C growth.

The model accurately replicates the measured Bi mole fractions to within one standard deviation σ_i of uncertainty for each InAsSbBi sample.

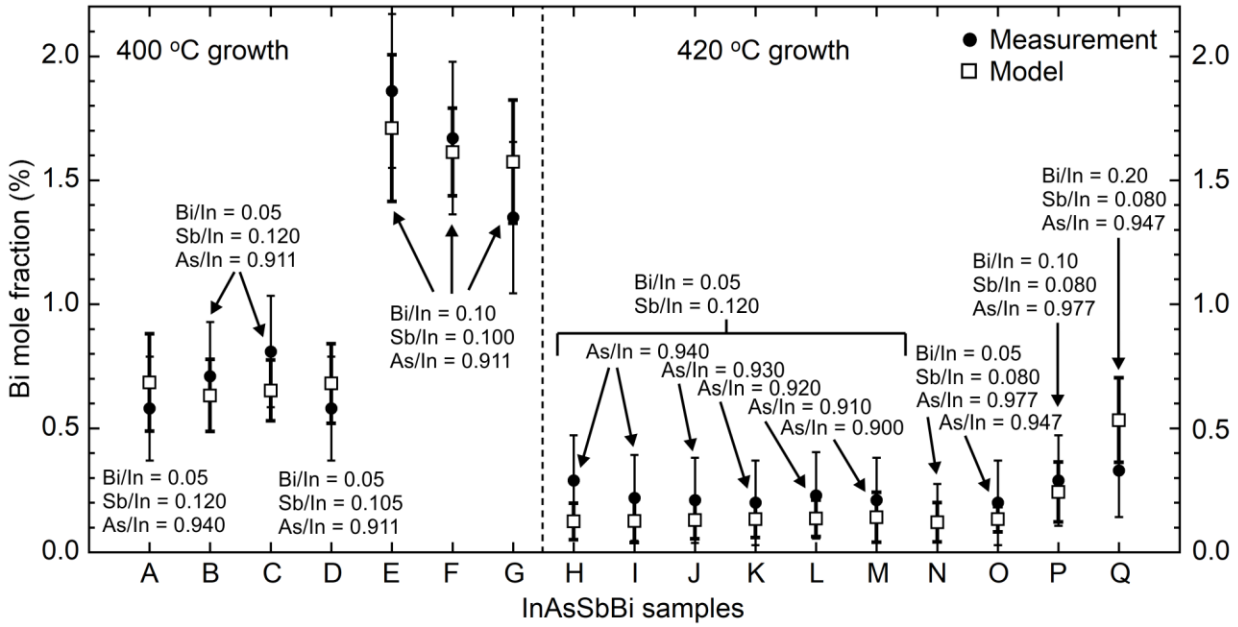

Figure 65. Measured (solid circles) and model predicted (open squares) Bi mole fractions for 400 °C and 420 °C grown InAsSbBi sample set. Light error bars on measured Bi mole fractions are the uncertainties σ_i reported in Table 33. Heavy error bars on modeled Bi mole fractions are asymptotic standard errors of the fit. Bi/In, Sb/In, and As/In flux ratios are labeled for each sample

Figure 66 shows the Bi surface coverage in steady state, θ_{Bi}, predicted by the model. The black circles indicate droplet-free specular samples and the red squares indicate droplet covered rough samples. The surface coverage is not measurable *ex-situ* and is very challenging to measure *in-situ*, but regardless the model prediction offers important insights for molecular beam epitaxy growth of bismide alloys. The surface coverage is roughly proportional to the Bi/In flux ratio for all samples. The steady state surface coverage is slightly reduced for droplet covered samples where the droplet accumulation rate R_{dr} reduces the surface coverage. A trend of increasing Bi surface coverage with decreasing As flux is evident in the 420 °C grown bulk sample series H – M, confirming the dominant role of As flux in desorbing Bi from the growth surface. The model predicts that Bi desorption, incorporation, droplet accumulation, and As- and Sb-assisted removal will all act to deplete the surface reservoir of Bi. The As-assisted exchange rate $F_{As}P_{exc,As}$ serves to replenish the Bi surface reservoir from Bi atoms in the crystal termination layer, however the net effect is a reduction in the Bi surface coverage due to the much greater contribution from the incorporation, desorption, droplet accumulation, and As-assisted removal mechanisms.

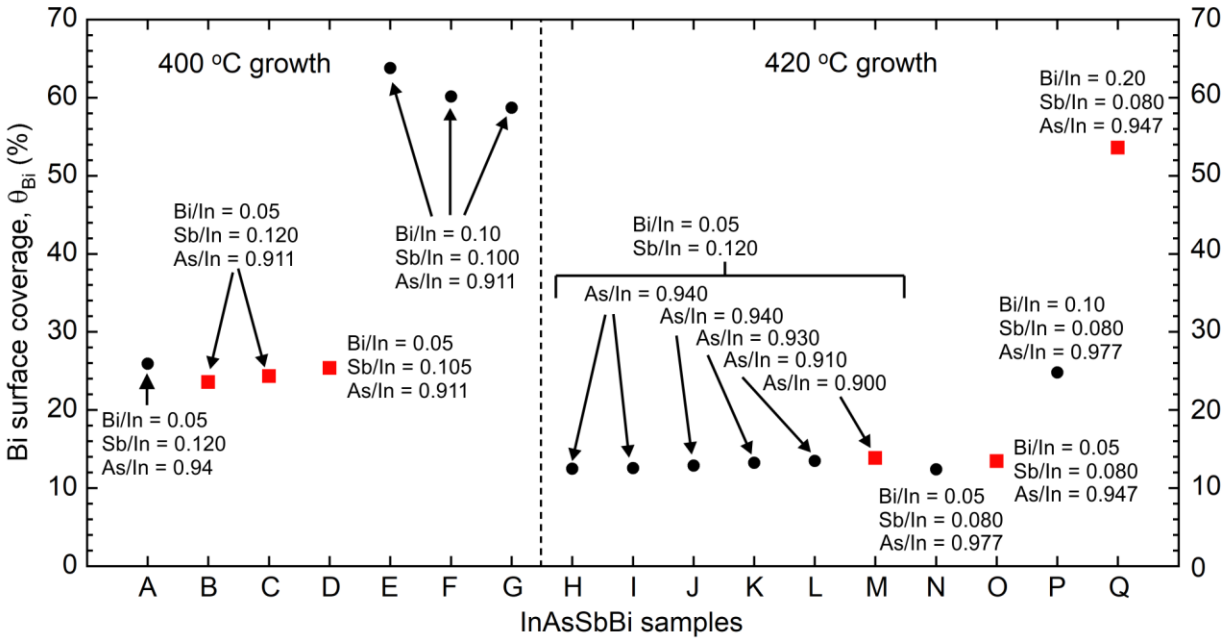

Figure 66. Model predicted Bi surface coverage θ_{Bi} for 400 °C and 420 °C grown InAsSbBi sample set. The black circles indicate droplet-free specular samples and the red squares indicate droplet covered rough samples. Bi/In, Sb/In, and As/In flux ratios are labeled for each sample

The best fit growth model parameters in Table 38 indicate that As flux plays a dominant role in Bi incorporation with effectively zero contribution from the Sb flux. The Bi mole fraction dependence on As flux is illustrated in Figure 67. The Sb/In flux ratio is held constant at 0.120 and the excess Sb/In at 0.030, typical of InAsSbBi in the 400-420 °C growth regime where the average Sb incorporation coefficient is 75%.[1] Bi mole fraction is directly proportional to the Bi/In flux ratio. Bi mole fraction decreases with increasing As flux in all cases, however the reduction in mole fraction with excess As flux in Fig 52b is much greater than the reduction with absolute As flux in Fig 52a. This is a consequence of the unity probability of As-assisted removal by excess As flux which directly reduces the Bi surface coverage. In contrast, the As-assisted exchange by the absolute As flux has a smaller and less direct effect on Bi surface coverage and thus incorporation.

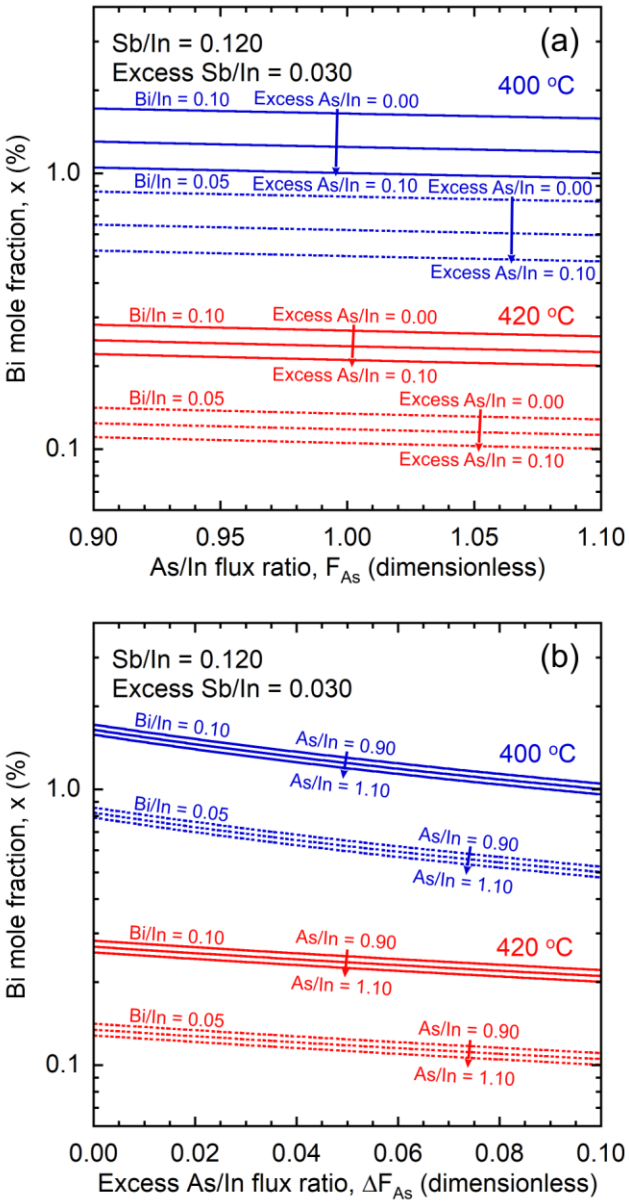

Figure 67. Model predicted Bi mole fraction as a function of (a) absolute As/In flux ratio with excess As/In flux ranging from 0.00 – 0.10, and (b) excess As/In flux with absolute As/In flux ranging from 0.90 – 1.10. Sb/In flux is fixed at 0.120 with excess Sb/In of 0.030. Bi/In flux ratios of 0.05 (dashed lines) and 0.10 (solid lines) are shown for 400 °C growth (red lines) and 420 °C (blue lines)

The molecular beam growth conditions for droplet-free growth are of particular interest for materials designers. Bi-rich droplet features are generally undesirable as they are detrimental to the structural and optical properties of the material. Droplet-free growth is predicted if the droplet accumulation rate R_{dro} is set to zero in the model and the steady state Bi surface coverage θ_{Bi} is maintained below unity. This can be understood from the fact that if the surface coverage increases above unity, the thickness of the Bi surface layer will begin to increase above one monolayer. Steady state conditions will not be achieved in this situation unless Bi-rich droplet accumulation occurs, thus depleting the Bi surface layer back below unity surface coverage.

The steady state growth model embodied by Eqs. 33-34 can be used to specify the molecular beam epitaxy growth conditions to grow bulk InAsSbBi with a desired composition. Figure 68

shows the As/In, Sb/In, and Bi/In flux ratios for growth of droplet-free InAsSbBi lattice matched to GaSb substrates. The Sb sticking coefficient, defined as the ratio between Sb mole fraction and Sb/In flux ratio, is assumed to be constant at 75% as in Figure 68. The shaded regions in Figure 53 indicate the ranges of As/In and Bi/In flux ratios which yield droplet-free growth. The flux ratios for the measured samples from Table 33 are shown on Figure 68 as data points, with droplet-free specular samples indicated by solid circles and droplet-covered samples indicated by open circles. It should be noted that these samples are not strictly-lattice matched, however the shift in the flux ratio contours over the experimental range of strain is negligible. As the As/In flux ratio becomes very large, so too does the Bi/In flux ratio for growth of dilute-Bi material. Physically, the model predicts that increasing As flux will increase the rate of As-assisted removal and thus can maintain a droplet-free surface under high Bi fluxes. While interesting, this result is of little practical importance for growth of high Bi content alloys.

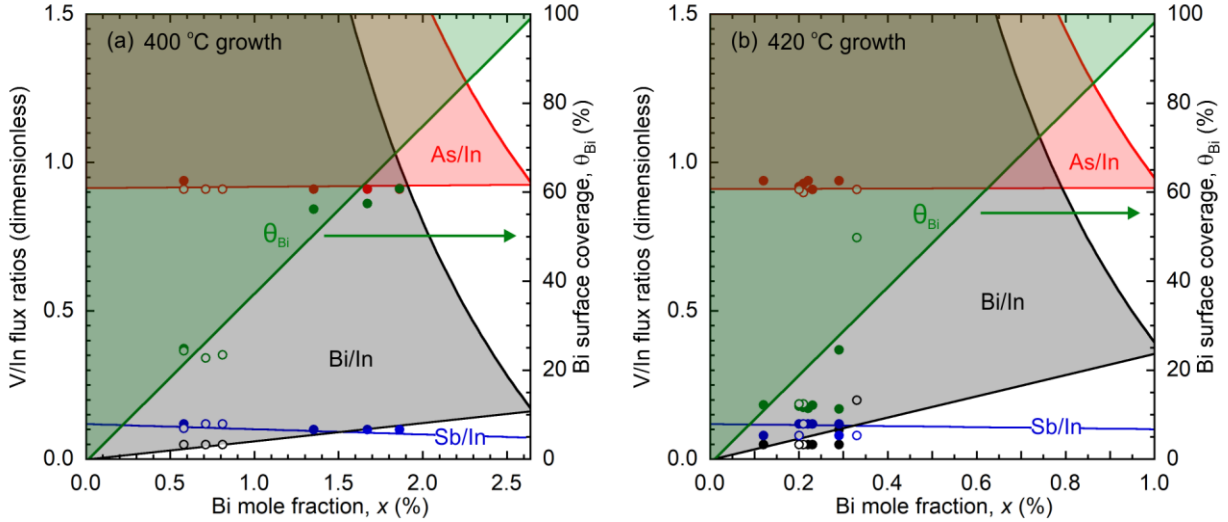

Figure 68. As/In, Sb/In, and Bi/In flux ratios for growth of droplet-free InAsSbBi lattice-matched to GaSb at (a) 400 °C and (b) 420 °C. Bi surface coverage θ_{Bi} (green) is shown on the right-hand axis and ranges from zero to 100% coverage, above which Bi-rich droplet formation occurs. Shaded regions indicate ranges of As/In (red) and Bi/In (gray) flux ratios for droplet-free growth. A maximum As/In flux ratio of 1.5 is shown, and a constant Sb incorporation coefficient of 0.75 is assumed. The flux ratios for the measured samples from Table 33 are shown as data points, with droplet-free specular samples indicated by solid circles and droplet-covered samples indicated by open circles

The lower limit of the shaded flux ratio regions indicates growth with As overpressures of zero and corresponds to the minimum amount of Bi flux required to achieve the target Bi mole fraction on the x-axis. In this case the Bi surface coverage increases linearly from zero to 100%, reaching a saturation point of approximately 2.64% and 0.99% Bi mole fraction for 400 °C and 420 °C growth respectively. Bi mole fraction is linearly proportional to the Bi surface coverage, and thus maximum Bi mole fraction is supported by unity surface coverage. Increasing Bi flux further will only result in formation of Bi-rich droplet features, while increasing As flux will deplete the Bi surface coverage and thereby reduce Bi mole fraction. The results suggest that the mole fractions 2.64% and 0.99% are the ultimate limit for droplet-free growth of InAsSbBi lattice-matched to GaSb at 400 °C and 420 °C respectively.

This ultimate Bi mole fraction limit and corresponding Bi/In, Sb/In, and As/In flux ratios for InAsSbBi lattice-matched to GaSb is plotted as a function of growth temperature in Figure 69. The Bi mole fraction exponentially decays with growth temperature as indicated by the dashed fit line and equation, with a characteristic temperature of 20.70 K. As growth temperature increases, the rate of Bi desorption increases with a characteristic temperature of 20.17 K and the rate of Bi

incorporation decreases with a characteristic temperature of 20.56 K. The probabilities of As- and Sb-assisted exchange and removal are assumed to be constant with respect to growth temperature. The resulting Bi mole fraction limit decreases with growth temperature from 6.8% at 380 °C to 0.62% at 430 °C. The required Bi/In flux ratio increases approximately exponentially from 0.135 at 380 °C to 0.573 at 430 °C. The growth model indicates that the growth temperature must be reduced to 380 °C or lower to obtain the lattice-matched endpoint ternary alloy $InAs_{0.932}Bi_{0.068}$ on GaSb, and that increases in growth temperature strongly reduce the Bi incorporation coefficient

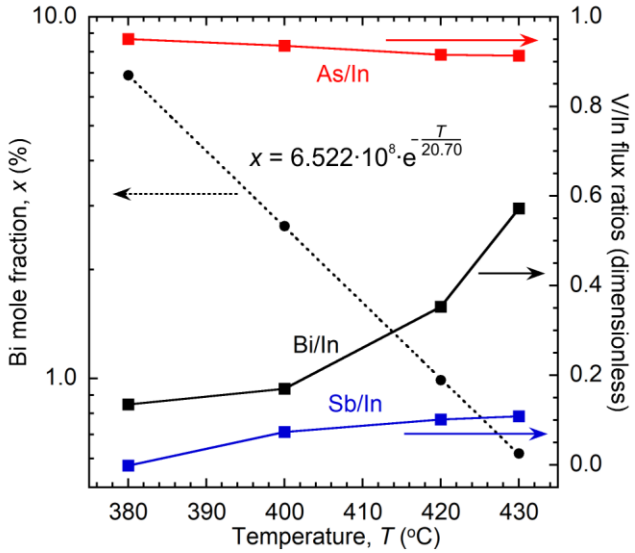

Figure 69. Ultimate Bi mole fraction limit (solid circles) and corresponding Bi/In (black squares), Sb/In (blue squares), and As/In (red squares) flux ratios as a function of growth temperature for InAsSbBi lattice-matched to GaSb. The Bi mole fraction exponentially decays with growth temperature as indicated by the dashed fit line and equation, with a characteristic temperature of 20.70 K

4.12 Absorption edge characteristics of GaAs, GaSb, InAs, and InSb

The optical absorption edge is a key property determining the optical emission spectrum in direct-bandgap III-V semiconductors. It reflects the influence of numerous properties including the joint optical density of states, the optical transition strength, and the presence of localized tail states at the band edges. Precise and repeatable measurement of the absorption edge is crucial for evaluating material quality and provides insight to the density of states and transition probabilities in the material. Specifically, these include the fundamental bandgap energy, the magnitude of the absorption coefficient at the bandgap energy, and the characteristic width of the Urbach tail that embodies the localized states near the band edges due to lattice disorder. [23,35-37]

In order to obtain these parameters from measured absorption data, analytical models of interband absorption[38-41] and empirical models of absorption edge broadening[23,25-37] have been developed to fit the intrinsic absorption edge of GaAs. Existing models typically treat interband and tail state absorption separately, which can complicate the extraction of the bandgap energy from the absorption coefficient spectrum.

The fundamental bandgap energy of a semiconductor is defined as the energy separation between the continuum valence band maximum and continuum conduction band minimum. This definition is precise in the absence of defect or tail states that cause sub-bandgap absorption. The unavoidable presence of these localized states results in a degree

of ambiguity about the determination of the bandgap energy. The bandgap energy of bulk semiconductors is at times identified as the energy at which the first derivative of the absorption coefficient α, extinction coefficient k, or imaginary part of the dielectric function ε_2 attains its maximum value.[19-22] This so-called first derivative maximum method approximates the energy at which the joint optical density of states increases at the greatest rate.[19,20] For direct-bandgap bulk semiconductors this corresponds to the onset of optical transitions involving the edges of valence and conduction band continuum states once the photon energy equals or exceeds the fundamental bandgap energy. The first derivative maximum method is also used to identify the ground state transition energy for quantum-confined structures such as quantum wells or superlattices.[20] Nevertheless, the first derivative maximum provides little insight into the shape of the absorption edge that can be strongly influenced by the Coulomb interaction[42] between the electrons and holes and the presence of localized states near the continuum band edges. These effects influence the fundamental bandgap energy as defined by the energy separation of the continuum band edges.

In its textbook form, the optical absorption spectrum of a semiconductor is expressed as a product of the joint optical density of states $\rho(h\nu)$ (cm^{-3}·eV^{-1})and a transition strength $S(h\nu)$ (cm^2·eV with[39,43]

$$\alpha(h\nu) = \rho(h\nu) \cdot S(h\nu)\,. \tag{39}$$

The joint optical density of states depends on the electron and hole density of states, which are determined by the band structure in the vicinity of the fundamental bandgap. For direct-gap semiconductors, such as III-V binaries, electrons and holes have approximately parabolic band dispersion near the band edges.[39] The corresponding joint optical density of states[39] exhibits a square root dependence on photon energy $h\nu$, with

$$\rho(h\nu) = \frac{8\sqrt{2}\pi}{h^3}\left(m_e \frac{m_c m_v}{m_c + m_v}\right)^{3/2} \sqrt{h\nu - E_g}\,. \tag{40}$$

where m_e is the free electron mass, and m_c and m_v are the dimensionless effective masses of the conduction band electrons and valence band holes, respectively.[39] In the absence of strain the light hole and heavy hole bands are degenerate at the Γ point, and the joint optical density of states is dominated by the smaller electron effective mass. Here $\rho(h\nu)$ is the density of states in the absence of band filling effects, such as the Moss-Burstein shift and bandgap renormalization.[42] These effects are negligible for measurements where the photoexcited carrier concentration is well below degeneracy.

The transition strength in Eq. 41 can be expressed in terms of a dimensionless transition strength[39,43] $S_0(h\nu)$ with

$$S(h\nu) = \frac{he^2}{4c\varepsilon_0 m_e n(h\nu)} S_0(h\nu)\,, \tag{41}$$

where h is Planck's constant, c is the speed of light, ε_0 is the vacuum permittivity, e is the electron charge, and $n(h\nu)$ is the refractive index that typically has a weak dependence on photon energy. The absorption coefficient changes by orders of magnitude in the vicinity of the band edge of the materials considered in this work, while the refractive index changes by less than 2% and as such is assumed to be an average constant value.

The transition strength S_0 describes the probability of a given optical transition and is described by the optical perturbation to the crystal Hamiltonian due to the presence of light. According to Fermi's golden rule[39] the rate of optical transitions is proportional to the perturbed Hamiltonian matrix element for interband transitions. In the long-wavelength dipole approximation where the wavelength of the perturbing optical field is much greater than the unit cell, the transition strength associated with this matrix element is equivalently related to either the momentum matrix element $\langle\psi_h|\boldsymbol{p}|\psi_e\rangle$ or dipole matrix element $\langle\psi_h|\boldsymbol{r}|\psi_e\rangle$ as [20]

$$S_0 = \left(\frac{2}{m_e}\right)\frac{|\langle\psi_h|\boldsymbol{p}|\psi_e\rangle|^2}{h\nu} = \left(\frac{8\pi^2 m_e}{h^2}\right)|\langle\psi_h|\boldsymbol{r}|\psi_e\rangle|^2 h\nu = \frac{4\pi}{h}\sqrt{|\langle\psi_h|\boldsymbol{p}|\psi_e\rangle|^2 \cdot |\langle\psi_h|\boldsymbol{r}|\psi_e\rangle|^2}\,. \quad (42)$$

In practice, either the momentum matrix element, dipole matrix element, or transition strength is assumed to be a constant that is independent of photon energy[39,44,45] in much of the analyses performed in the literature. The assumption that any one of these three is constant assumes an energy dependence for the other two. Using Eqs. 39 through 42 the absorption coefficient is expressed in terms of the momentum matrix element $\langle\psi_h|\boldsymbol{p}|\psi_e\rangle$ in Eq. 43a, the dipole matrix element $\langle\psi_h|\boldsymbol{r}|\psi_e\rangle$ in Eq. 43b, and the product of the two in Eq. 43c.

$$\alpha(h\nu) = \frac{4\sqrt{2}\pi e^2}{nc\varepsilon_0 h^2\sqrt{m_e}}\left(\frac{m_c m_v}{m_c + m_v}\right)^{3/2}|\langle\psi_h|\boldsymbol{p}|\psi_e\rangle|^2 \cdot (h\nu - E_g)^{1/2}(h\nu)^{-1} \quad (43a)$$

$$\alpha(h\nu) = \frac{16\sqrt{2}\pi^3 e^2 {m_e}^{3/2}}{nc\varepsilon_0 h^4}\left(\frac{m_c m_v}{m_c + m_v}\right)^{3/2}|\langle\psi_h|\boldsymbol{r}|\psi_e\rangle|^2 \cdot (h\nu - E_g)^{1/2} h\nu \quad (43b)$$

$$\alpha(h\nu) = \frac{8\sqrt{2}\pi^2 e^2\sqrt{m_e}}{nc\varepsilon_0 h^3}\left(\frac{m_c m_v}{m_c + m_v}\right)^{3/2}\sqrt{|\langle\psi_h|\boldsymbol{p}|\psi_e\rangle|^2 \cdot |\langle\psi_h|\boldsymbol{r}|\psi_e\rangle|^2} \cdot (h\nu - E_g)^{1/2} \quad (43c)$$

By writing the equations in this form, the photon energy dependence of each of the three assumptions is explicitly shown. In addition to the square root density states term, the constant momentum matrix element approximation results in a one over energy term, the constant dipole matrix element results in a linear energy term, and the constant transition strength approximation has no additional energy dependent term. The choice of which is taken to be constant influences the interpretation of the behavior of the absorption coefficient above the bandgap energy.

This treatment of the absorption edge considers only the continuum states involved in transitions at and above the fundamental bandgap energy and does not account for free exciton absorption,[38,42] the Coulomb enhancement of absorption near the bandgap,[40,42] or the broadening effects of thermal and frozen in crystal lattice disorder. Even high-quality materials exhibit an Urbach absorption edge[23,35-37] that is mainly due to the electron-phonon interaction. Excitonic absorption is a significant effect in high purity material, particularly at low temperatures, and results in absorption peaks below the bandgap energy.[38,40,46]

Furthermore, the Coulomb interaction between free electrons and holes results in an enhancement of absorption near the bandgap that is dependent on the free exciton binding energy[40,42,46] that typically scales with bandgap energy in the III-Vs. The Coulomb interaction is a multi-particle phenomenon involving both an electron and hole and as such cannot be treated within the free electron band structure framework, but rather requires the addition of the electron-hole Coulomb potential to the crystal Hamiltonian.[47] Thus the Coulomb interaction can modify both the density of states and the transition strength. The effect of the Coulomb interaction is large near the bandgap energy and asymptotically approaches unity at energies above the bandgap energy, which has been quantified by an enhancement factor[38,42] described as

$$F(h\nu) = \frac{2\pi\sqrt{\frac{E_{ex}}{h\nu - E_g}}}{1 - e^{-2\pi\sqrt{\frac{E_{ex}}{h\nu - E_g}}}}\,. \quad (44)$$

The exciton binding energy E_{ex} scales with bandgap energy and is experimentally determined as 4.0 meV for GaAs[40], 2.1 meV for GaSb[42], 1.0 meV for InAs[48], and 0.4 meV for InSb.[49] As such, the Coulomb enhancement of absorption is expected to increase with bandgap energy.

In this work, a model is developed that evaluates the onset of absorption at the fundamental bandgap and that encompasses the asymptotic behaviors of the absorption coefficient above and below the bandgap. The model is shown in Eq. 45 and contains 5 parameters: the bandgap energy E_g, determined by the behavior of the absorption coefficient above bandgap; the

characteristic Urbach energy E_u, based on the slope of the absorption tail below the bandgap; the magnitude of the absorption coefficient at the bandgap energy α_g; and the power law dependence $p(h\nu)$ of the absorption coefficient above the bandgap that is comprised of a constant term p_g that describes the power law at the bandgap and a photon energy $h\nu$ dependent term that describes the variation in the power law above the bandgap with characteristic energy, E_m.

$$\alpha(h\nu) = \alpha_g \left[\frac{ln\left(1 + e^{(h\nu - E_g)/pE_u}\right)}{\ln 2}\right]^p \tag{45a}$$

$$p(h\nu) = p_g + \frac{h\nu - E_g}{E_m} \tag{45b}$$

For energies above the bandgap, $h\nu > E_g$, the asymptotic behavior reflects optical absorption involving continuum states and is specified as a power law with

$$\alpha(h\nu) = \alpha_g \left(\frac{h\nu - E_g}{\ln(2) \cdot p(h\nu) \cdot E_u}\right)^{p(h\nu)} . \tag{46}$$

For energies below the bandgap, $h\nu \leq E_g$, the asymptotic behavior reflects optical absorption involving localized tail states specified by an exponential Urbach tail with

$$\alpha(h\nu) = \alpha_g (\ln 2)^{-p(h\nu)} e^{(h\nu - E_g)/E_u} \cong \alpha_g (\ln 2)^{-p_g} e^{(h\nu - E_g)/E_u} , \tag{47}$$

where the right-hand approximation is valid for abrupt absorption edges, with $E_u \ll E_m$.

Examining the absorption coefficient in terms of these model parameters provides insight into the optical joint density of states, the optical transition strength, and Coulomb enhancement of the optical transition strength. As an example, the parabolic single-electron band model predicts a square root density of states with power law one half and an Urbach tail width that approaches zero. The model in Eq. 44 does not describe bound exciton absorption peaks when present in the data, which would be modeled by an additional function.

The model is shown in Figure 70, where it is plotted in terms of normalized absorption coefficient $(\alpha/\alpha_g)(\ln 2)^p$ as a function of normalized energy $(h\nu - E_g)/E_u$. Two cases are illustrated: i) for a square root density of states and a constant transition strength, where the power law is a constant one half with p_g = 1/2 and $1/E_m$ = 0, and ii) for a strong Coulomb interaction, where the power law is small with p_g = 1/5 and $E_m = 2E_g$. The normalization $(\alpha/\alpha_g)(\ln 2)^p$ is selected such that the Urbach tail asymptotes of the two curves coincide. The power law p_g, which is related to the optical density of states and the influence of the Coulomb interaction, dictates the sharpness of the absorption turn-on at the bandgap energy. The characteristic energy E_m is related to the energy dependence of the optical transition strength (matrix element) and the decay in the strength of Coulomb interaction for optical transitions at photon energies above the bandgap.

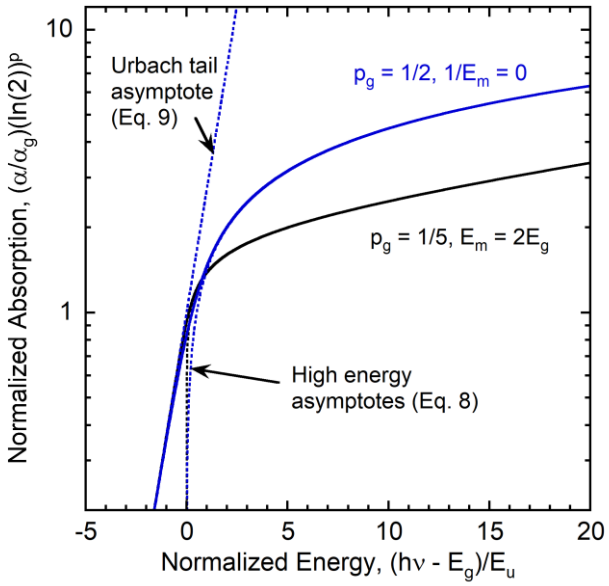

Figure 70. Normalized absorption coefficient model with $(\alpha/\alpha_g)(\ln 2)^p$ as a function of normalized energy $(h\nu - E_g)/E_u$. Dashed lines show the low and high energy asymptotic expressions, Eqs. 46 and 47 respectively

Although knowledge of the absorption coefficient at the bandgap energy is useful, it does not fully describe the overall magnitude of the absorption near the bandgap that is strongly influenced by the Coulomb interaction in addition to the density of states. For instance, the effective cutoff wavelength of a photodetector is typically shorter than the bandgap wavelength, as thin film materials can be transparent right at the bandgap. Therefore a better figure of merit for comparing the optical absorption strength of different materials for device applications is the "knee" of the absorption spectrum when viewed on a log scale, which identifies the magnitude of the absorption coefficient as it rolls over above the bandgap. The position of the absorption spectrum knee E_k is specified by the energy where the radius of curvature r_a of the absorption spectrum has a minimum value $r_k = \min_{h\nu} r_a$, with[50]

$$r_a = \left|\frac{(x'^2 + y'^2)^{3/2}}{x'y'' - y'x''}\right| = \frac{a\left(\left(\frac{1}{a}\right)^2 + \left(\frac{1}{\alpha(h\nu)}\frac{d\alpha}{dh\nu}\right)^2\right)^{3/2}}{\left|\frac{1}{\alpha(h\nu)}\frac{d^2\alpha}{dh\nu^2} - \left(\frac{1}{\alpha(h\nu)}\frac{d\alpha}{dh\nu}\right)^2\right|}. \quad (48)$$

Here, $x = h\nu/a$ and $y = ln(\alpha(h\nu)/b)$ are the dimensionless energy and absorption coefficient normalized by the constants a with units of energy and b with units of inverse length. The parameter b does not appear in Eq. 48 as the derivatives of y are independent of the vertical scale when the absorption coefficient is observed on a log scale. The parameter a scales the horizontal energy axis to the energy range of interest, as the range selected affects the observed energy position of the knee. The first and second derivatives are $x' = 1/a$, $y' = \alpha'/\alpha$, $x'' = 0$, and $y'' = \alpha''/\alpha - (\alpha'/\alpha)^2$. The radius of curvature of $\ln(\alpha(h\nu))$ exhibits a single well-defined minimum that is observed above the bandgap energy E_g, thus defining the position E_k and amplitude α_k of the knee in the absorption spectrum.

The absorption edge also manifests itself in the imaginary parts of the complex index of refraction, $\tilde{n} = n + ik$, and the complex dielectric function, $\tilde{\varepsilon} = \varepsilon_1 + i\varepsilon_2$, as is apparent in the following relationships between the optical constants.[39,51]

$$\alpha = \frac{4\pi k h\nu}{hc} \tag{49a}$$

$$\varepsilon_1 = n^2 - k^2 \tag{49b}$$

$$\varepsilon_2 = 2nk \tag{49c}$$

$$n^2 = \frac{1}{2}\left[\sqrt{\varepsilon_1^2 + \varepsilon_2^2} + \varepsilon_1\right] \tag{49d}$$

$$k^2 = \frac{1}{2}\left[\sqrt{\varepsilon_1^2 + \varepsilon_2^2} - \varepsilon_1\right] \tag{49e}$$

As such the absorption edge model in Eq. 45 is also suitable for examination of the extinction coefficient k and the imaginary dielectric coefficient ε_2.

The first derivative method of identifying bandgap energy finds the energy where the absorption edge increases at the greatest rate. Numerical calculation of the derivative at each data point is performed by the center-difference formula[52]

$$\frac{df[j]}{dh\nu[j]} = \frac{f[j+1] - f[j-1]}{h\nu[j+1] - h\nu[j-1]}. \tag{50}$$

Here, f is the measured discrete data as a function of energy, which is either the absorption coefficient α, the extinction coefficient k, or the imaginary dielectric coefficient ε_2. If the energy spacing of the data is constant, the denominator $h\nu[j+1] - h\nu[j-1]$ may be replaced by $2\Delta h\nu$, where $\Delta h\nu$ is the constant energy spacing. The center-difference point-by-point derivative calculation does not shift of the maximum of the first derivative, unlike backward or forward difference formulas that shift the derivative by $\pm\Delta h\nu$, respectively.

The fundamental absorption-edge of semi-insulating GaAs and unintentionally doped GaSb, InAs, and InSb is investigated using spectroscopic ellipsometry. The measurements are performed on commercially available III-V wafers.[53] The material specifications for resistivity, Hall mobility, and carrier concentration supplied by the manufacturer are summarized in Table 39. The carrier concentrations are well below the conduction and valence band effective density of states N_c and N_v at room temperature.[39] Therefore the material is not degenerate and band filling effects such as the Moss-Burstein shift are negligible. The absorption measurements are performed on three separate GaAs samples A, B, and C to assess the reproducibility of the measurement technique and modeling work.

Table 39. Physical and electrical characteristics of III-V substrates studied by ellipsometry. Values obtained from wafer datasheets[24]

Material	Sample	Type	Thickness (μm)	Resistivity (Ω·cm)	Hall mobility ($cm^2V^{-1}s^{-1}$)	Carrier concentration (cm^{-3})
GaAs	A	Semi-insulating	500	2×10^8	5500	5×10^6
	B		350	2×10^8	5400	6×10^6
	C		350	2×10^8	5400	6×10^6
GaSb	-	Undoped (p-type)	500	7×10^{-2}	700	1×10^{17}
InAs	-	Undoped (n-type)	500	1×10^{-2}	2.5×10^4	2×10^{16}
InSb	-	Undoped (n-type)	640	6×10^{-2}	5.0×10^5	2×10^{14}

The spectroscopic ellipsometry measurements of GaAs and GaSb are performed using a J.A. Woollam VASE spectroscopic ellipsometer that covers 0.39 to 6.42 eV (193 to 3200 nm wavelength). Measurements of InAs and InSb are performed using a J.A. Woollam IR-VASE ellipsometer that covers 0.04 to 0.73 eV (1.7 to 30 μm). All measurements are performed at room temperature (297 K) using four incident angles (68°, 72°, 76°, and 80°) with a spectral resolution of 3.9 nm (6.3 meV for GaAs and 1.7 meV for GaSb) for the VASE measurements and 16 cm^{-1} (2.0 meV for InAs and InSb) for the IR-VASE measurements. Because the wafers are transparent below the bandgap energy, reflection from the backside of the wafer results in the collection of

spurious depolarized light at the detector. Therefore, the wafer backsides are roughened sequentially with 320 and 400 grit sandpaper to diffusely scatter the backside reflections. After backside roughening, the depolarization is less than 2%.

The WVASE software[7] is used to obtain the optical constants of III-V wafers from the measured ellipsometry parameters Ψ and Δ. The ellipsometry optical model employs two layers, a surface oxide layer and the III-V layer. The thickness of the wafers ranges from 350 to 640 μm and is treated as infinite when analyzing ellipsometry data. This assumption is justified as light that reaches the backside of the substrate is diffusely scattered. Optical constants of the oxide layers and the initial values of optical constants of the III-V substrates are provided by the WVASE software library. Since the optical constants for InSb oxide are not available, the InSb native oxide is modeled using the GaSb oxide optical constants. The best fit thickness of the oxide layers is shown in Table 40. The optical constants are determined using the wavelength-by-wavelength method of analysis, which provides the raw data that is not distorted by any mathematical modeling of the optical constants. The Kramers-Kronig consistency of the optical constants is verified by repeating the fits using a generalized oscillator (PSM0: Psemi-M0) model; the optical constants derived from the wavelength-by-wavelength fitting and generalized oscillator model agree to within less than 1% over the entire wavelength range.

Table 40. Oxide layer thickness for ellipsometry models of III-V wafers

Material	GaAs			GaSb	InAs	InSb
Sample	A	B	C			
Oxide thickness (nm)	2.015	1.814	2.100	6.475	3.457	2.473

The measured absorption spectra for semi-insulating GaAs sample A and undoped GaSb, InAs, and InSb are presented in Figure 71 as a function of photon energy less bandgap energy, which aligns the absorption edges for comparison. The absorption model in Eq. 45 (solid curve) is fit to the absorption data (solid circles). The fit range is from 140 meV above the bandgap down to an extinction coefficient of $k = \alpha hc/(4\pi h\nu)$ = 0.014 below the bandgap, which is the sensitivity limit of the ellipsometric measurement. The least squares fit analysis assumes that the uncertainty in the value of each data point is proportional to its value, which results in a proportionally weighted fit to the entire data set. The results are highly reproducible with a standard deviation of 0.2 meV in the measured bandgap energy for the three GaAs samples. The best fit values for parameters α_g, E_g, E_u, p_g, and E_m are summarized in Table 41, along with the absorption coefficient knee values E_k and α_k identified from the minimum of radius of curvature for $a = 0.100$ eV; see Eq. 48. The energy scaling parameter a is selected at 40% of the full-scale range of -0.05 to 0.20 eV in Figure 71 to coincide with the visual roll-over point observed on this energy scale. The values in Table 41 are reported to the significant level of precision necessary to illustrate the reproducibility of the GaAs measurements and to accurately reproduce the model parameters and curves.

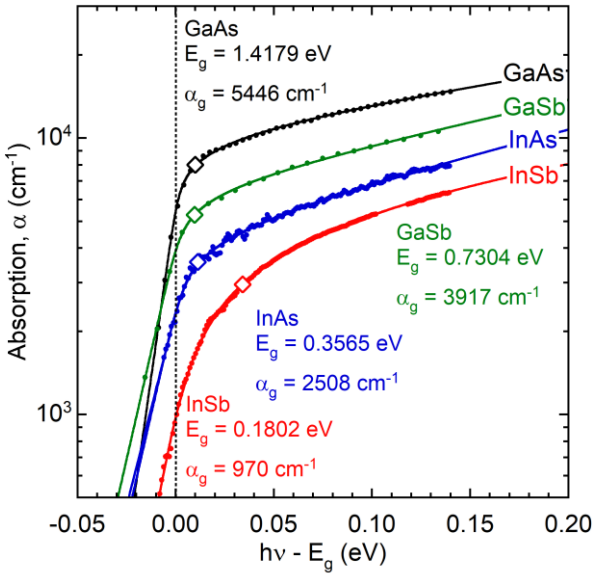

Figure 71. Absorption coefficient α as a function of photon energy relative to the bandgap $h\nu - E_g$ for semi-insulating GaAs sample A and undoped GaSb, InAs, and InSb substrates. Measured data shown as solid circles. The solid lines are fits of the absorption model in Eq. 45 to the data. The best fit parameters for bandgap energy E_g and absorption coefficient α_g are shown for each curve. The position of the knee in the spectrum is indicated by the open diamonds

Table 41. Best fit parameters for the absorption coefficient model (Eq. 45) and the absorption coefficient knee (Eq. 48) for semi-insulating GaAs, samples A, B, and C, and undoped GaSb, InAs, and InSb

	GaAs			GaSb	InAs	InSb
	A	B	C			
α_g (cm^{-1})	5446	5427	5480	3917	2508	970
E_g (eV)	1.4179	1.4177	1.4183	0.7304	0.3565	0.1802
E_u (meV)	8.69	8.66	8.74	13.98	14.05	10.67
p_g	0.1580	0.1583	0.1584	0.1613	0.1929	0.4948
E_m (eV)	2.541	2.472	2.529	1.501	1.190	4.332
E_k (eV)	1.4279	1.4277	1.4283	0.7401	0.3677	0.2142
α_k (cm^{-1})	8014	7921	7990	5286	3568	2958

The optical constants n and k, and ε_1 and ε_2, are shown for the three semi-insulating GaAs samples in Figure 72. The first derivative maxima of k and ε_2, and the maxima of the n and ε_1, are shown by vertical lines and indicated numerically. The location of the maxima is precisely determined by interpolating the data in the region of the peak with a Gaussian function, where the peak location is given by the best fit value. Detailed sensitivity analysis shows that the resulting precision of the discrete numerical calculation of the first derivative maximum is better than 0.02 meV.

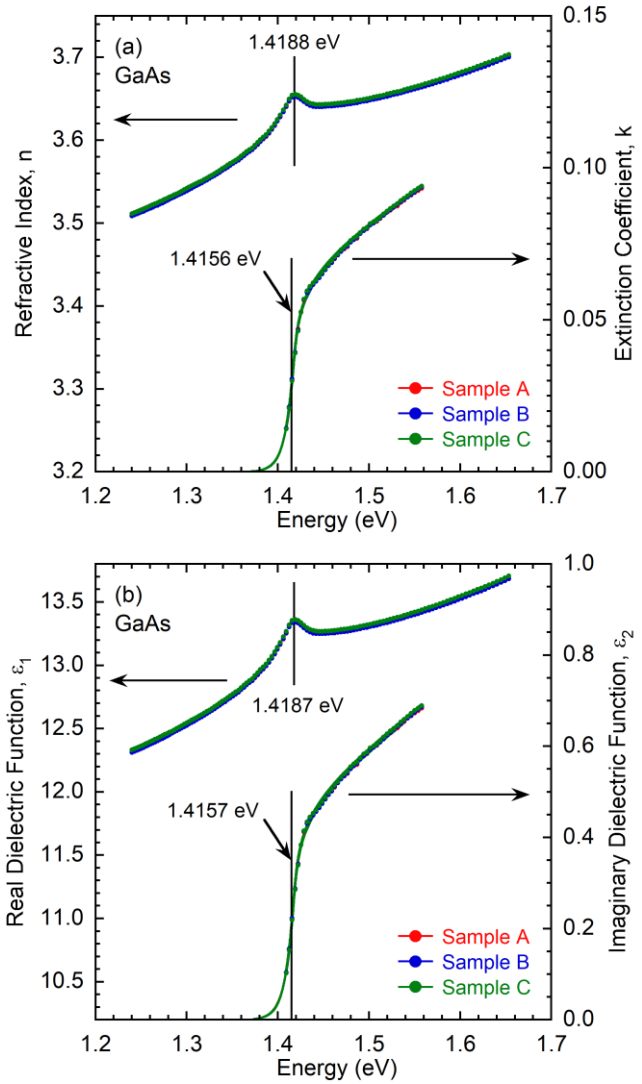

Figure 72. (a) Complex index of refraction and (b) complex dielectric function for three different semi-insulating GaAs samples measured by spectroscopic ellipsometry. The peak value of the real parts n and ε_1, and the first derivative maximum of the imaginary parts k and ε_2, are indicated by vertical lines. The solid curves are fits of the model in Eq. 45 to the k and ε_2 data over the photon energy range 140 meV above the bandgap down to an extinction coefficient of k = 0.014 below the bandgap (1.4091 – 1.5579 eV)

The GaAs bandgap energy estimated by i) fitting the absorption model in Eq. 45 to α, k, and ε_2, ii) finding the first derivative maximum[19-22] of α, k, and ε_2, and iii) finding the peak values[54] of n and ε_1 are shown in Table 42. There is excellent agreement between the three GaAs samples with the average and standard deviation of the values of the three samples shown in the right-hand column.

Table 42. GaAs bandgap energy determined by first derivative maximum of extinction coefficient k, absorption coefficient α, and imaginary dielectric function ε_2. Also shown are bandgap energies determined from the maximum values of refractive index n and real dielectric function ε_1. The model parameters for α, k, and ε_2 are summarized for each GaAs sample in the lower portion of the table. The model fits are performed over the same photon energy range as in Figure 71

	Sample A (eV)	Sample B (eV)	Sample C (eV)	Average ± Standard Deviation (eV)
maximum of 1st derivative of ε_2	1.4157	1.4156	1.4158	1.4157 ± 0.00008
maximum of 1st derivative of k	1.4157	1.4156	1.4158	1.4157 ± 0.00008
maximum of 1st derivative of α	1.4156	1.4155	1.4157	1.4156 ± 0.00008
maximum of ε_1	1.4187	1.4186	1.4188	1.4187 ± 0.00012
maximum of n	1.4188	1.4186	1.4189	1.4188 ± 0.00012
absorption coefficient α fit to model	Sample A	Sample B	Sample C	Average ± Standard Deviation
Amplitude α_g (cm^{-1})	5446	5427	5480	5451 ± 22
E_g (eV)	1.4179	1.4177	1.4183	1.4180 ± 0.0002
E_u (meV)	8.69	8.66	8.74	8.70 ± 0.03
p_g	0.1580	0.1583	0.1584	0.1582 ± 0.0002
E_m (eV)	2.54	2.47	2.53	2.51 ± 0.03
extinction coefficient k fit to model	Sample A	Sample B	Sample C	Average ± Standard Deviation
Amplitude k_g	0.0383	0.0380	0.0384	0.0382 ± 0.0002
E_g (eV)	1.4181	1.4180	1.4183	1.4181 ± 0.0001
E_u (meV)	8.81	8.75	8.84	8.80 ± 0.04
p_g	0.1500	0.1507	0.1507	0.1505 ± 0.0003
E_m (eV)	3.91	3.76	3.89	3.85 ± 0.07
imaginary dielectric function ε_2 fit to model	Sample A	Sample B	Sample C	Average ± Standard Deviation
Amplitude $\varepsilon_{2,g}$	0.280	0.278	0.281	0.280 ± 0.001
E_g (eV)	0.14181	0.14180	0.14183	1.4181 ± 0.0001
E_u (meV)	8.79	8.72	8.82	8.78 ± 0.04
p_g	0.1478	0.1485	0.1485	0.1483 ± 0.0003
E_m (eV)	3.62	3.50	3.61	3.58 ± 0.06

Agreement is observed for the best fit model (Eq. 45) parameters for the bandgap energy E_g and the Urbach energy E_u obtained from the three optical constants α, k, and ε_2. Agreement is also observed for the first derivative maximum obtained from the three optical constants α, k, and ε_2, although the first derivative maximum values are about 2 meV less than the bandgap value determined from the fit of the model to the data. The best fit power law p_g values are within 4% across the 3 sets of optical constants. The characteristic energy E_m is larger for the optical constants k and ε_2, indicating a weaker energy dependence above the bandgap compared to the absorption coefficient α, as indicated in the relations of Eq. 49 where k and ε_2 are proportional to $\alpha/h\nu$.

The absorption amplitude is observed to increase with bandgap energy and is analyzed at the bandgap energy using the product of the optical density of states, the transition strength, and the Coulomb enhancement factor in Eqs. 40, 42, and 44, where

$$\alpha_A = \lim_{h\nu \to E_g} \rho(h\nu) S(h\nu) F(h\nu) = \frac{4\sqrt{2}\pi^2 e^2 \sqrt{m_e}}{c\varepsilon_0 h^2} \cdot \sqrt{E_{ex}} \left(\frac{m_c m_v}{m_c + m_v}\right)^{3/2} \frac{S_0(E_g)}{n(E_g)}. \quad (51)$$

The exciton binding energy E_{ex} is a product of the band structure and can be expressed to first order in terms of the effective mass as[49]

$$E_{ex} = \frac{m_c m_v}{m_c + m_v} R_H / \varepsilon^2 \,, \tag{52}$$

where ε is the dimensionless static dielectric constant and $R_H = 13.6$ eV is the hydrogen Ryberg constant. The four terms on the right-hand side of Eq. 51 vary with bandgap energy and their values and power law relation with bandgap energy are provided in Table 43. Experimentally measured exciton binding energies from the literature are used in the calculation of Eq. 51, as the values predicted by Eq. 52 are significantly larger for the smaller bandgap materials.

Table 43. Material parameters and calculated absorption amplitude at the bandgap energy. References listed in square brackets for values obtained from the literature, the other values are from this work. The power law relation of the parameters with bandgap energy and reduced effective mass are shown in rightmost two columns

	GaAs	GaSb	InAs	InSb	Power laws vs E_g	Power laws vs $\frac{m_c m_v}{m_c+m_v}$
Measured bandgap energy E_g from Eq. 45 model fit (eV)	1.4179	0.7304	0.3552	0.1803	1	1.553
Experimental exciton binding energy E_{ex} values (meV)	4.0 [40]	2.1 [42]	1.0 [48]	0.4 [49]	1.110	1.554
Experimental static dielectric constant ε	12.9 [55]	15.7 [56]	15.2 [56]	16.8 [57]	-0.111	-0.157
Experimental reduced effective mass $\frac{m_c m_v}{m_c+m_v}$	0.0595 [40]	0.0364 [58]	0.0245 [59]	0.0131 [60]	0.717	1
Optical density of states effective mass $(\frac{m_c m_v}{m_c+m_v})^{3/2}$	0.0145 [40]	0.0069 [58]	0.0038 [59]	0.0015 [60]	1.076	3/2
Theoretical transition strength values $S_0(E_g)$	18.1 [61]	33.8 [61]	60.0 [61]	134.8 [61]	-0.950	-1.415
Measured index of refraction values $n(E_g)$	3.632	3.990	3.607	3.929	-0.019	-0.079
Momentum matrix element $\frac{2}{m_e}\lvert\langle\psi_h\lvert\boldsymbol{p}\rvert\psi_h\rangle\rvert^2$ (eV)	25.6 [61]	24.7 [61]	21.3 [61]	24.3 [61]	0.050	0.195
Calculated absorption amplitude (Eq. 51) α_A (cm^{-1})	21423	12662	9466	4830	0.693	0.956

The experimental values of the joint optical density of states effective mass, the exciton binding energy E_{ex}, and the strength of the Coulomb interaction $\sqrt{E_{ex}}$ all increase with bandgap energy with power laws 1.08, 1.11, and 0.56 respectively. The transition strength S_0 decreases with bandgap energy with power law – 0.95. The index of refraction is about 9% larger for the antimonides and does not significantly vary with bandgap energy. The momentum matrix element $(2/m_e)\lvert\langle\psi_h\lvert\boldsymbol{p}\rvert\psi_e\rangle\rvert^2$ in units of eV and the subsequent transition strength is determined from values of the matrix element P provided in Ref. 27, which are consistent with other published calculations.[62-64] The momentum matrix element at the Γ point does not significantly change with bandgap energy.

The theoretical absorption amplitude α_A (black circles) and the experimental absorption amplitudes α_g (red squares) and absorption knee α_k (blue diamonds) are compared in Figure 73 for GaAs, GaSb, InAs, and InSb. The solid curves are fits of a power law to the results for GaAs, GaSb, and InAs (solid symbols), with the best fit expressions indicating a power law near 0.6 for all three measures of absorption strength. The values for InSb (open symbols) are excluded from

the fit as the values for InSb do not consistently follow the bandgap dependence trend of the other three materials. The $k \cdot p$ perturbation method employed by E. O. Kane[65] indicates a non-parabolic nature in the InSb conduction band, however this nonparabolicity only becomes a significant correction at about 0.2 eV above the fundamental bandgap energy. The energy range analyzed in this work extends to 0.14 eV above the bandgap energy. The limited agreement between the InSb absorption amplitudes and the power law trend in Figure 73 are attributed to a much weaker Coulomb interaction that results in a poorly defined knee in the spectrum rather than InSb band nonparabolicity.

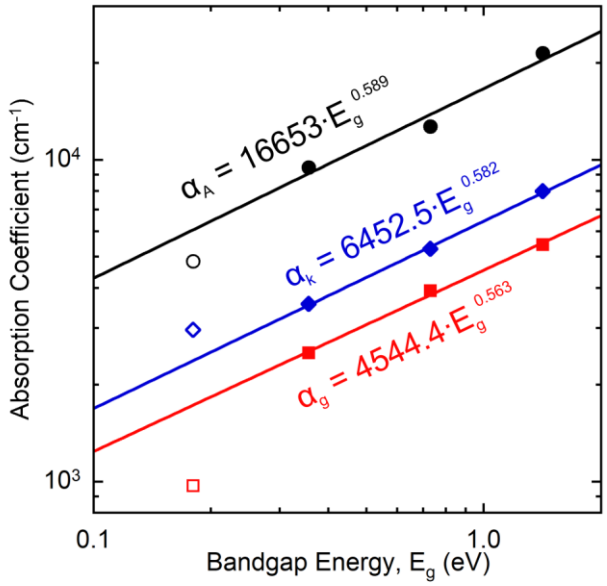

Figure 73. The calculated absorption amplitude α_A (black circles) and the experimental absorption amplitudes α_g (red squares) and absorption knee α_k (blue diamonds) are compared for GaAs, GaSb, InAs, and InSb. The solid curves are power law fits to the GaAs, GaSb, and InAs results (solid circles), with best fit expressions shown. The results for InSb (open symbols) are excluded from the fits

The Kramers-Kronig dispersion relation between the real and imaginary parts of the optical constants specifies that onset of absorption in the imaginary parts, k, or ε_2, is manifested as a peak in the real part, n or ε_1[54,66]. This small peak in the real part of the optical constants is denoted as Δn and $\Delta\varepsilon_1$ and is given by Kramers-Kronig relation[66] of the optical constants k and ε_2 evaluated over an integration range of $h\nu_1$ = 1.38 eV to $h\nu_2$ = 1.50 eV, with

$$\Delta n(h\nu) = \frac{2}{\pi}\mathcal{P}\int_{h\nu_1}^{h\nu_2} \frac{k(h\nu')h\nu'}{(h\nu')^2 - (h\nu)^2}\, dh\nu' \tag{53a}$$

$$\Delta\varepsilon_1(h\nu) = \frac{2}{\pi}\mathcal{P}\int_{h\nu_1}^{h\nu_2} \frac{\varepsilon_2(h\nu')h\nu'}{(h\nu')^2 - (h\nu)^2}\, dh\nu' \tag{53b}$$

where $\mathcal{P}$ denotes the Cauchy principal value of the integral. The integration range of 1.38 eV to 1.50 eV is selected to yield the same amplitude of Δn as in the experiment. This integration range yields an amplitude for $\Delta\varepsilon_1$ that is within 5% of the experimental value. The experimental values for Δn and $\Delta\varepsilon_1$ are obtained from the measured data by subtracting off a linear background not attributed to the fundamental absorption edge, which is $n = 2.930 + 0.469 \cdot h\nu$ and $\varepsilon_1 = 8.178 + 3.352 \cdot h\nu$ for GaAs. It is necessary to subtract the linear background as it results in a blue shift of the peak values that is not attributable to the fundamental bandgap. Decreasing the lower limit of integration below 1.38 eV has no effect on the amplitude or peak position of Δn and $\Delta\varepsilon_1$ due to the rapid decrease in optical absorption below the fundamental absorption edge. However,

increasing the upper limit of integration above 1.50 eV increases the amplitude and slightly blue-shifts the peaks in relation to the bandgap energy, which is as much as 0.9 meV for an upper integration limit of 2.50 eV. The integration range of 1.38 eV to 1.50 eV is in agreement with other analysis performed in the literature.[41]

The semi-insulating GaAs bandgap energies at 297 K determined by the various methods discussed in this work are compared in Figure 74. The values determined from the fit of the model in Eq. 45 to the measured absorption data are indicated in blue and the values determined directly from the measured data are shown in red. The optical constants examined are listed on the horizontal axis, left to right: absorption coefficient α, extinction coefficient k, imaginary dielectric coefficient ε_2, refractive index n, real dielectric coefficient ε_1, refractive index change Δn, and real dielectric coefficient change $\Delta\varepsilon_1$. Error bars indicate the standard deviation over the three samples measured. The various methods agree within a few meV of each other. The peak values of n and ε_1 are blue shifted by about 2 meV compared to the peak values of Δn and $\Delta\varepsilon_1$, which are blue shifted by about 1 meV compared to their values calculated from the Kramers-Kronig relation using both the model (blue) and the measurements (red). The bandgap energy identified by the first derivative maximum of the absorption coefficient α, extinction coefficient k, and imaginary dielectric function ε_2 is red shifted by about 1 meV using the model (blue) and by about 2 meV using the measured data (red) compared to E_g determined from the model.

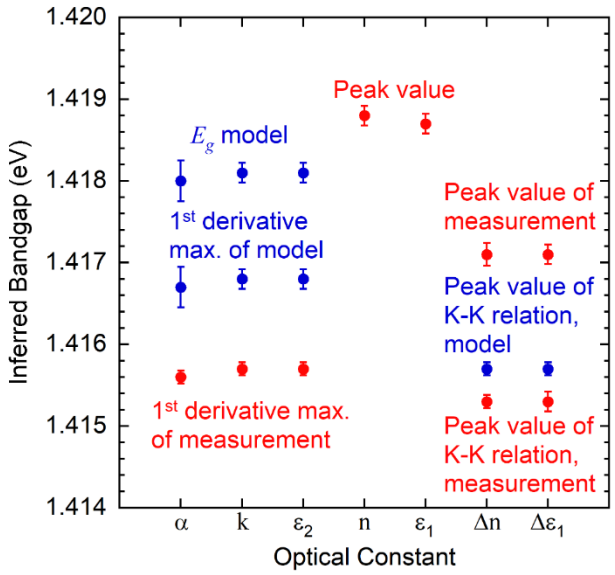

Figure 74. Comparison of GaAs bandgap energies at 297 K determined from the absorption edge model in Eq. 45 (blue circles) and the measured data (red circles) for the various optical constants and analytical methods, including the positions of peak values and 1st derivative maxima. The error bars show the standard deviation in the measurements of three GaAs samples. The horizontal-axis labels, left to right, are absorption coefficient α, extinction coefficient k, imaginary dielectric coefficient ε_2, refractive index n, real dielectric coefficient ε_1, refractive index change Δn, and real dielectric coefficient change $\Delta\varepsilon_1$

The energy position of the first derivative maximum E_p of the absorption model in Eq. 45 as a function of the power law parameter p_g is shown in Figure 75. The first derivative maximum shift relative to the model bandgap energy E_g is shown using the GaAs Urbach energy E_u = 8.70 meV, GaSb E_u = 13.98 meV, InAs E_u = 14.05 meV, InSb E_u = 10.67 meV, and a hypothetical E_u = 1.00 meV. In general the first derivative maximum of the absorption edge model does not occur exactly at the fit parameter E_g except in the specific cases where p_g is zero or 0.31 as illustrated in Figure 75. In the case where there is little exponential broadening of the absorption edge, the Urbach energy becomes small, and the first derivative maximum energy approaches the bandgap energy

E_g for all values of p_g, as illustrated by the grey curve. Relative to the bandgap parameter E_g the deviation of the first derivative maximum is less than one half of the Urbach energy E_u, and is slightly blue shifted for InSb that has a weak Coulomb interaction and is slightly red shifted for the larger bandgap III-Vs where the Coulomb interaction is more pronounced. The numerical first derivative maxima determined directly from the data for GaAs (1.4156 eV) and for GaSb (0.7272 eV) are also shown in Figure 75. The values are redshifted by approximately 1.1 meV with respect to the first derivative maximum of the absorption model.

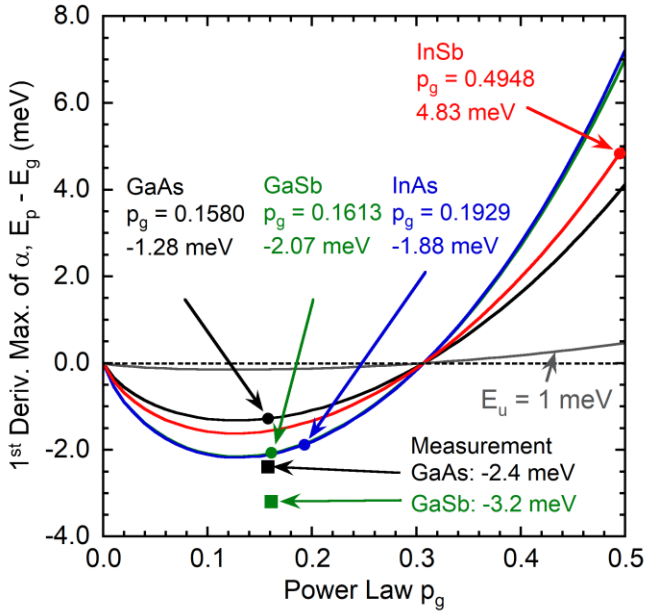

Figure 75. Comparison of the position of the first derivative maximum to the model parameter $E_p - E_g$ as a function of power law p_g for GaAs (black) with Urbach energy E_u = 8.70 meV, GaSb (green) with E_u = 13.98 meV, InAs (blue) with E_u = 14.05 meV, InSb (red) with E_u = 10.67 meV, and for E_u = 1 meV (grey). The analytical first derivative maxima of the model for each material is shown as solid circles. The numerical first derivative maxima obtained directly from the GaAs and GaSb data is shown as solid squares for comparison

The ratio of the model parameters E_m/E_g as a function of p_g is shown in red in Figure 76 for GaAs, GaSb, InAs, and InSb. The ratio of E_m/E_{ex} as a function of p_g, where E_{ex} is the exciton binding energy from Table 43, is shown in blue in Figure 76 for comparison. These results illustrate that p_g and E_m/E_g are correlated with a power law relation of about 2.2 as shown by the best fit equation in red. The absorption coefficient, bandgap energy, and exciton binding energy all scale with reduced effective mass, $m_c m_v/(m_c + m_v)$. Therefore the relation E_m/E_{ex} versus p_g exhibits a similar power law of about 2.4. The power law p_g and the ratio E_m/E_g both decrease with increasing bandgap energy, reflecting the increasing strength of the Coulomb interaction between electrons and holes. As the bandgap energy decreases, the Coulomb enhancement of absorption becomes negligible for InSb. As a result the InSb absorption coefficient behaves like that predicted for a parabolic band density of states and a constant transition strength. Larger bandgap materials exhibit reduced dielectric screening by mobile charges due to their stronger atomic potentials, and hence the Coulomb interaction is more pronounced for GaAs, GaSb, and InAs.

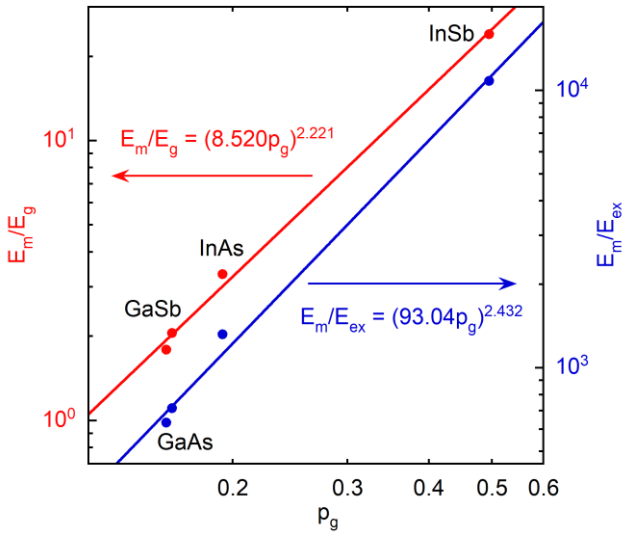

Figure 76. The ratio of the model parameters E_m/E_g (red) and E_m/E_{ex} (blue) as a function of model parameter p_g for GaAs, GaSb, InAs, and InSb. The power law relation for each is shown

The exciton binding energies in the III-V semiconductors examined in this work range from approximately 0.4 meV for InSb to 4.0 meV for GaAs, which are relatively small compared to the thermal energy of 25.6 meV at the 297 K measurement temperature. Nevertheless, an exciton absorption peak is typically observed in high-purity GaAs up to room temperature. [41,51,67-69] However, the semi-insulating GaAs measured in this work has a very short carrier lifetime due to a high density of deep-levels in the material.[70] Therefore an excitonic absorption peak is not observed in the spectroscopic ellipsometry measurements in this work, although the Coulomb interaction is clearly present in the onset of absorption of GaAs, GaSb, and InAs.

For small bandgap InSb where the Coulomb enhancement of absorption is weak, it is straightforward to interpret the model parameters p_g = 0.495 and E_m = 4.33 eV. In the absence of a Coulomb interaction, the power law reduces to the dispersion relation between energy and momentum determined by band structure near the fundamental bandgap. In the nearly free carrier approximation this yields a value of one half corresponding to a parabolic band. Furthermore, the relatively large value of the characteristic energy E_m indicates that the optical transition strength S_0 is close to constant.

The Coulomb enhancement of absorption is significant for GaAs, GaSb, and InAs and complicates the physical interpretation of the model parameters p_g and E_m. Nevertheless, they provide insight to the relative strength of Coulomb interaction and the energy dependence of transition strength. The increase in the magnitude of the Coulomb interaction with bandgap is evident from the decrease in the power law p_g as the absorption at the bandgap energy is enhanced. Furthermore, a picture emerges where the photon energy dependence of the optical transition as a function of bandgap energy is clarified. The decrease in E_m/E_{ex} with bandgap energy associated with the optical transition indicates that as the Coulomb interaction increases, the photon energy dependence changes from a constant transition strength (Eq. 43c) for small bandgap InSb to a constant dipole matrix element (Eq. 43b) for larger bandgap GaAs.

None of the experimental observations in these materials indicate that the momentum matrix element is independent of photon energy, which is expected to result in negative values for the characteristic energy E_m. However, in Table 43 the theoretical momentum matrix values at the Γ point are nearly constant across the materials examined, which is consistent with the experiment as illustrated by the similar power laws in the increase of absorption magnitude with bandgap energy observed in Figure 73. Nevertheless, the fact that the momentum matrix element is nearly

constant across bandgap energies does not necessarily imply that it should be independent of photon energy for interband optical transitions within a particular material.

A literature survey of the published values of the room-temperature (297 K) bandgap energy of GaAs finds a range of 1.422 to 1.436 eV,[67,68,71-73] with a widely accepted value of 1.424 eV.[72] The model in Eq. 45 used in this work identifies the 297 K GaAs bandgap energy at 1.418 eV, approximately 6 meV lower than the commonly-accepted value from literature. Much of the work in the literature identifies the bandgap energy by backing out the Coulomb interaction[72] from a measured feature in the optical constants or by extrapolating the below-bandgap Urbach edge to a known bandgap absorption coefficient.[36,71] On the other hand, in this work the bandgap is identified directly from onset of absorption in the measured optical constants, which may be better described as the optical bandgap.

When comparing the features in the GaAs optical constants measured in this work to those in the literature, the energy of the onset of absorption and the peak in the index of refraction are at the same energy positions. This indicates that any discrepancy is not due to experimental measurement differences, such as temperature or doping level, but instead is a result of how the bandgap is determined from the optical constants, such as how the onset of absorption is impacted by the Coulomb interaction. There is a distinction between the single-electron bandgap, a theoretical construct based on the assumption of empty conduction band that neglects many-body effects, and the optical bandgap energy that includes the effects of electron-electron interactions and electron-hole interactions, encompassing excitonic absorption and the Coulomb interaction. These effects result in a smaller optical bandgap than that predicted from the single-electron model.

The optical bandgap energy is the most relevant consideration in the description and design of optoelectronic devices, as it is the energy of the onset of absorption and emission that determines how devices perform. For example, the bandgap energy is generally described as the cutoff of absorption in photodetectors and photovoltaic solar cells and as the cutoff of emission from light emitting diodes.

Somewhat closer agreement is found between the GaSb, InAs, and InSb bandgap energies measured in this work and those reported in the literature. A literature survey finds 297 K bandgap energies ranging from 0.724 to 0.728 eV for GaSb,[74-77] from 0.350 to 0.356 eV for InAs,[78-80] and from 0.169 to 0.180 eV for InSb.[80-84] The optical bandgap energies measured in this work are 0.730 eV, 0.357 eV, and 0.180 eV for GaSb, InAs, and InSb respectively, which are all on the upper end of the range measured in the literature. Many of these measurements are based on analysis of photoluminescence peak energy or extrapolations of absorption coefficient down to zero. There are complications in the extraction of optical bandgap energy for each of these various methods which can make it difficult to exactly compare the room temperature bandgap energy.

5.0 CONCLUSIONS

InAsSbBi samples are grown by molecular beam epitaxy at temperatures ranging from 345 – 440 °C and using a variety of techniques including random alloy, digital alloy, and "metal-modulation" digital alloy growth. X-ray diffraction measurements and low-temperature photoluminescence measurements provide the unstrained InAsSbBi lattice constant and bandgap energy respectively. The lattice constant and bandgap energy are used to determine the average chemical composition of each InAsSbBi sample. The Bi mole fractions incorporated range from 0.04% to 1.81%, the Sb mole fractions range from 5.03% to 10.17%, and the As mole fractions range from 89.74% to 94.46%. The InAsSbBi samples luminesce at photon energies of 0.244 eV to 0.322 eV (5.08 μm to 3.85 μm). Nomarski optical microscopy images reveal widely varying surface morphology ranging from smooth, specular samples to rough, droplet-covered or pitted sample surfaces. The bulk random alloy samples generally exhibit better agreement between coupled $\omega - 2\theta$ x-ray diffraction measurements of the (400) plane and simulations, with sharper layer peaks, than do the digital alloy or "metal-modulation" digital alloy samples. This indicates superior crystalline quality of the bulk InAsSbBi layers and improved interfaces for the random alloy growths. Additionally, photoluminescence intensity is generally improved for random alloy growth versus digital alloy or "metal-modulation" digital alloy growth. No systematic differences in the average Bi mole fraction incorporated are observed between the different modes of InAsSbBi growth. The results suggest that growth temperature and As/In flux overpressures are the key growth factors driving Bi incorporation, and that alternative growth methods such as digital alloy growth or "metal-modulation" digital alloy growth tend to result in inferior material physical and optical quality compared to random alloy growth, without a significant change in Bi incorporation rate.

The integrated photoluminescence study of radiation-damaged InAsSbBi indicates that the Bi-containing alloy may be marginally more radiation tolerant than reference InAsSb by approximately 5-10%, however more measurements are needed to make a formal conclusion regarding the radiation-hardness of Bi-containing alloys.

The microstructural investigation of InAsSbBi layers grown on (100) on-axis, (100) 1° and 4° to (011) offcut GaSb substrates indicate high-quality, pseudomorphic, defect free layers with sharp interfaces. Excess Bi around 32% of the incident flux accumulates on the surface resulting in the optically rough 3 μm Bi rich droplet covered surfaces. Preferentially oriented surface features along $[0\bar{1}1]$ step edge direction are observed for the growth on (100) 1° to (011) offcut substrate. Substrate offcut did not significantly change the Bi incorporation. Lateral modulation in Bi mole fraction is observed on (100) on-axis and (100) 4° to (111)A offcut substrates, which has a step edge density of 2.3×10^6 per cm. Bi composition modulation is not observed in the growth on the (100) 1° to (011) offcut substrate, which has a step edge density of 5.7×10^6 per cm. The layers are compressively strained, and pseudomorphic along with strain induced crystallographic tilt observed on offcut (100) 1° and 4° to (011) substrates. A tilt model as a function of out-of-plane distortion and the offcut angle is established which agrees well with the measured tilt. The unit cell for coherently strained epilayers grown on offcut substrates in the (011) direction is monoclinic. The unit cell lattice constants and angles are derived.

The X-ray diffraction and temperature dependent photoluminescence measurements of InAsSb, GaInAsSb, InAsSbBi, and GaInAsSbBi indicate that Sb and Bi reduces the zero-temperature bandgap energy by -10 meV/%Sb and -52 mev/%Bi, and increases the zero-temperature photoluminescence width intercept by 0.3 mev/%Sb and 13.2 mev/%Bi. Under lean As flux, about 10-15% of the incident Bi flux incorporates at 400 °C and excess surface Bi can result in droplet formation. A quinary bandgap bowing model is developed to determine the GaInAsSbBi mole fractions lattice constant measured from X-ray diffraction and zero-temperature bandgap measured from photoluminescence.

Temperature-dependent time-resolved photoluminescence measurements indicate the minority carrier lifetime at 77 K of the mid-wave type-II InAs/InAsSb and InGaAs/InAsSb superlattices are 2.28 μs and 1.32 μs, respectively. The temperature-dependent steady-state photoluminescence measurements of the mid-wave/long-wave superlattice structures indicate that carriers excited in the mid-wave region diffuse into the long-wave region from 12 K at the lowest and 125 K at the highest. As the thickness of the mid-wave superlattice is reduced, the long-wave superlattice photoluminescence intensity increases indicating that more carriers are successfully diffusing into the long-wave region. Further, for the 1400 nm thick mid-wave superlattices, the long-wave superlattices do not luminesce until around 50 K, indicating that the diffusion length increases with temperature. Incorporation of Ga in the superlattice structure appears to increase the vertical hole mobility by a factor of 2.

A molecular beam epitaxy growth model based on the kinetics of Bi adsorption, desorption, incorporation, surface accumulation, and droplet formation is applied to the quaternary alloy InAsSbBi grown on GaSb. A solution for steady state growth is derived and the model parameters are fit to experimentally measured Bi mole fractions for bulk and quantum well InAsSbBi samples grown at 400 °C and 420 °C. The Bi mole fractions predicted by the model agree to within a single standard deviation of uncertainty on the measured mole fractions, and to within +19/-18% relative error on mole fraction for 400 °C growth and +57/-62% relative error on mole fraction for 420 °C growth. The results indicate that Bi incorporation rate reduces with growth temperature while Bi self-desorption increases with temperature. The characteristic temperatures for Bi desorption and incorporation rates are 20.17 K and 20.56 K respectively, tracking closely with the 20 °C difference in growth temperatures examined. As-assisted removal and exchange of Bi dominates the growth process. Sb-assisted removal and exchange of Bi plays a negligible role in the growth of InAsSbBi. The net result is a reduction of Bi mole fraction for growth at higher temperature. The model indicates that the Bi surface coverage is directly proportional to the Bi/In flux and decreases as As/In flux increases. As-assisted exchange of Bi from the crystal termination layer and removal of Bi from the surface layer results in reduced Bi mole fraction and decreased likelihood of Bi-rich droplet formation. The model predicts that under droplet-free growth conditions, the ultimate achievable Bi mole fractions are 2.64% and 0.99% for growth at 400 °C and 420 °C respectively. The characteristic temperature of this ultimate Bi mole fraction limit is 20.70 K, indicating that the growth temperature must be reduced to 380 °C to obtain the lattice-matched endpoint ternary alloy $InAs_{0.932}Bi_{0.068}$ on GaSb.

The intrinsic absorption edges of GaAs, GaSb, InAs, and InSb are examined using a model that is developed to describe and parameterize the experimentally observed features of the fundamental bandgap absorption edge, which include the optical bandgap energy E_g, the width of the Urbach tail E_u, the impact of the Coulomb interaction on the absorption edge p_g, and the magnitude of the absorption coefficient at the bandgap cutoff α_g and at the knee of the absorption spectrum α_k. The Urbach parameter E_u is determined from the exponential absorption edge below the bandgap and the optical bandgap parameter E_g and absorption edge power law parameter p_g are determined from the above-bandgap absorption. The room-temperature (297 K) values of the optical bandgap energy and Urbach parameter are 1.418 eV and 8.7 meV for GaAs, 0.730 eV and 14.0 meV for GaSb, 0.357 eV and 14.1 meV for InAs, and 0.180 eV and 10.7 meV for InSb. The GaAs optical bandgap energy determined from the absorption coefficient, extinction coefficient, and real part of the dielectric function agree closely with the peak values of the refractive index and real dielectric function. The energy dependence of the optical absorption above the bandgap is observed to be most accurately described by the constant dipole matrix element approximation for GaAs where the Coulomb interaction is strong and by the constant transition strength approximation for InSb where the Coulomb interaction is weak.

6.0 PUBLICATIONS ACKNOWLEDGING AFRL GRANT SUPPORT

Articles in Refereed Journals

Rajeev R. Kosireddy, Stephen T. Schaefer, Marko S. Milosavljevic, Shane R. Johnson, *Structural and Optical Properties of InAsSbBi Grown by Molecular Beam Epitaxy on Offcut GaSb Substrates*, Photonics **8**, 215 (2021); 20 pages

Stephen T. Schaefer, Marko S. Milosavljevic, Rajeev R. Kosireddy, Shane R. Johnson, *Kinetic model for molecular beam epitaxy growth of InAsSbBi alloys*, J. Appl. Phys. **129**, 035303, 1-19 (2021); published January 2021; 19 pages.

Rajeev R. Kosireddy, Stephen T. Schaefer, P. T. Webster, Marko S. Milosavljevic and Shane R. Johnson, *Temperature dependence of atomic ordering and composition modulation in InAsSbBi grown by molecular beam epitaxy on GaSb substrates*, J. Alloys Compd., **859**, 157860 (2021), 1-8; published November 2020; 8 pages.

S. T. Schaefer, S. Gao, P. T. Webster, R. R. Kosireddy, and S. R. Johnson, *Absorption edge characteristics of GaAs, GaSb, InAs, and InSb*, J. Appl. Phys. **127**, 165705 (2020); 15 pages

Conference Presentations and Abstracts

Stephen T. Schaefer, Marko S. Milosavljevic, Rajeev R. Kosireddy, Shane R. Johnson, *Kinetic Model for Molecular Beam Epitaxy Growth of InAsSbBi Alloys*, 21st International Conference on Molecular Beam Epitaxy, Puerto Vallarta, Mexico, September 2021.

M. S. Milosavljevic, S. T. Schaefer, R. R. Kosireddy, P. T. Webster, S. R. Johnson, *Crystallographic tilt in coherently strained InAsSbBi grown on (100) GaSb substrates offcut toward [011]*, 21st International Conference on Molecular Beam Epitaxy, Puerto Vallarta, Mexico, September 2021.

Stephen T. Schaefer, Marko S. Milosavljevic, Preston T. Webster, Shane R. Johnson, *Temperature and excitation dependent photoluminescence measurements of nonradiative lifetime in InAs(SbBi)*, 15th International Conference on Mid-IR Optoelectronics: Materials and Devices, Surrey, United Kingdom, September 2021.

M. S. Milosavljevic, S. T. Schaefer, R. R. Kosireddy, P. T. Webster, S. R. Johnson, *Optical properties of InAsSbBi and GaInAsSbBi grown on GaSb substrates*, 15th International Conference on Mid-IR Optoelectronics: Materials and Devices, Surrey, United Kingdom, September 2021.

Stephen T. Schaefer, Rajeev R. Kosireddy, Marko S. Milosavljevic, Preston T. Webster, and Shane R. Johnson, *Impact of growth conditions, surface reconstructions, and substrate offcut on the structural and optical properties of InAsSbBi grown on GaSb by molecular beam epitaxy*, 2020 Lawrence Symposium on Epitaxy, Scottsdale AZ, February 2020.

Rajeev. R. Kosireddy, Stephen T. Schaefer, and S. R. Johnson, *Microstructure, chemical composition, and surface morphology of InAsSbBi grown on GaSb by molecular beam epitaxy*, 35th North American Conference on Molecular Beam Epitaxy, Ketchum ID, September 2019.

Stephen T. Schaefer, Rajeev R. Kosireddy, and S. R. Johnson, *Molecular beam epitaxy growth and bandgap measurements of InAsSbBi*, 35th North American Conference on Molecular Beam Epitaxy, Ketchum ID, September 2019.

Patents

Stephen T. Schaefer, Marko S. Milosavljevic, Rajeev R. Kosireddy, Shane R. Johnson, *Kinetic model for molecular beam epitaxy growth of III-V alloys*, US provisional patent 63/126,229, filed December 16th, 2020, 103 pages.

Stephen T. Schaefer, Shang Gao, Shane R. Johnson, *Devices, systems, and methods utilizing an improved optical absorption model for direct-gap semiconductors*, US patent serial number 16/999,975, filed August 21st, 2020, 49 pages.

Stephen T. Schaefer, Shang Gao, Shane R. Johnson, *Devices, systems, and methods utilizing an improved optical absorption model for direct-gap semiconductors*, US provisional patent 62/890,324, filed August 22nd, 2019, 20 pages.

7.0 REFERENCES

[1] S. T. Schaefer, R. R. Kosireddy, P. T. Webster, and S. R. Johnson, “Molecular beam epitaxy and optical properties of InAsSbBi”, J. Appl. Phys. **126**, 083101 (2019).

[2] P. T. Webster, A. J. Shalindar, S. T. Schaefer, and S. R. Johnson, “Bandgap and composition of bulk InAsSbBi grown by molecular beam epitaxy”, Appl. Phys. Lett. **111**, 082104 (2017).

[3] X’pert Epitaxy software, PANalytical B. V., Almelo, The Netherlands.

[4] C. H. Macgillavry and G. D. Rieck, “International Tables for Crystallography” (The Kynoch Press, Birmingham, England, 1968).

[5] I. Vurgaftman, J. R. Meyer, and L. R. Ram-Mohan, Band parameters for III-V compound semiconductors and their alloys, J. Appl. Phys. **89** (2001) 5815.

[6] A. J. Shalindar, P. T. Webster, B. J. Wilkens, T. L. Alford, and S. R. Johnson, “Measurement of InAsBi mole fraction and InBi lattice constant using Rutherford backscattering spectrometry and X-ray diffraction”, J. Appl. Phys. **120**, 145704 (2016).

[7] WVASE32, version 3.774, Lincoln, NE, USA.

[8] J. W. Matthews and A. E. Blakeslee, “Defects in epitaxial multilayers: I. Misfit dislocations”, J. Crystal Growth **27**, 18-125 (1974).

[9] MATLAB, version 2020a, Natick, MA, USA.

[10] P. T. Webster, N. A. Riordan, C. Gogineni, S. Liu, J. Lu, X.-H. Zhao, D. J. Smith, Y.-H. Zhang, and S. R. Johnson, "Molecular beam epitaxy using bismuth as a constituent in InAs and a surfactant in InAs/InAsSb superlattices", J. Vac. Sci. Technol. B **32**(2), 02C120-1 (2014).

[11] R. R. Kosireddy, S. T. Schaefer, A. J. Shalindar, and S. R. Johnson, "Microstructure and surface morphology of InAsSbBi grown by molecular beam epitaxy", J. Appl. Phys. **126**, 095108 (2019).

[12] J. A. Olsen, E. L. Hu, S. R. Lee, I. J. Fritz, A. J. Howard, B. E. Hammons, and J. Y. Tsao,” X-ray reciprocal-space mapping of strain relaxation and tilting in linearly graded InAlAs buffers,” J. Appl. Phys. **79**, 3578 (1996).

[13] V. M. Kaganer, R. Kohler, M. Shmidbauer, R. Opitz, B. Jenichen, “X-ray diffraction peaks due to misfit dislocations in heteroepitaxial structures,” Phys. Rev. B **55**, 1793 (1997).

[14] J. M. Chauveau, Y. Androussi, A. Lefebvre, J. Di Persio, Y. Cordier, “Indium content measurements in metamorphic high electron mobility transistor structures by combination of X-ray reciprocal space mapping and transmission electron microscopy,” J. Appl. Phys. **93**, 4219 (2003) .

[15] X. Lu, D. A. Beaton, R. B. Lewis, T. Tiedje, and M. B. Whitwick, “Effect of molecular beam epitaxy growth conditions on the Bi content of GaAs(1-x)Bi(x),” Appl. Phys. Lett. **92**(19), 192110 (2008).

[16] R. B. Lewis, M. Masnadi-Shirazi, and T. Tiedje, “Growth of high Bi concentration GaAs(1-x)Bi(x) by molecular beam epitaxy,” Appl. Phys. Lett. **101**(8), 082112 (2012).

[17] C. R. Tait and J. M. Millunchick, "Kinetics of droplet formation and Bi incorporation in GaSbBi alloys", J. Appl. Phys. **119**, 215302 (2016).

[18] M. K. Rajpalke, W. M. Linhart, K. M. Yu, T. S. Jones, M. J. Ashwin, and T. D. Veal, "Bi flux-dependent MBE growth of GaSbBi alloys", J. Cryst. Growth **425**, 241–244 (2015).

[19] P. T. Webster, N. A. Riordan, S. Liu, E. H. Steenbergen, R. A. Synowicki, Y.-H. Zhang, and S. R. Johnson, "Measurement of InAsSb bandgap energy and InAs/InAsSb band edge positions using spectroscopic ellipsometry and photoluminescence spectroscopy", J. Appl. Phys. **118**, 245706 (2015).

[20] P. T. Webster, N. A. Riordan, S. Liu, E. H. Steenbergen, R. A. Synowicki, Y.-H. Zhang, and S. R. Johnson, "Absorption properties of type-II InAs/InAsSb superlattices measured by spectroscopic ellipsometry", Appl. Phys. Lett. **106**, 061907 (2015).

[21] D. Souri and Z. E. Tahan, "A new method for the determination of optical band gap and the nature of optical transitions in semiconductors", Appl. Phys. B **119**, 273–279 (2015).

[22] P. T. Webster, A. J. Shalindar, N. A. Riordan, C. Gogineni, H. Liang, A. R. Sharma, and S. R. Johnson, "Optical properties of InAsBi and optimal designs of lattice-matched and strain-balanced III-V semiconductor superlattices", J. Appl. Phys. **119**, 225701 (2016).

[23] S. R. Johnson and T. Tiedje, "Temperature dependence of the Urbach edge in GaAs," J. Appl. Phys. **78**, 5609 (1995).

[24] L. Viña, S. Logothetidis, and M. Cardona, "Temperature dependence of the dielectric function of germanium," Phys. Rev. B **30**, 1979 (1984).

[25] L. Vegard, "Die Konstitution der Mischkristalle und die Raumfüllung der Atome," Z. Phys. **5**, 17–26 (1921).

[26] Gwyddion, version 2.56, GNU General Public License.

[27] Y. Horikoshi, M. Kawashima, and H. Yamaguchi, "Migration-enhanced epitaxy of GaAs and AlGaAs", Jap. J. Appl. Phys. **27**, 169-179 (1988).

[28] A. Y. Cho, "Growth of III-V semiconductors by molecular beam epitaxy and their properties", Thin Film Solids **100**, 291-317 (1983).

[29] C. B. Alcock, V. P. Itkin, and M. K. Horrigan, "Vapour pressure equations for the metallic elements: 298-2500K", Canadian Metallurgical Quarterly **23**, 309 (1984).

[30] H. P. Gavin, "The Levenberg-Marquardt algorithm for nonlinear least squares curve-fitting problems", Department of Civil and Environmental Engineering, Duke University (2019).

[31] H. Kobayashi, B. L. Mark, and W. Turin, Ch. 6, 151-152 in "Probability, Random Processes, and Statistical Analysis : Applications to Communications, Signal Processing, Queueing Theory and Mathematical Finance", Cambridge University Press, Cambridge, UK, 1st Edition (2012).

[32] E. C. Young, S. Tixier, and T. Tiedje, "Bismuth surfactant growth of the dilute nitride GaN(x)As(1-x)", J. Cryst. Growth 279, 316 (2005).

[33] S. Tixier, M. Adamcyk, T. Tiedje, S. Francoeur, A. Mascarenhas, P. Wei, and F. Schiettekatte, "Molecular beam epitaxy growth of GaAs(1-x)Bi(x)", Appl. Phys. Lett. 82, 2245 (2003).

[34] M. K. Rajpalke, W. M. Linhart, M. Birkett, K. M. Yu, J. Alaria, J. Kopaczek, R. Kudrawiec, T. S. Jones, M. J. Ashwin, and T. D. Veal, "High Bi content GaSbBi alloys", J. Appl. Phys. 116, 043511 (2014).

[35] M. V. Kurik, "Urbach Rule", Phys. Status Solidi A 8, 9 (1971).

[36] M. Beaudoin, A. J. G. DeVries, S. R. Johnson, H. Laman, and T. Tiedje, “Optical absorption edge of semi-insulating GaAs and InP at high temperatures”, Appl. Phys. Lett. 70, 26 (1997).

[37] V K Malyutenko and V I Chernyakhovsky, “Thermal emission of InAs induced by band tails”, Semicond. Sci. Technol. 9, 1047-1049 (1994).

[38] R. J. Elliott, “Intensity of Optical Absorption by Excitons”, Phys. Rev. 108, 1384 (1957).

[39] S. L. Chuang, Physics of Optoelectronic Devices (Wiley, New York, 1995), p. 355.

[40] J. S. Blakemore, “Semiconducting and other major properties of gallium arsenide”, J. Appl. Phys. 53, R123 (1982).

[41] Y. H. Lee, A. Chavez-Pirson, S. W. Koch, H. M. Gibbs, S. H. Park, J. Morhange, A. Jeffery, and N. Peyghambarian, “Room-temperature optical nonlinearities in GaAs”, Phys. Rev. Lett. 57, 2446 (1986).

[42] P. P. Paskov, “Optical absorption and refraction spectra in highly excited GaSb”, IEEE J. Quantum Elec. 30, 12 (1994).

[43] P. K. Basu, Theory of Optical Processes in Semiconductors (Clarendon Press, Oxford, 1997), p. 87.

[44] A. R. Hassan, “On the estimation of matrix elements for optical transitions in semiconductors”, Optics Communications 98, 80-85 (1993).

[45] W. B. Jackson, S. M. Kelso, C. C. Tsai, J. W. Allen, and S.-J. Oh, “Energy dependence of the optical matrix element in hydrogenated amorphous and crystalline silicon”, Phys. Rev. B 31, 5187 (1985).

[46] M. Rohlfing and S. G. Louie, “Electron-Hole Excitations in Semiconductors and Insulators”, Phys. Rev. Lett. 81, 2312 (1998).

[47] T. Ogawa and T. Takagahara, “Optical absorption and Sommerfeld factors of one-dimensional semiconductors: An exact treatment of excitonic effects”, Phys. Rev. B 44, 8138 (1991).

[48] P. J. P. Tang, M. J. Pullin, and C. C. Phillips, “Binding energy of the free exciton in indium arsenide”, Phys. Rev. B 55, 7 (1996).

[49] I. Pelant and J. Valenta, Luminescence Spectroscopy of Semiconductors (Oxford University Press, Oxford UK, 2016), p. 163.

[50] A. Gray, E. Abbena, and S. Salamon, Modern differential geometry of curves and surfaces with Mathematica (Chapman & Hall CRC, Boca Raton, FL, 2006), p. 14.

[51] P. Y. Yu and M. Cardona, Fundamentals of Semiconductors (Springer-Verlag, Berlin Heidelberg, 2010), p. 276.

[52] W. H. Press, S. A. Teukolsky, W. T. Vetterling, and B. P. Flannery, Numerical Recipes in Fortran 77: The Art of Scientific Computing (Press Syndicate, University of Cambridge, 1986), p. 180.

[53] Wafer Technology Company, 34 Maryland Road, Milton Keynes, MK15 8HJ, UK.

[54] F. Stern, “Dispersion of the Index of Refraction Near the Absorption Edge of Semiconductors”, Phys. Rev. B 133, A1653 (1964).

[55] G. E. Stillman, C. M. Wolfe, and J. O. Dimmock, in Semiconductors and Semimetals (Academic, New York), Vol. 12, p. 169 (1977).

[56] M. Hass and B. W. Henvis, "Infrared lattice reflection spectra of III-V compound semiconductors", J. Phys. Chem. Solids 23, 1099 (1962).

[57] J. R. Dixon and J. K. Furdyna, "Measurement of the static dielectric constant of the InSb lattice via gyrotropic sphere resonances", Solid State Communications 35, 195 (1980).

[58] M. W. Heller, and R. G. Hamerly, “Hole transport in gallium antimonide”, J. Appl. Phys. 57, 10, 4626-4632 (1985).

[59] F. P. Kesamanly, Yu. MaTtsev, D. N. Nasledov, L. A. Nikolaeva, M. N. Pivovarov, V. A. Skripkin, and Yu. I. Uvanov, Fiz. Tekhn. Polupr. 3, 8, p. 1182-1187 (1969).

[60] W. Zawadski, “Electron transport phenomena in small-gap semiconductors”, Advances in Phys. 23, p. 435-522 (1974).

[61] J.-M. Jancu, R. Scholz, E. A. de Andrada e Silva, and G. C. La Rocca, “Atomistic spin-orbit coupling and k·p parameters in III-V semiconductors”, Phys. Rev. B 72, p. 193201 (2005).

[62] M. Merian and A. K. Bhattacharjee, “Momentum Matrix Elements in III-V Semiconductor Alloys”, Solid State Communications 55, 12, p. 1071-1073 (1985).

[63] C. Hermann and C. Weisbuch, “$k \vec{\cdot} p$ perturbation theory in III-V compounds and alloys: a reexamination”, Phys. Rev. B 15, 2, p. 823-833 (1977).

[64] P. Pfeffer and W. Zawadzki, “Five-level k–p model for the conduction and valence bands of GaAs and InP”, Phys. Rev. B 53, 19, p. 12813-12828 (1996).

[65] E. O. Kane, “Band Structure of Indium Antimonide”, J. Phys. Chem. Solids 1, 249 (1957).

[66] V. Lucarini, J. J. Saarinen, K. -E. Peiponen, E.M. Vartiainen, Kramers-Kronig Relations in Optical Materials Research (Springer, Berlin, 2005), p. 35.

[67] M. D. Sturge, "Optical Absorption of Gallium Arsenide between 0.6 and 2.75 eV", Phys. Rev. 127, 768 (1962).

[68] P. Lautenschlager, M. Garriga, S. Logothetidis, and M. Cardona, "Interband critical points of GaAs and their temperature dependence", Phys. Rev. B 35, 9174 (1987).

[69] H. C. Casey, D. D. Sell, and K. W. Wecht, “Concentration dependence of the absorption coefficient for n− and p−type GaAs between 1.3 and 1.6 eV”, J. Appl. Phys. 46, 250 (1975).

[70] G. M. Martin, “Optical assessment of the main electron trap in bulk semi-insulating GaAs”, Appl. Phys. Lett. 39, 747 (1981).

[71] M. B. Panish and H. C. Casey, Jr, "Temperature Dependence of the Energy Gap in GaAs and GaP", J. Appl. Phys. 40, 163 (1969).

[72] D. D. Sell, H. C. Casey Jr., and K. W. Wecht, "Concentration dependence of the refractive index for n - and p -type GaAs between 1.2 and 1.8 eV", J. Appl. Phys. 45, 2650 (1974).

[73] D. S. Chemla, D. A. B. Miller, and P. W. Smith, “Nonlinear Optical Properties of Multiple Quantum Well Structures for Optical Signal Processing”, Semiconductors and Semimetals Vol 24, 279 (1987).

[74] M.-C. Wu and C.-C. Chen, “Photoluminescence of high-quality GaSb grown from Ga- and Sb rich solutions by liquid-phase epitaxy”, J. Appl. Phys. 72, 4275 (1992).

[75] V. Bellani, S. Di Lemia, M. Geddo, G. Guizzetti, A. Bosacchi, S. Franchi and R. Magnanini, “Thermoreflectance Study of the direct energy gap of GaSb”, Solid State Comm. 104, 81 (1997).

[76] C. Ghezzi, R. Magnanini, A. Parisini, B. Rotelli, L. Tarricone, A. Bosacchi, and S. Franchi, “Optical absorption near the fundamental absorption edge in Gasb”, Phys. Rev. B 52, 1463 (1995).

[77] A. Joullié, A. Zein Eddin, and B. Girault, “Temperature dependence of the L_6^c-Γ_6^c energy gap in gallium antimonide”, Phys. Rev. B 23, 928 (1981).

[78] E. Adachi, “Energy band parameters of InAs at various temperatures”, J. Phys. Soc. Jpn. 24, 1178 (1968).

[79] J. R. Dixon and J. M. Ellis, “Optical properties of n-Type Indium Arsenide in the fundamental absorption edge region”, Phys. Rev. 123, 1560 (1961).

[80] Z. M. Fang, K. Y. Ma, D. H. Jaw, R. M. Cohen, and G. B. Stringfellow, “Photoluminescence of InSb, InAs, and InAsSb grown by organometallic vapor phase epitaxy”, J. Appl. Phys. 67, 7034 (1990).

[81] Y. J. Jung, M. K. Park, S. I. Tae, K. H. Lee, and H. J. Lee, “Electron transport and energy-band structure of InSb”, J. Appl. Phys. 69, 3109 (1991).

[82] C. L. Littler and D. G. Seiler, “Temperature dependence of the energy gap of InSb using nonlinear optical techniques”, Appl. Phys. Lett. 46, 986 (1985).

[83] D. Auvergne, J. Camassel, H. Mathieu, and M. Cardona, “Temperature dependence of the band structure of germanium and zinc-blende-type semiconductors”, Phys. Rev. B 9, 5168 (1974).

[84] J. Camassel and D. Auvergne, “Temperature dependence of the fundamental edge of germanium and zinc-blende-type semiconductors”, Phys. Rev. B 12, 3258 (1975).

[85] E. G. Bithell and W. M. Stobbs, "Composition determination in the GaAs/(Al, Ga)As system using contrast in dark-field transmission electron microscope images," Philos. Mag. A 60, 39 (1989).

[86] P. A. Doyle and P. S. Turner, "Relativistic Hartree–Fock X-ray and electron scattering factors," Acta Crystallogr. Sect. A 24, 390 (1968).

[87] S. J. Pennycook et al., “Aberration-corrected scanning transmission electron microscopy: from atomic imaging and analysis to solving energy problems,” Philos. Trans. R. Soc. A Math. Phys. Eng. Sci. 367, 1903 (2009).

LIST OF SYMBOLS, ABBREVIATIONS, AND ACRONYMS

AFM – Atomic force microscopy

AFRL – Air Force Research Laboratory

As – Arsenic

Bi – Bismuth

Ga – Gallium

He – Helium

In – Indium

IR – Infrared

LW – Long-wave

MW – Mid-wave

PL – Photoluminescence

RBS – Rutherford backscattering

Sb – Antimony

SL – Superlattice

TEM – Transmission electron microscopy

XRD – X-ray diffraction

DISTRIBUTION LIST

DTIC/OCP 8725 John J. Kingman Rd, Suite 0944 Ft Belvoir, VA 22060-6218	1 cy
AFRL/RVIL Kirtland AFB, NM 87117-5776	1 cy
Official Record Copy AFRL/ RVS/Preston Webster	1 cy

(This Page Intentionally Left Blank)